Forschungszentrum Karlsruhe
in der Helmholtz-Gemeinschaft
Wissenschaftliche Berichte
FZKA 7244

The COMET-L3 Experiment on Long-Term Melt – Concrete Interaction and Cooling by Surface Flooding

H. Alsmeyer, T. Cron, B. Fluhrer,
G. Messemer, A. Miassoedov,
S. Schmidt-Stiefel, T. Wenz

Institut für Kern- und Energietechnik
Programm Nukleare Sicherheitsforschung

Februar 2007

Forschungszentrum Karlsruhe
in der Helmholtz-Gemeinschaft
Wissenschaftliche Berichte

FZKA 7244

The COMET-L3 Experiment on Long-Term Melt – Concrete Interaction and Cooling by Surface Flooding

H. Alsmeyer, T. Cron, B. Fluhrer, G. Messemer,
A. Miassoedov, S. Schmidt-Stiefel, T. Wenz

Institut für Kern- und Energietechnik
Programm Nukleare Sicherheitsforschung

Forschungszentrum Karlsruhe GmbH, Karlsruhe
2007

Forschungszentrum Karlsruhe GmbH
Postfach 3640, 76021 Karlsruhe

Mitglied der Hermann von Helmholtz-Gemeinschaft
Deutscher Forschungszentren (HGF)

ISSN 0947-8620

urn:nbn:de:0005-072449

Abstract

The COMET-L3 experiment considers the long-term situation of corium/concrete interaction in an anticipated core melt accident of a light-water-reactor, after the metal melt is layered beneath the oxide melt. The experimental focus is on cavity formation in the basemat and the risk of long term basemat penetration. The experiment investigates the two-dimensional concrete erosion in a cylindrical crucible fabricated from siliceous concrete in the first phase of the test, and the influence of surface flooding in the second phase. Decay heating in the two-component metal and oxide melt is simulated by sustained induction heating of the metal phase that is overlaid by the oxide melt.

The inner diameter of the concrete crucible was 60 cm, the initial mass of the melt was 425 kg steel and 211 kg oxide at 1665°C, resulting in a melt height of 450 mm. The net power to the metal melt was about 220 kW from 0 s to 1880 s, when the maximum erosion limit of the crucible was reached and heating was terminated.

In the initial phase of the test (less than 100 s), the overheated, highly agitated metal melt causes intense interaction with the concrete, which leads to fast decrease of the initial melt overheat and reduction of the initially high concrete erosion rate. Thereafter, under quasi-stationary conditions until about 800 s, the erosion by the metal melt slows down to some 0.07 mm/s into the axial direction. Lateral erosion is a factor 3 smaller. Video observation of the melt surface shows an agitated melt with ongoing gas release from the decomposing concrete. Several periods of more intense gas release, gas driven splashing, and release of crusts from the concrete interface indicate the existence and iterative break-up of crusts that probably form at the steel/concrete interface.

Surface flooding of the melt is initiated at 800 s by a shower from the crucible head with 0.375 litre water/s. Flooding does not lead to strong melt/water interactions, and no entrapment reactions or penetration of water into the melt did occur. A nearly closed surface crust forms within 60 s after start of flooding and quenches after not more than 140 s. Residual holes in the crust are closed and the crust separates the coolant water overlayer and the hot melt below. Concrete erosion continues - although reduced - with some 0.040 mm/s, and eventually the melt reaches the maximum erosion limit of the crucible, at what time the simulated decay power is cut off. Two volcanic melt eruptions, that developed at the crust surface for a duration of 2 min each, had minor influence on coolabilty, as only 2.8 kg oxide particles were ejected into the overlaying water pool. Finally, the volcanic vents were blocked, and there are no indications that water ingression occurred through the surface crust.

Post test analysis of the solidified melt was performed after the crucible was sectioned. The solidified melt shows no indication of water ingression from the upper surface. Tight crusts explain poor heat removal to the flooding water and the ongoing concrete erosion also after top flooding.

The experiment shows many phenomena that are important to understand and to model the late phase of a core melt accident, and shall be used for model and code validation. Detailed experimental data are given, especially for concrete erosion by the metal melt, for time dependent cavity formation, and for the influence of surface flooding.

Zusammenfassung

Das COMET-L3 Experiment zur langzeitigen Schmelze-Beton-Wechselwirkung und zur Flutung der Schmelzenoberfläche

Das COMET-L3 Experiment untersucht die Langzeitsituation der Schmelze-Beton-Wechselwirkung bei einem unterstellten Kernschmelzunfall in einem Leichtwasser-Reaktor, nachdem die Metallschmelze unter der Oxidschmelze geschichtet ist. Das Experiment zielt auf die Ausbildung der Kaverne im Fundament des Reaktors sowie auf das Risiko der langzeitigen Fundamentdurchdringung. In einem zylindrischen Tiegel, gefertigt aus silikatischem Beton, wird in der ersten Phase des Experiments die zwei-dimensionale Betonerosion untersucht, und in der anschließenden zweiten Phase der Einfluss von Wasseraufgabe auf die Schmelze. Die Simulation der Nachwärme in der 2-komponentigen Metall- und Oxidschmelze erfolgt durch fortwährende induktive Beheizung der Metallschmelze, die von der Oxidschmelze überdeckt ist.

Der Innendurchmesser des Betontiegels betrug 60 cm; die Anfangsmasse der Schmelze war 425 kg Stahl plus 211 kg Oxid von anfangs 1665°C, mit einer Höhe der Gesamtschmelze von 450 mm. Die Nettoleistung, die in die Metallschmelze eingebracht wurde, betrug etwa 220 kW von 0 bis 1880 s. Zu diesem Zeitpunkt wurde die maximale Erosion des Tiegels erreicht und die Beheizung beendet.

In der ersten Phase des Versuchs bis etwa 100 s gab es eine heftige Wechselwirkung der überhitzten, stark bewegten Metallschmelze mit dem Beton. Diese führt zu einer schnellen Abnahme der anfänglichen Übertemperatur der Schmelze und einer Reduktion der zunächst hohen Erosionsrate des Betons. Danach herrschen quasi-stationäre Bedingungen bis etwa 800 s, wobei sich die Erosion durch die Metallschmelze in axialer Richtung auf etwa 0,07 mm/s verlangsamt. Die Erosion in seitlicher Richtung ist etwa um den Faktor 3 geringer. Die Videobeobachtung der Schmelzenoberfläche zeigt eine bewegte Schmelze mit andauernder Gasfreisetzung aus der Betonzersetzung. Mehrere Phasen mit stärkerer Gasfreisetzung, gas-getriebenem Auswurf von Schmelze und aus der Schmelze aufschwimmende Krusten verweisen auf die Existenz und das wiederholte Aufbrechen von Krusten, die sich wahrscheinlich an der Kontaktfläche Stahlschmelze/Beton bilden.

Die Flutung der Schmelzenoberfläche wird nach 800 s durch Aktivierung einer Brause mit 0,375 Liter Wasser je s eingeleitet. Die Flutung erzeugt keine heftigen Reaktionen zwischen Wasser und Schmelze. Es treten auch keine Entrapmentreaktionen oder Eindringen von Wasser in die Schmelze auf. Innerhalb von 60 s nach Start der Flutung bildet sich eine nahezu geschlossen Oberflächenkruste, die nach nur 140 s gequenched ist. Verbliebene Öffnungen in der Kruste schließen sich, und damit trennt die Kruste die oben liegende

Wasserschicht und die untere heiße Schmelze. Die Erosion des Betons schreitet weiter fort – allerdings verlangsamt – mit etwa 0,040 mm/s, und schließlich erreicht die Schmelze die maximale Erosionsgrenze des Betontiegels, was zum Abschalten der Nachwärmeleistung führt. Zwei vulkanische Eruptionen von Schmelze, die sich an der Oberflächenkruste für jeweils 2 Minuten entwickelten, hatten geringen Einfluss auf die Kühlbarkeit, da lediglich 2,8 kg Oxidpartikel in die Wasserschicht ausgetragen wurden. Schließlich wurden die Vulkanöffnungen blockiert, und es gibt keine Hinweise, dass ein Eindringen von Wasser durch die Oberflächenkruste erfolgte.

Nachuntersuchungen an der erstarrten Schmelze wurden nach Durchtrennen des Tiegels durchgeführt. Die erstarrte Schmelze gibt keine Hinweise auf das Eindringen von Wasser von oben. Dichte Krusten sind der Grund dafür, dass die Wärmeabfuhr an das Wasser gering war und dass die Betonerosion nach der Flutung weiterging.

Das Experiment zeigt viele Phänomene auf, die wichtig sind, um die späte Phase eines Kernschmelzunfalls verstehen und modellieren zu können. Es soll für die Überprüfung von Modellen und Rechenprogrammen eingesetzt werden. Dazu werden detaillierte experimentelle Daten angegeben, insbesondere zur Betonerosion durch die Metallschmelze, für die zeitabhängige Ausbildung der Kaverne und für den Einfluss der Oberflächenflutung.

TABLE OF CONTENTS

1 Introduction..1

2 COMET - L3 Test Design..4

2.1 Facility description..4

2.2 Melt composition and melt generation..9

2.3 Decay heat simulation..11

2.4 Water supply and off-gas systems..12

2.5 Instrumentation and data acquisition..13

3 Experiment Preparation and Test Procedure..19

3.1 Preparation of the concrete crucible..19

3.2 Planned performance..22

3.3 Course of the test..23

4 Experimental Results..33

4.1 Mass and temperature of the melt..33

4.2 Decay heat simulation and melt behaviour..38

4.3 Concrete erosion and cavity shape..40

4.4 Gas release..47

4.5 Flooding and long-term melt behaviour..52

4.6 Post test analyses..56

4.7 Concrete erosion using post test data..65

5 Conclusions..71

6 References..75

Appendices..77

Appendix A: Summary of the realized test conditions..77

Appendix B: Data acquisition and channel assignments..79

Appendix C: Test data..86

LIST OF TABLES

Table 1: Specifications for COMET-L3 3
Table 2: Properties of the siliceous concrete for the crucible 8
Table 3: Planned characteristics of the initial oxide and metal melt in the concrete cavity 9
Table 4: Melt generation by thermite reaction in COMET-L3 10
Table 5: Planned power densities in COMET-L3 11
Table 6: Position of NiCr-Ni Thermocouples in Plane SW-NE in COMET-L3 18
Table 7: Position of NiCr-Ni Thermocouples in Plane SE-NW in COMET-L3 18
Table 8: Planned conduct of COMET-L3 23
Table 9: Sequence of COMET-L3 as observed during the test and from video-film 24
Table 10: Position and failure times of thermocouples in the concrete cavity 41
Table 11: Eroded concrete volume and related energy 62

Table B-1: COMET-L3 Channel assignment for Microlink-data acquisition system 80

LIST OF FIGURES

Figure 1: COMET test rig with its main components 5

Figure 2: Photo of the COMET facility 6

Figure 3: Dimensions of COMET-L3 crucible 7

Figure 4: Orientation of the instrumentation in planes NW-SE and SW-NE (top view) 15

Figure 5: Thermocouple and light guides instrumentation in plane SW-NE 16

Figure 6: Thermocouple and light guides instrumentation in plane SE-NW 17

Figure 7: Instrumentation during crucible fabrication: Light guides (black sheeting) and thermocouples fixed to glass rods 19

Figure 8: Fabricating the bottom of the concrete crucible 20

Figure 9: Fabricating the concrete crucible 20

Figure 10: The mould for the cavity filled with concrete 21

Figure 11: The lower side of the concrete crucible with the 30 mm deep cavity 21

Figure 12: Pour of the oxide melt fraction at 11 s 29

Figure 13: Intense melt concrete interaction with melt splashing at 115 s 29

Figure 14: Steady erosion with dark oxide material expelled from below (240 s) 30

Figure 15: Eruption of melt upon removal of interfacial crust (290 s) 30

Figure 16: Flooding the melt surface by a showerhead (840 s). The melt forms a darker, viscous surface layer 31

Figure 17: Continuous boiling of the flooded melt surface (1680 s) 31

Figure 18: Volcanic melt eruption through the flooded surface at 1760 s. Hot oxide particles are injected into the boiling water layer. 32

Figure 19: Weight of thermite vessel during thermite reaction and melt release 33

Figure 20: Melt temperature in the spout 34

Figure 21: Temperature of the metallic melt jet (left) and of the oxidic melt jet (right). 36

Figure 22: IR measured temperatures of the melt surface assuming the oxide emissivity of 0.92 37

Figure 23: Voltage to operate the induction coil 39

Figure 24: Net heating power in the melt by induction 39

Figure 25: Efficiency of the induction heating, referred to the gross heating power 39

Figure 26: Failure times of thermocouples in the concrete crucible through erosion of the heated melt. a) Plane SW-NE b) Plane SE-NW 42

Figure 27: Axial erosion front of propagating melt in plane SW-NE of the concrete cavity 44

Figure 28: Lateral erosion front of propagating melt in plane SW-NE of the concrete cavity 44

Figure 29: Axial erosion front of propagating melt in plane SE-NW of the concrete cavity 45

Figure 30: Lateral erosion front of propagating melt in plane SE-NW of the concrete cavity 45

Figure 31: Eroded concrete cavity in plane SW-NE from TC measurements 46

Figure 32: Eroded concrete cavity in plane SE-NW from TC measurements 46
Figure 33: Gas pressure in the hood of the concrete crucible..47
Figure 34. Gas temperature in the hood of the concrete crucible 48
Figure 35: Approximate gas flow in the off-gas tube measured by the Prandtl tube.............48
Figure 36: Gas release rates as measured in the off-gas line (without H2O) 51
Figure 37. Integrated gas release as measured in the off-gas line (without H2O) 51
Figure 38: Flow rate of coolant water to flood the melt surface..52
Figure 39: Thermocouples in the bottom of the crucible in instrumentation line T2 54
Figure 40: Long term temperatures at the erosion front at the bottom of the cavity..............55
Figure 41: Long term temperatures in the concrete below the erosion front of the cavity......55
Figure 42: View into the open facility with the solidified melt (1) at the central bottom 57
Figure 43: Closer view to the central melt and the rim of the concrete cavity 57
Figure 44: View to melt in the concrete cavity after removal of the protection tube 58
Figure 45: Closer view to the melt surface and the concrete cavity 58
Figure 46: Close-up view showing the rough surface partly covered by ejected debris.........59
Figure 47: Loose oxidic/glassy debris ejected during volcanic eruption................................59
Figure 48: Contour of the melt after the test, taken from the sectioned crucible....................60
Figure 49: Sectioned crucible. View to plane S-N. White lines show the initial cavity...........63
Figure 50: Sectioned crucible. View to plane N-S. White lines show the initial cavity...........63
Figure 51: Close-up view of the solidified oxide with large inner cavity and crust.................64
Figure 52. Inner surface of the upper oxide crust as seen from the bottom of the cavity.......64
Figure 53: Comparison of sectioned crucible with erosion as measured by thermocouples in plane SW-NE 66
Figure 54: Comparison of sectioned crucible with erosion as measured by thermocouples in plane NW-SE 66
Figure 55: Eroded cavity SW-NE: TC measurements compared with sectioned crucible......67
Figure 56: Eroded cavity SE-NW TC measurements compared with sectioned crucible.......67
Figure 57: Axial erosion vs time in plane SW-NE, completed by data from sectioned cavity (dotted lines) 68
Figure 58: Lateral erosion vs time in plane SW-NE, completed by data from sectioned cavity (dotted lines) 68
Figure 59: Axial erosion vs time in plane SE-NW, completed by data from sectioned cavity (dotted lines) 69
Figure 60: Lateral erosion vs time in plane SE-NW, completed by data from sectioned cavity (dotted lines) 69
Figure 61: Evolution of cavity versus time during concrete erosion 70

Figure C- 1: T1│CL - thermocouples on the centre line of the concrete crucible. 87
Figure C- 2: T2│NE - thermocouples in the bottom of the concrete crucible. 88
Figure C- 3: T2│SE - thermocouples in the bottom of the concrete crucible. 88
Figure C- 4: T2│NW - thermocouples in the bottom of the concrete crucible. 89
Figure C- 5: T2│SW - thermocouples in the bottom of the concrete crucible 90
Figure C- 6: T3│NE - thermocouples in the bottom of the concrete crucible 90
Figure C- 7: T3│SE - thermocouples in the bottom of the concrete crucible 91
Figure C- 8: T3│SW - thermocouples in the bottom of the concrete crucible 91
Figure C- 9: T3│NW - thermocouples in the bottom of the concrete crucible 92
Figure C- 10: Thermocouples BT10, BT14, and BT34 in the outer position of the lower crucible, section NE 93
Figure C- 11: Thermocouples BT12, BT15, and BT36 in the outer position of the lower crucible, section SW 93
Figure C- 12: T4│NW- thermocouples in the bottom of the concrete crucible 94
Figure C- 13: T4│SE- thermocouples in the bottom of the concrete crucible Thermocouples BT13 and BT37 in the outer position of the lower crucible, section SE 95
Figure C- 14: T5│NE- thermocouples in the side wall of the concrete crucible 96
Figure C- 15: T5│SE- thermocouples in the side wall of the concrete crucible 97
Figure C- 16: T5│NW- thermocouples in the side wall of the concrete crucible 98
Figure C- 17: T5│SW- thermocouples in the side wall of the concrete crucible 99
Figure C- 18: T6│NE- thermocouples in the side wall of the concrete crucible 100
Figure C- 19: T6│SE- thermocouple in the side wall of the concrete crucible 100
Figure C- 20: T6│NW- thermocouple in the side wall of the concrete crucible 101
Figure C- 21: T6│SW- thermocouples in the side wall of the concrete crucible 101
Figure C- 22: T7│NE- thermocouples in the side wall of the concrete crucible 102
Figure C- 23: T7│SW- thermocouples in the side wall of the concrete crucible 103
Figure C- 24: T8│NE- thermocouple in the side wall of the concrete crucible 104
Figure C- 25: T8│SE- thermocouple in the side wall of the concrete crucible 104
Figure C- 26: T8│SW- thermocouple in the side wall of the concrete crucible 105
Figure C- 27: T8│NW- thermocouple in the side wall of the concrete crucible 106
Figure C- 28: T9│NE- thermocouple in the side wall of the concrete crucible 107
Figure C- 29: T9│SW- thermocouple in the side wall of the concrete crucible 107
Figure C- 30: Long term temperatures at the erosion front in the lower cavity 108
Figure C- 31: Long-term temperatures in the concrete layer close to the erosion front in the lower cavity 108

Figure C- 32: Long-term temperatures at the erosion front of the upper cavity, section SW. Thermocouple BT89 has significant offset after formation of a “new junction”. 109
Figure C- 33: Long-term temperatures at the erosion front of the upper cavity, section NE. The thermocouples show quenching by the water between 13,000 and 18,000 s. 109
Figure C- 34: Argon cover gas flow into the crucible hood..110

1 Introduction

Initiated by the LACOMERA project at the Forschungszentrum Karlsruhe, Germany, a group of large scale experiments is performed that investigate the long term interaction of a simulated corium melt with a cylindrical concrete cavity. This interaction, conventionally nominated “**M**olten **C**orium **C**oncrete **I**nteraction” (MCCI), has been under study since many years, based on small scale laboratory tests with model materials on the one hand [1] and on large scale experiments with high temperature melts in real concrete on the other hand. Such typical experiments of the latter type are the BETA experiments performed 1984 to 1992 at Forschungszentrum Karlsruhe [2]. In these experiments with sustained heated steel and oxide simulant melts, concrete erosion occurred predominantly by the metal melt, in which the decay heat was deposited by induction heating. Later experiments with sustained heated, pure oxide melts gave additional information on specific erosion by UO_2 based melts, see e. g. [3]. These experimental results were used to improve the models for heat transfer and material behaviour in the computer codes that were developed to predict the ex-vessel accident situation in a light water reactor. Nevertheless, substantial uncertainties still persist in the long term calculation of cavity erosion by different computer codes. These uncertainties are mainly related to the partition of the decay power in the melt dissipated for concrete ablation in the lateral and axial directions, respectively. The underlying reason is the poor experimental data base for erosion through oxide melts which is up to now solely one-dimensional [4], and the limited information on the erosion in a layered steel/oxide melt. As a consequence, substantial deviations are predicted in the time for axial basement penetration, or in strong lateral erosion which can undermine containment structures.

To overcome this problem, experiments on 2-d concrete erosion by oxide melts have been started recently at ANL, sponsored by an OECD consortium [5, 6]. These experiments showed, however, unexpected erosion behaviour which is not clearly understood at present. To complement these data for melts with a heated steal layer, Forschungszentrum Karlsruhe together with international partners has also performed further tests in the COMET facility in which the steel fraction of the melt is heated by induction heating [7,8]. These experiments, which are part of the EU sponsored LACOMERA project, are completed by the 3rd and final COMET-L3 test reported here.

Beyond the question of concrete erosion there exists substantial interest in the coolability of melt by adding water to the melt surface during concrete erosion. It is expected that a surface crust will form at the melt/water interface. The open subject is to what degree the surface crust will allow ingression of water to the bulk of the melt, thus extracting part of the decay power from the melt to the evaporating water. This subject is also investigated in COMET-L3.

The present report describes the experiment COMET-L3 which is in many aspects a successful duplication of the COMET-L1 experiment in which, however, unexpected interruption of decay heating limited the duration of the test. The COMET-L3 experiment is performed as a long term MCCI test with simulated oxidic and metallic corium in a cylindrical cavity of siliceous concrete, with decay heat simulation of low decay power, and is carried out under dry conditions in the first phase of the test. The report provides test results during downward and lateral concrete erosion during the first phase of the experiment. After substantial concrete erosion, melt cooling is initiated in the second phase of the test by supplying water to the top of the melt. The influence of the top flooding on melt cooling and ongoing cavity erosion after the flooding is the second objective of the experiment. This second test objective is complementary to the COMET cooling concept by bottom flooding that has been investigated in the EU sponsored ECOSTAR Programme [9].

The COMET-L3 test uses a heated steel melt that is covered by an oxide melt. Decay heat is simulated in the steel melt by electrical inductive heating throughout the course of the test.

The report gives a description of the COMET facility and the operating systems as well as a presentation and analysis of the test results. The experiment was conducted on November 12th, 2005. A short overview of the main test parameters is provided in Table 1.

Table 1: Specifications for COMET-L3

Parameter	**Specification**
Corium simulant	Metal (Fe + Ni) and oxide (Al_2O_3 + CaO)
Melt formation	Thermite reaction
Initial temperature of the melt	~ 1700°C
Initial melt mass	460 kg steel + 160 kg oxide
Concrete type	Standard siliceous concrete
Initial cavity dimension	D_i = 600 mm, H_i = 780 mm
Radial erosion limit	250 mm
Axial erosion limit	190 mm
Simulated decay power	Induction heating at approx. 200-230 kW
Facility pressure	Atmospheric
Cover gas	Argon
Flow rate of the cover gas	50 m^3/h main flow and 2 x 8 m^3/h from windows
Criteria for phase 1 = Dry MCCI	200 - 230 kW heating, flooding to start after ~90 mm downward erosion
Criteria for phase 2 = MCCI with surface flooding	200 - 230 kW heating, initial flooding rate 0.375 litres/s, melt covered by water until end of heating after maximal axial or radial erosion of 190/250 mm, respectively
Criteria for test termination	1) Contact of the melt with a light guide 2) 25 cm radial erosion 3) Porous concrete at the bottom reached 4) Melt stabilized by surface flooding with stop of long-term concrete erosion

2 COMET - L3 Test Design

2.1 Facility description

The central part of the COMET test facility, shown in Figure 1, consists of a test rig with the concrete crucible and the induction coil underneath for simulation of the decay heat. Not shown are the external melt generator, details of the induction heating system with power supply and power control, off-gas system, water supply for melt flooding, a series of measurement and video systems, and the data acquisition systems. The COMET facility and the supporting systems are located in a dedicated building (Figure 2). Due to safety reasons the control room with the equipment for online measurements is located in a bunker next to this building.

The outer crucible consists of a composite protection tube that includes the large test insert, and is designed to withstand higher pressure pulses if they would occur. The test rig is located on a transport car to allow installation and disassembly of the crucible.

The simulated corium melt is generated externally by a thermite reaction (see chapter 2.2) with an initial temperature of about 1700°C and poured into the crucible through a lid in the upper hood. This moment defines the experimental time zero, when the first phase of dry erosion starts. With the decay power deposited in the melt during the course of the test through the induction coil located under the bottom concrete shell, erosion of the concrete is expected to occur in the axial and lateral directions. After substantial concrete erosion, when the melt has eroded some 90 mm into the axial direction, surface flooding will be initiated by supplying water to the top of the melt, which may reduce or even stop the erosion process. If, however, the melt would progress further and eventually contact the light guides at the bottom of the crucible, the test would be stopped by terminating the induction heating. If required, coolant water may be supplied to the porous concrete layer under the concrete crucible, which would in any case stop further downward cavity erosion, thus protecting the induction coil from any damage.

The outer crucible is gas tight; so that all gases generated during the experiment, are collected in the free volume of the crucible and feed through the off-gas system into the ambient atmosphere. A constant argon cover gas flow is injected into the crucible to prevent the accumulation of a burnable gas mixture. In the off-gas system, the main characteristics such as temperature, composition and flow rate of the released gases are measured online.

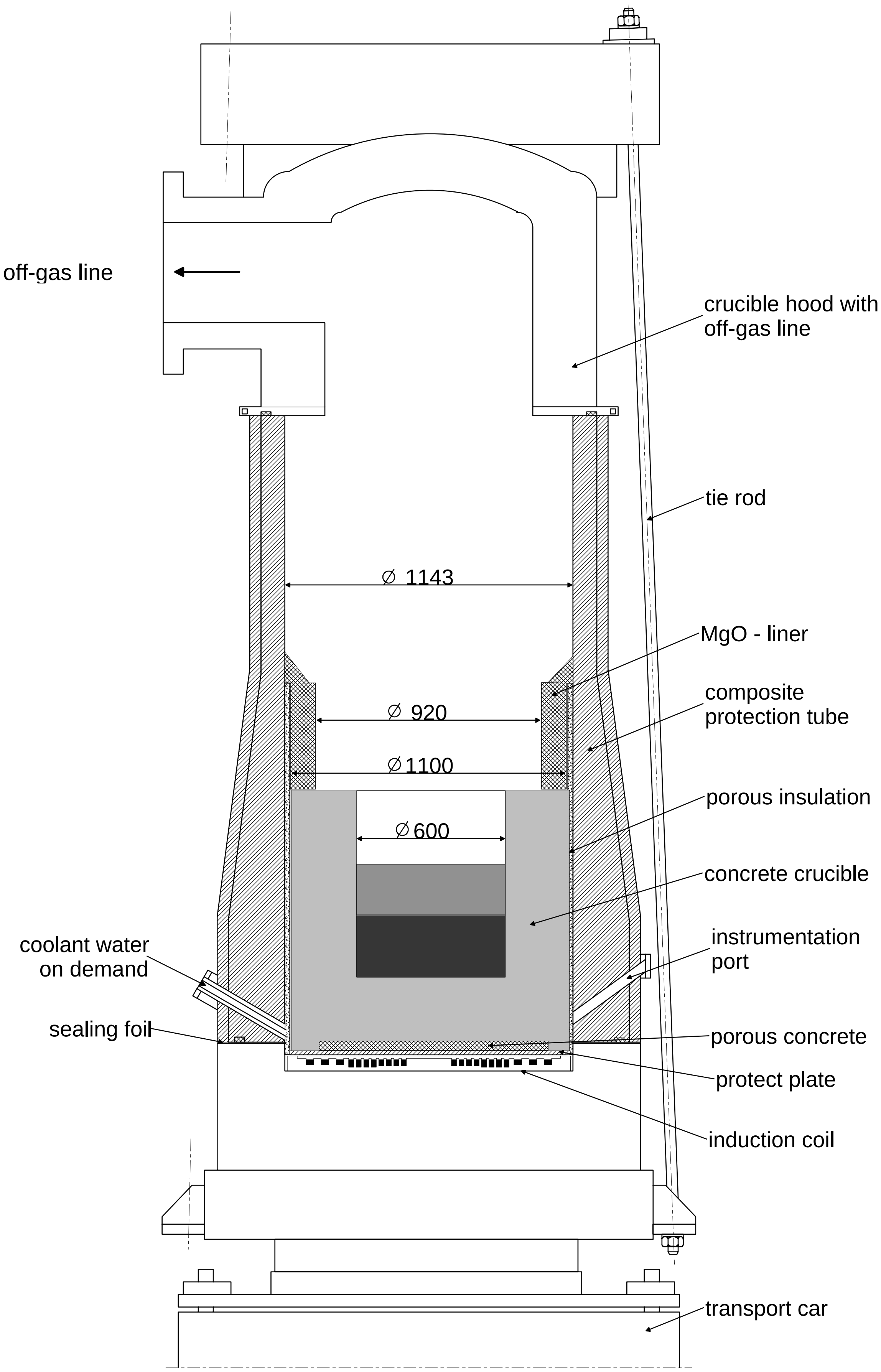

Figure 1: COMET test rig with its main components

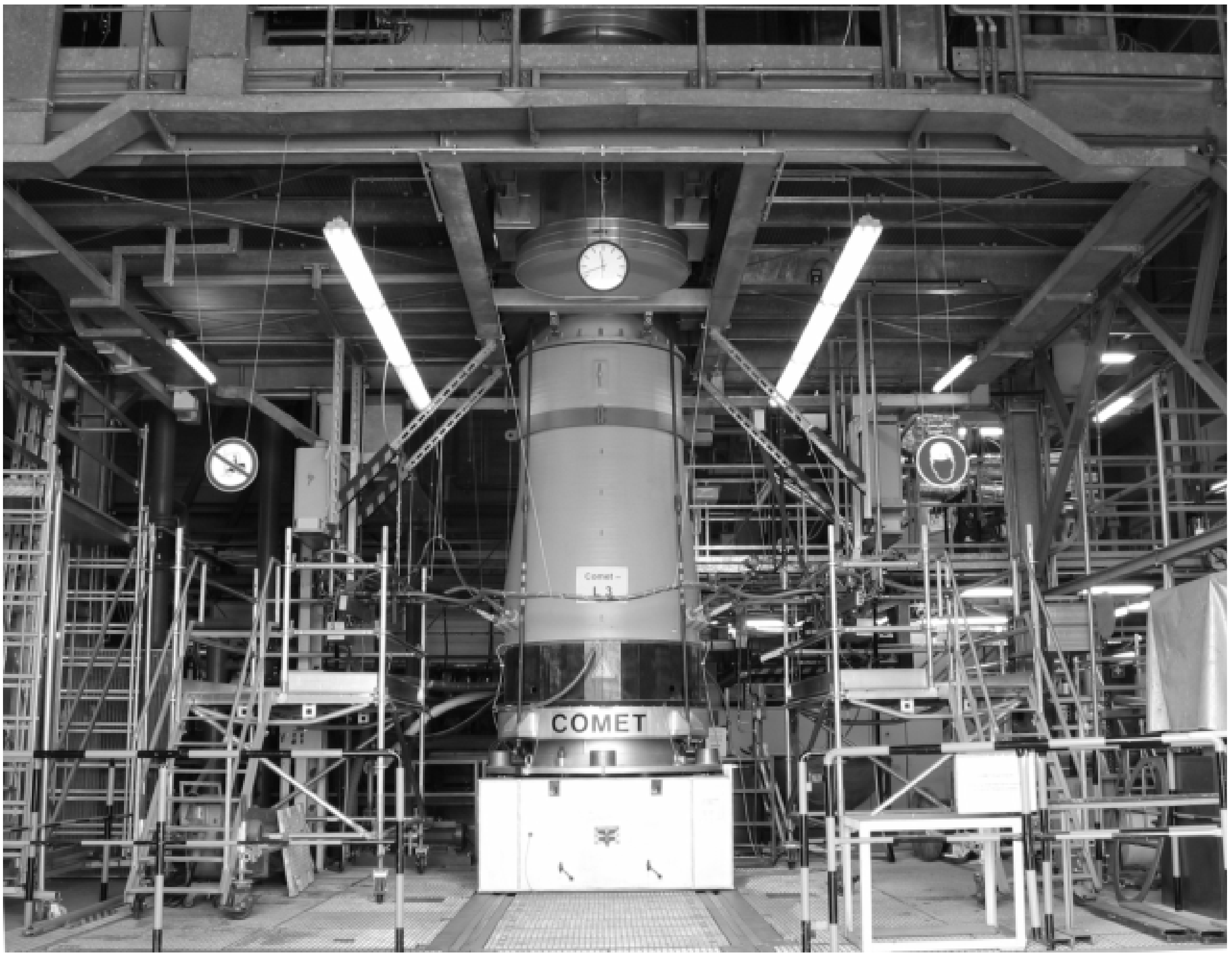

Figure 2: Photo of the COMET facility

The induction coil, which supplies the electromagnetic 1000 cps heating power to the melt, is water-cooled. All other components located on the transport car are fabricated from non-metallic materials to exclude coupling to the induction field. The upper surface of the induction coil is covered by a 5 mm silicone foil, which protects the coil against any water that might be released from the concrete cavity. A 10 mm thin, refractory plate protects the induction coil, if hot melt would penetrate the concrete crucible. The distance between the induction coil and concrete crucible or melt respectively is kept as small as possible to reduce the inductive losses.

Figure 3 gives details of the inner concrete crucible that is fabricated from standard siliceous concrete. The (simplified) composition of the concrete and some of its properties are listed in Table 2

The cylindrical ring of MgO oxide, located above the crucible, is 90 mm thick and has an inner diameter of 920 mm. The ring is stable against thermal and chemical attack so that the melt may erode only the concrete cavity below. The gap between the concrete crucible with the

MgO ring and the outer protection tube is filled with coarse silica gravels used as a thermal insulation (Figure 1).

The inner structure of the composite protection tube is formed by refractory concrete and the outer shell of gas-tight, high temperature epoxy with glass fiber. The upper hood is a steel structure with inner ceramic liner and is connected to the off-gas tube. The role of the four tie rods is to tighten the upper and lower parts of the facility and maintain its integrity in case when inner mechanical loads act on the structure.

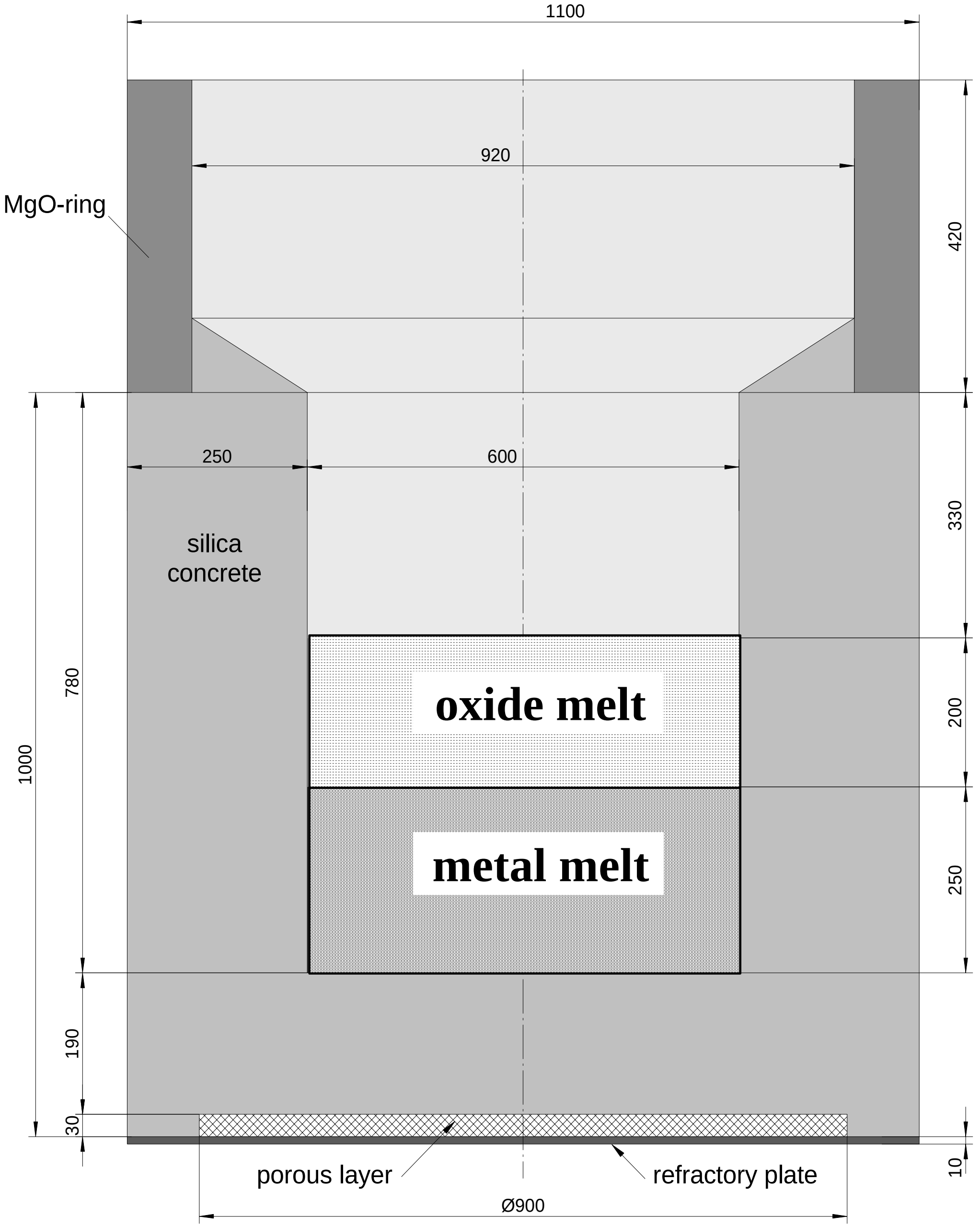

Figure 3: Dimensions of COMET-L3 crucible

Table 2: Properties of the siliceous concrete for the crucible

Parameter	
SiO_2 70.3 weight %	blast furnace cement CEM III/B 32,5 NW/HS
$Ca(OH)_2$ 13.55 weight %	density of the concrete is 2220 kg/m^3
Al_2O_3 6.58 weight %	decomposition enthalpy is 2075 kJ/kg
$CaCO_3$ 5.46 weight %	
free H_2O 4.11 weight %	

Two redundant water supply lines are connected to the porous concrete layer under the bottom of the crucible, to which water may be supplied on demand (Figure 3). This layer shall act as an efficient heat sink when later in the test the melt should propagate to the lower bottom of the concrete crucible, and the residual heat from concrete and melt must be removed to maintain the integrity of the induction heating system. Two instrumentation ports to the lower concrete cavity are used for thermocouple and light guides instrumentation of the crucible.

To allow sufficient time and material for the erosion process, the cavity of the crucible is fabricated as a massive structure of siliceous concrete (Figure 3). The outer diameter is 1100 mm as limited by the COMET facility. The inner diameter is 600 mm, to allow a maximal lateral erosion of 250 mm. The thickness of the bottom of the crucible is 190 mm, which limits the maximal downward erosion. This thickness is limited by the maximal distance from the induction coil, and shall allow supply of 250 kW net power to the melt.

Minor deviations from the inner cavity dimensions occurred due to imperfections of the fabrication of the concrete crucible: The inner diameter is 589 mm instead of 600 mm, and the thickness of the bottom of the crucible is 193 instead of 190 mm, with minor influence on the positions of the thermocouples in the lower crucible. The consequences for the determination of the eroded cavity and of the erosion rate are, however, negligible.

The initial height of the metal and oxide phases are 250 mm and 300 mm, respectively, not taking into account the porosity of the melt by gas release.

2.2 Melt composition and melt generation

With the given dimensions of the inner cavity, the masses of metallic and oxidic melts were selected to fill the cavity – without void – with 250 and 200 mm, respectively (Figure 3). The steel height decreases during the test because of the radial cavity erosion, while the oxide thickness would increase, as all liquid concrete products accumulate in the oxide layer.

From the experimental point of view, the initial metal height of 250 mm has the advantage, that the melt in its final stage would not be too shallow, thus representing relevant accident scenarios. However, due to the nature of induction heating, the simulated decay heat is generated in the steel layer only, so that heating of the oxide melt is restricted to interfacial heat transfer between the metal and oxide layer.

The required steel mass (90 w% Fe + 10 w% Ni) for h = 25 cm is 459 kg, liquid density 6500 kg/m^3. The required oxide mass is 159 kg for h = 20 cm, assuming a typical density of the generated oxide melt of 2810 kg/m^3. This density was determined in the preceding COMET-L1 test by measurement of the melt height in the thermite crucible. Table 3 summarises the main characteristics of the melts.

Table 3: Planned characteristics of the initial oxide and metal melt in the concrete cavity

	Metal	Oxide
mass of melt:	459 kg	159 kg
initial height of melt	250 mm	200 mm
volume of melt	0.0707 m^3	0.0566 m^3
composition of melt	90 w% Fe, 10 w% Ni	56 w% Al_2O_3 and 44 w% CaO
liquid density at ~1700°C	6500 kg/m^3	2810 kg/m^3
Contact surface of melt and concrete	0.754 m^2	0. 377 m^2

The melt is generated by a thermite reaction in a separate reaction vessel located above the test facility. The basis for this reaction is a thermite powder that provides liquid Al_2O_3 and iron by strongly exothermic reaction.

$$Al + Fe_2O_3 \rightarrow Al_2O_3 + Fe + h_{chem} \qquad (1)$$

Further additives are added to the thermite powder. For the steel melt, 10 w% Ni are added to the Fe melt, resulting in 459 kg Fe + Ni melt. Ni lowers the solidification range and represents components of the stainless steel of core structures. Furthermore, from the point of induction heating, Ni makes coupling to the induction field more stable if the steel temperature should strongly decrease and approach the Curie temperature. No further metals are added as they would no more exist in metallic form at that time of the accident for which this long-term MCCI experiment is representative (e.g. no Zr or Cr).

The total oxide melt mass generated in the thermite vessel is 504 kg, composed of 56 w% Al_2O_3 and 44 w% CaO. CaO is added to the thermite mix to lower the freezing range and the viscosity of the oxide melt, with the objective to increase the similarity to the corium melt, however at reduced temperatures. The fraction of oxide melt poured into the crucible is 159 kg, the residual 341 kg are retained in the slag wagon. During the course of the experiment, the silica from the decomposing concrete will mix to the oxide melt in the concrete crucible, and thus will change the oxide properties.

Table 4 shows the composition of the thermite mix and of the resulting high temperature melts after completion of the thermite burn.

Table 4: Melt generation by thermite reaction in COMET-L3

Thermite mixture		**Produced melt**	
Thermite “Th”	559.29 kg	275.70 kg Fe	283.59 kg Al_2O_3
Fe pins	137.85 kg	137.85 kg Fe	-
Ni pellets	45.95 kg	45.95 kg Ni	-
CaO	220.57 kg	-	220.57 kg CaO
total	**963.66 kg mix**	**459.50 kg Fe+Ni**	**504,16 oxide**

The thermite reaction in the thermite vessel is normally completed within some 30 seconds. After additional 60 s for the metal and oxide melts to separate completely into the denser steel and the less dense oxide layer, melt pour starts: All metal is poured into the test crucible. When the weight loss of the thermite vessel indicates release of additional 159 kg oxide melt, the remaining oxide melt is directed into the slag wagon. The time to pour the melt into the concrete crucible is 40 s typical.

The initial temperature of the melt is expected with 1700°C. This is sufficiently high so that pour of the melt from the thermite vessel occurs without problem. To reach this temperature, preheating of the thermite powder mixture is performed by electrical heater rods inserted into the thermite powder in the thermite vessel over more than 24 hours. The initial temperature of the melt is measured by a W-Re- thermocouple in the spout during pour of the melt. This is a well-established, reliable technique.

2.3 Decay heat simulation

The simulation of the decay heat in the melt is achieved by induction heating which couples to the metallic fraction of the melt. The horizontal induction coil, located under the crucible, forms the resonance circuit together with a set of 27 high voltage capacitors driven by a 1 kHz power supply. The maximum inductor voltage is 2600 V; the maximum current is 1200 A. The equivalent rated upper heating power for a non-magnetic melt is 400 kW. The heating power deposited in the melt is determined online by the actual measured total power from which the losses by ohmic resistance and by the electromagnetic stray field are subtracted. These losses were determined in separate system tests, depending on voltage and currents of the induction circuit. In addition, a complete balance of all electric cooling circuits confirms the validity of this approach.

According to the test plan, net inductive heating of the melt shall be at the 200 kW power level. The resulting mean power densities, referred to the concrete surface which is in contact with the steel melt and referred to the volume of the metal melt, respectively, are given in Table 5

Table 5: Planned power densities in COMET-L3

P_{Net}	Q_{Surf}	Q_{Vol}
200 kW	265 kW/m²	2829 kW/m³

The net heating power may vary substantially as the coupling efficiency between induction coil and metal melt may change during the test. To compensate for this effect, the inductive power is adjusted by control of the inductor voltage. This is performed manually by the operator, based on the displayed actual power history. All relevant data of induction heating are monitored for detailed evaluation.

There are three processes influencing the electromagnetic coupling:

- Agitation and variation of the void in the melt: for higher void the efficiency of the coupling is reduced. Strong high frequency power oscillations are characteristic for the early MCCI processes. Solidification of the melt, in whatever structure, leads to more stable coupling.
- The reduced distance between melt and induction coil, which is a consequence of the concrete erosion, improves the coupling.
- The electrical properties of the metal melt change with temperature. The most important property for the actual melt is the magnetic permeability which increases strongly below Curie temperature (400°C). This may occur after solidification and further cool down of the steel, resulting in a higher efficiency of heating.

In the present test, the induction heating system was started already 150 seconds before melt pouring, so that melt heating starts as the melt contacts the bottom of the crucible. Heating will be terminated when the maximum allowed cavity erosion did occur or when stable melt cooling is achieved.

2.4 Water supply and off-gas systems

There are two independent systems for water supply to the melt surface or to the outer concrete crucible, respectively.

To flood the surface of the melt as specified for phase 2 of the test after exceeding 90 mm downward erosion, a shower will be activated in the hood of the crucible that delivers 22.5 liter water/min = 0.375 litres/s. The height of the water layer that will form on the melt surface, shall be limited and maintained between 50 and 70 cm above the initial upper melt surface, which corresponds to the half or full height of the ceramic ring on top of the concrete crucible. This limitation shall avoid penetration of water into the gap between the outer concrete crucible and the cylinder wall. The water layer shall be maintained during the further test period to study the influence of top flooding.

The other option is to flood on demand - and after end of heating - the bottom and sidewall of the concrete crucible by introducing water through the lower protection tube (Figure 1) to the porous concrete layer, 30 mm thick, under the concrete crucible. This water would eventually also flood the insulation gap between crucible and protection tube, that is filled with silica gravels. The flooding water is supplied from a reservoir located some 2 m above the concrete crucible. This flooding shall stabilize the concrete crucible with the melt in case of strong or uncontrolled cavity erosion and shall exclude attack of the induction coil by the hot (solidifying) melt. This coolant water is not expected to penetrate into the melt, so that the concrete and melt remain in the status as they were at the time when heating was stopped. Under the crucible, a 10 mm thick protect plate of refractory oxide material is located to protect the COMET induction coil in case that melt should penetrate through the bottom porous layer (Figure 1).

The off-gas system through which the gases and steam from concrete erosion and subsequent flooding are released to the atmosphere is connected to the crucible through the hood. The system consists of a horizontal 1 m long tube with a ceramic liner of 400 mm inner diameter, a vessel to retain any melt which could be ejected from the test vessel, and an 11 m long horizontal steel tube with 500 mm inner diameter, exhausting the gas flow to the atmosphere outside of the building.

The large volume of the off-gas system excludes pressure build-up in the test vessel even for high gas rates. The off-gas system is preheated to 110°C before and during the experiment to exclude condensation of the steam. The end of the off-gas tube is closed in the beginning by a paper diaphragm, which allows argon inertisation before starting the test. This diaphragm is expelled by the first hot gases produced during pouring of the melt. Off-gas analyses are performed by instrumentation located along the off-gas tube, including a mass spectrometer for chemical analysis.

At the end of the off-gas tube, a heater plug ignites the off-gas if the concentration of the burnable gases is sufficient. A standing flame usually characterizes the first phase of dry concrete erosion when high amount of hydrogen is released.

2.5 Instrumentation and data acquisition

The COMET facility is equipped with a multitude of instrumentation to monitor and control the experiment and to collect data for subsequent evaluation. All data are stored and displayed on a PC data acquisition system as well as online registration using chart recorders and printers. Moreover, several video systems are used to observe the experiment, including two video installations, which are directed from the crucible hood onto the surface of the melt. These systems are especially useful to observe all processes which are related to crust formation on the melt surface and during cooling. Besides a conventional video camera, an infrared (IR) video camera was installed on top of the hood of the crucible, viewing through a sapphire window on the surface of the melt. This camera operates in the IR wavelength range from 3.4

to 5.0 μm and produces a video film. Additionally every 15 s, high quality digital pictures are taken during the first 60 min. This allows determination of localized temperatures of the surface of the melt or of the upper crust throughout the experiment. As for any IR system, to derive the temperature or the emitted radiation from the surface, assumptions have to be made for the emissivity of the surface.

The measurement signals are collected to characterise the information written below:

- Electrical induction heating: Total power, net power, various voltages and currents, inductor frequency, control temperatures and coolant flows in the electrical components.
- Generation and pouring of the thermite melt: mass of the melt in the thermite reaction vessel, temperature of the melt during pouring, signals to control the pouring process.
- Coolant flow to the crucible: water flow rate, water pressure, approximate height of water level during flooding.
- Upper crucible hood: temperature and pressure in the gas room, control and rate of the argon cover gas flow.
- Off-gas system: gas flow, temperature and pressure; gas composition by on-line quadrupole mass spectrometry.
- Control signals and conditions of the experimental hall.
- Thermocouples and light guides in the concrete crucible and the surrounding protection tube as described below in detail.

The assignment of the measurements to the data acquisition system is listed in Appendix B.

Instrumentation of the concrete crucible is given in Figure 4 to Figure 6. All indicated thermocouples are of the type NiCr-Ni. They fail at ~1350°C, and therefore operate until melting of the concrete does occur. Their failure indicates arrival of the melt front. These thermocouples are however unable to measure the temperature of the melt. It is important that the thermocouples give sufficient information during the test about the actual position of the melt front to control the course of the test. Therefore, the instrumentation is arranged in two perpendicular planes of the crucible, namely SW-NE and NW-SE, given in the top view in Figure 4. The complete instrumentation of the planes SW-NE and NW-SE is shown in Figure 5 and Figure 6, respectively. The positions of the thermocouples referred to the centreline and to the bottom of the cavity are listed in Table 6 and Table 7. The total number of NiCr-Ni thermocouples is 90. This number is limited by the high quality amplifiers which are required.

No thermocouples are installed to measure the temperature of the melt in the crucible during the erosion, because no stable thermocouples exist for this critical application. W-Re-thermocouples that were installed in the previous COMET-L1 test [7], failed very early in the test phase before showing any valid temperature because of the destruction by the very aggressive melt, especially because of the Fe content.

As we can not be sure to detect any critical position of the melt front by the thermocouples, additional safety relevant instrumentation in form of light guides is located in the outer sections of the crucible, indicated in Figure 5 and Figure 6 by crosses (**x**). Heating of the melt is planned until the melt approaches the light guides. If they are interrupted by the melt, heating is switched off immediately, and the melt cools down. Coolant water may be supplied to the outer crucible if required to prevent further erosion as described in section 2.4.

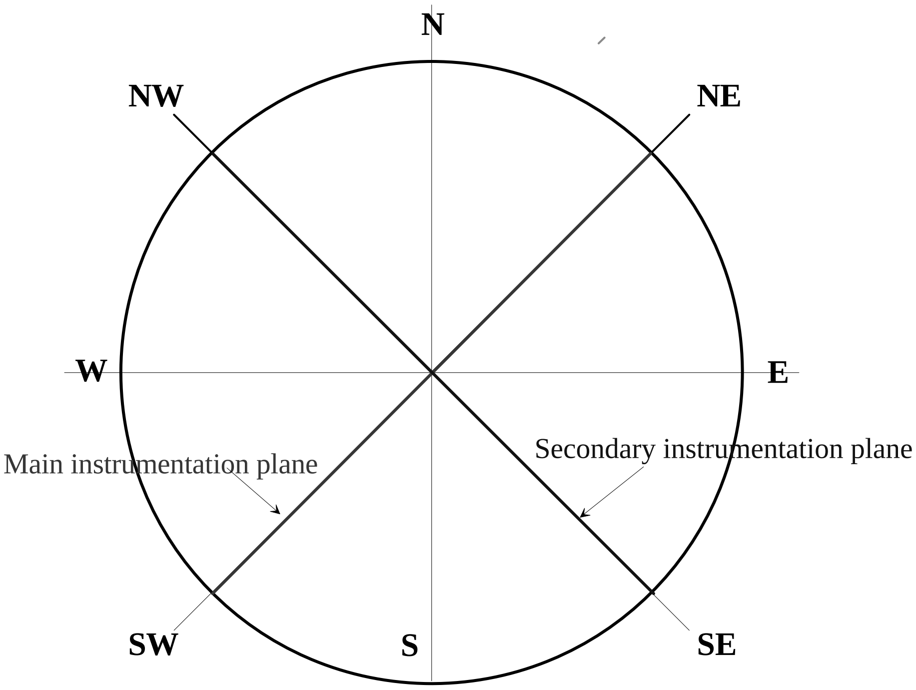

Figure 4: Orientation of the instrumentation in planes NW-SE and SW-NE (top view)

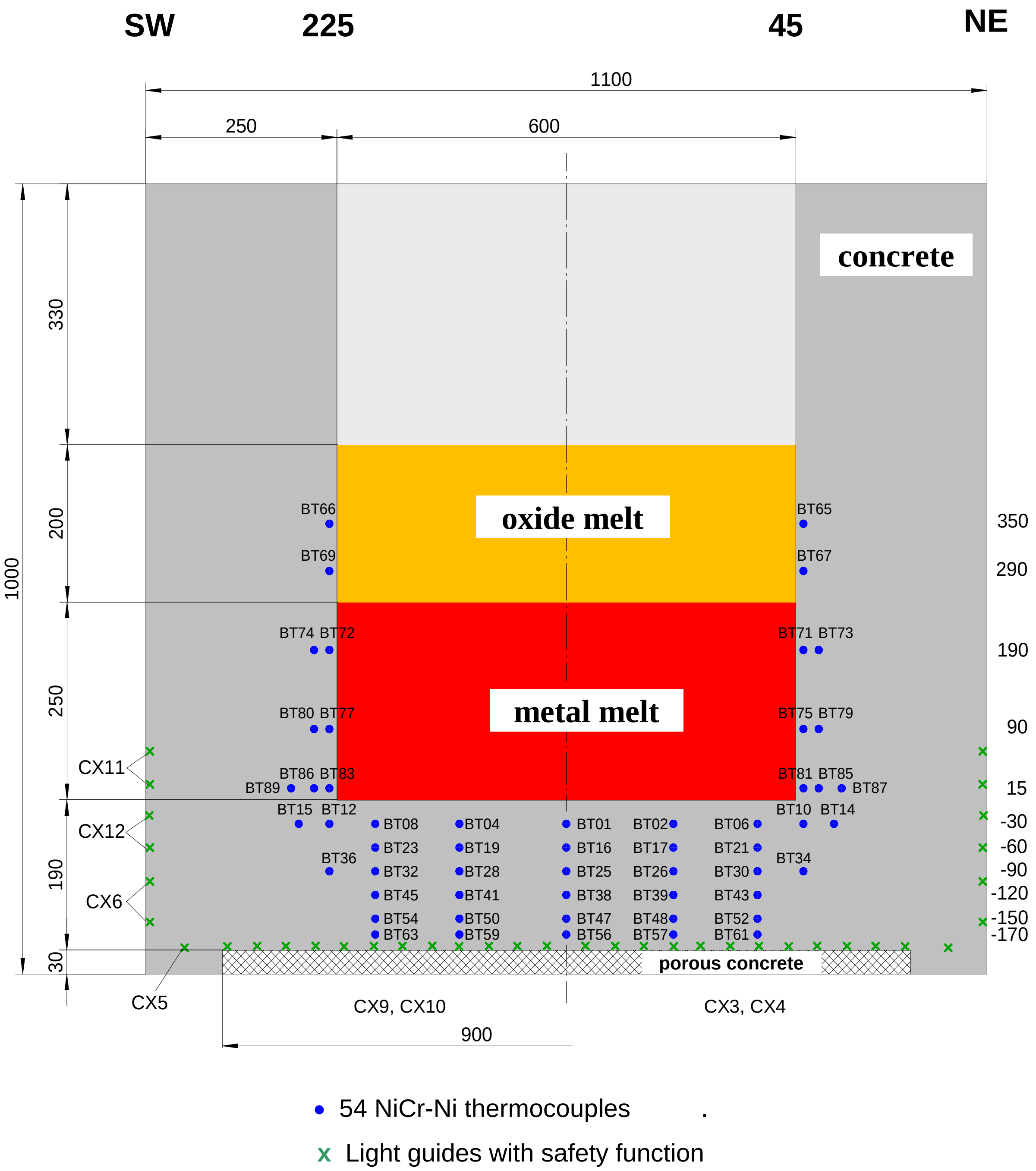

Figure 5: Thermocouple and light guides instrumentation in plane SW-NE

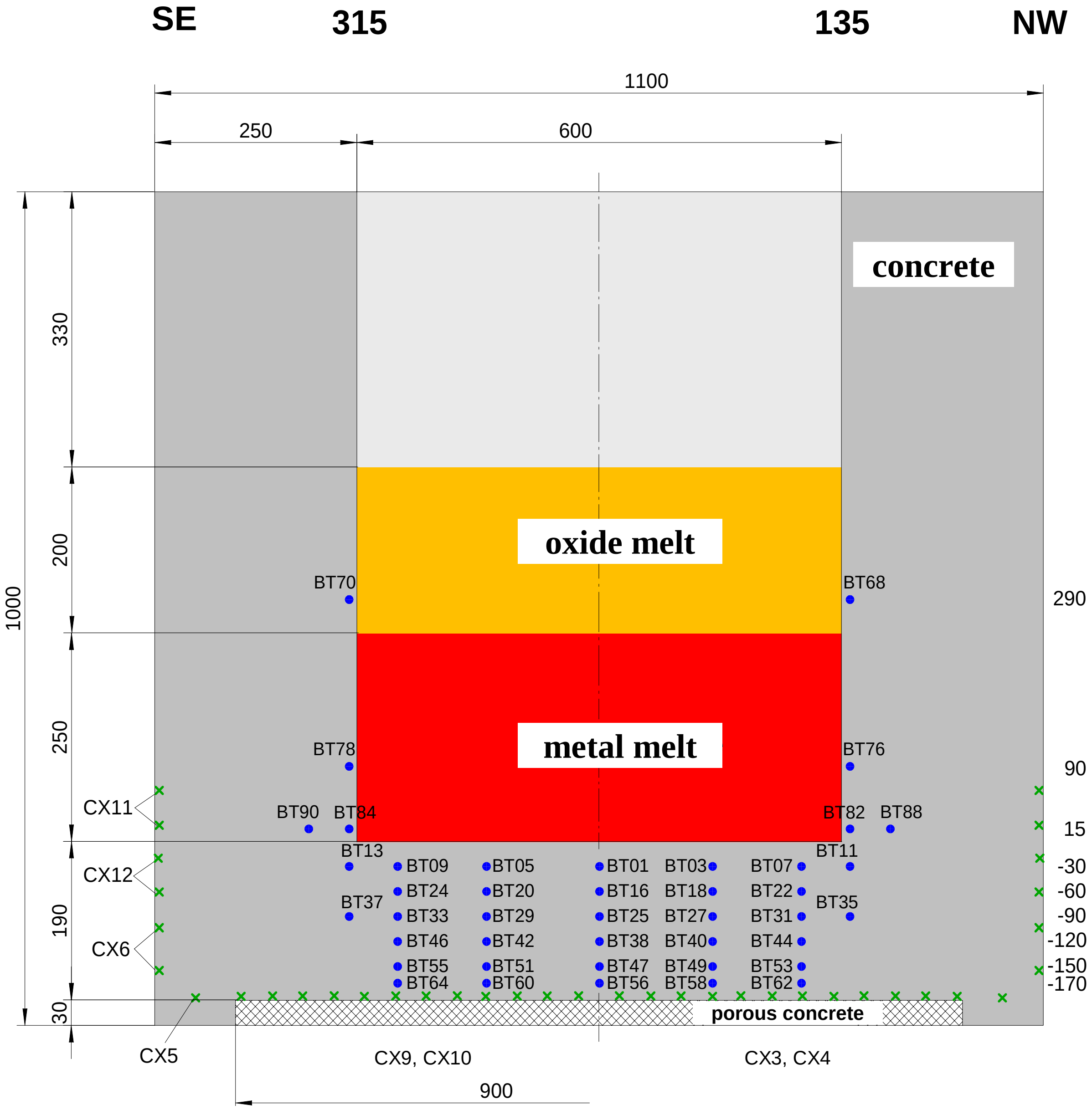

● 36 NiCr-Ni thermocouples (without TCs on centreline)

x Light guides with safety function

Figure 6: Thermocouple and light guides instrumentation in plane SE-NW

Table 6: Position of NiCr-Ni Thermocouples in Plane SW-NE in COMET-L3

Height mm			**SW (225°)**			**Radius, mm**					**NE (45°)**		
	-360	**-350**	**-330**	**-310**	**-250**	**-140**	**0**	**140**	**250**	**310**	**330**	**350**	**360**
350				BT66						BT65			
290				BT69						BT67			
190			BT74	BT72						BT71	BT73		
90			BT80	BT77						BT75	BT79		
15	BT89		BT86	BT83						BT81	BT85		BT87
-30		BT15		BT12	BT08	BT04	BT01	BT02	BT06	BT10		BT14	
-60					BT23	BT19	BT16	BT17	BT21				
-90				BT36	BT32	BT28	BT25	BT26	BT30	BT34			
-120					BT45	BT41	BT38	BT39	BT43				
-150					BT54	BT50	BT47	BT48	BT52				
-170					BT63	BT59	BT56	BT57	BT61				

Total number of TCs in plane SW-NE = 54

Table 7: Position of NiCr-Ni Thermocouples in Plane SE-NW in COMET-L3

Height mm			**SE (315°)**			**Radius, mm**					**NW (135°)**		
	-360	**-350**	**-330**	**-310**	**-250**	**-140**	**0**	**140**	**250**	**310**	**330**	**350**	**360**
350													
290				BT70						BT68			
190													
90				BT78[1]						BT76[1]			
15	BT90			BT84						BT82			BT88
-30				BT13	BT09	BT05	BT01	BT03	BT07	BT11			
-60					BT24	BT20	BT16	BT18	BT22				
-90				BT37	BT33	BT29	BT25	BT27	BT31	BT35			
-120					BT46	BT42	BT38	BT40	BT44				
-150					BT55	BT51	BT47	BT49	BT53				
-170					BT64	BT60	BT56	BT58	BT62				

Total number of TCs in plane SE-NW = 36, without TCs at r = 0, which are counted in Table 6

[1] The 2 NiCr-Ni thermocouples BT76 and BT 78 use Pt-Rh compensating cables. This has no influence on the registration of the failure time.

3 Experiment Preparation and Test Procedure

3.1 Preparation of the concrete crucible

A very laborious task is the fabrication of the concrete crucible with the embedded instrumentation. Figure 7 shows the preparation of the instrumentation, namely the light guides with their black plastic sheathing, located in the lower plane of the crucible, and the thermocouples that are fixed to rods of glass for exact positioning. Figure 8 and Figure 9 show different steps to fill in the liquid concrete in the prepared mould. Figure 10 shows the filled mould with the central core that represents the cavity in the crucible. Figure 11 shows the crucible upside down with the flat cavity that is to be filled with porous concrete. Some thermocouple lines that detect the erosion front in the bottom concrete layer, pass this cavity. The curing time for the crucible was more than 4 weeks so that the concrete complies with the technical specifications.

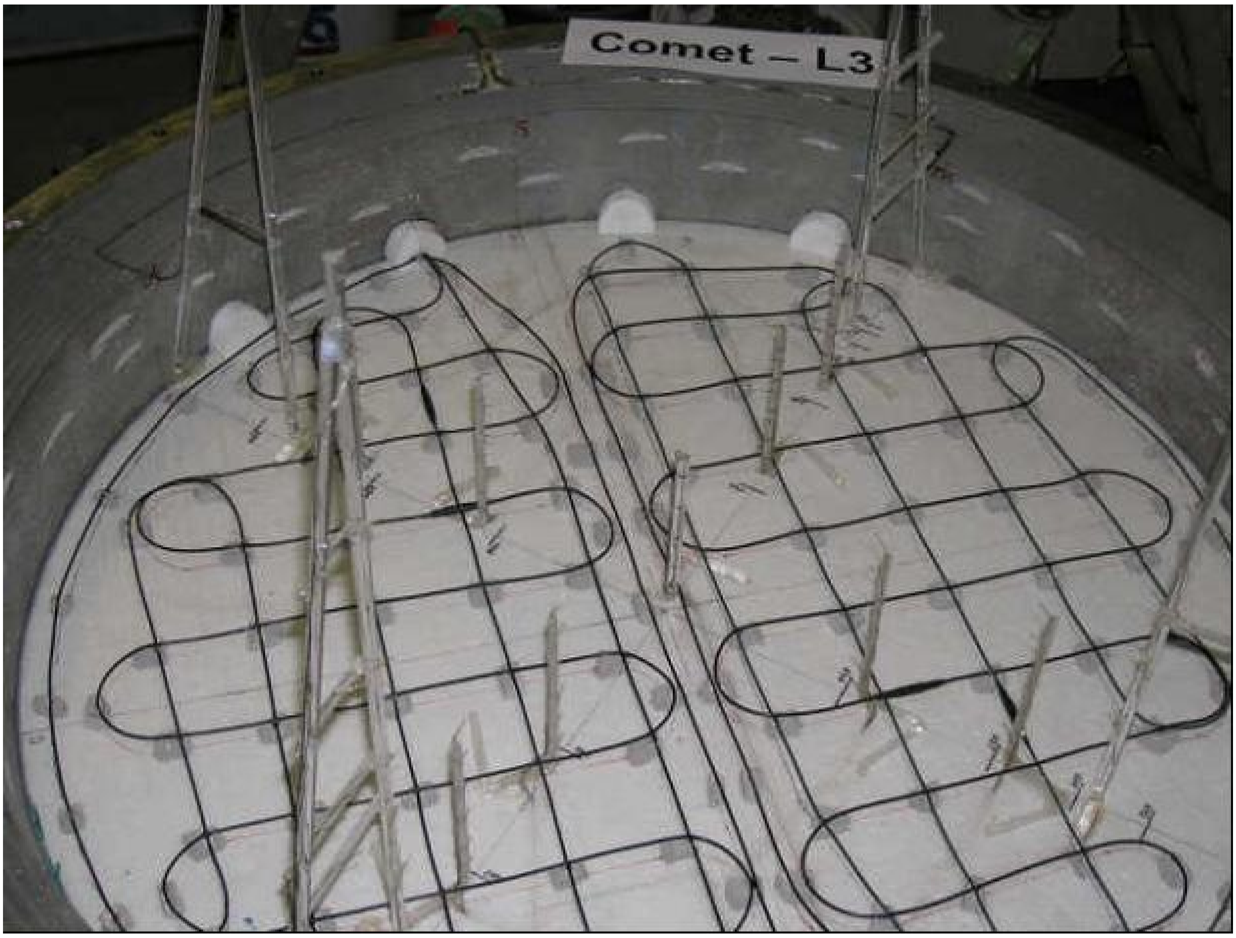

Figure 7: Instrumentation during crucible fabrication: Light guides (black sheeting) and thermocouples fixed to glass rods

Figure 8: Fabricating the bottom of the concrete crucible

Figure 9: Fabricating the concrete crucible

Figure 10: The mould for the cavity filled with concrete

Figure 11: The lower side of the concrete crucible with the 30 mm deep cavity

The cavity will be filled with porous concrete. Some thermocouple lines which shall detect the erosion front in the bottom concrete layer, pass this cavity.

3.2 Planned performance

A brief overview of the planned test is given in Table 8.

After preparation of the melt through thermite ignition in the external thermite vessel, **phase 1** of the test starts with pouring the melt into the crucible, with a typical duration of 30 s. Induction heating is operating at the maximum induction voltage of 2.6 kV, which is expected to generate the specified net heating power of 200 kW in the melt. This heating power should be maintained between 220 and 230 kW until the declared end the test phase.

During phase 1 of the test, we allow dry concrete erosion into the downward direction until approximately 90 mm are eroded, corresponding to the 3rd level of thermocouples in the bottom plate. This phase may take about 600 s. Then, **Phase 2** of the test is started by flooding the surface of the melt through the shower from the hood of the crucible. The flooding rate is set to 0.375 kg water/s. The water layer shall reach a height of 50 to 70 cm which will be maintained by actuating the shower flow. Heating of the melt shall be maintained at the previous power level, i.e. some 200 kW. Further erosion of the concrete will be detected online, and the formation of surface crust and cooling processes are registered by the video cameras and the measurement systems If arrest of the melt should not occur, the melt is allowed to erode the concrete cavity until the lowest level of thermocouples or the light guides detect arrival of the melt. Then, induction heating will be terminated.

The subsequent actions aim at stabilizing the melt during its solidification and shall protect the facility. Therefore, after a period of several minutes, flooding of the porous concrete layer under the concrete crucible is started and the coolant water is allowed to fill the insulating lateral gap between the concrete cylinder and the protection tube. Thus, cooling occurs from all sides. Nevertheless, complete cool-down of the solidifying melt may take several hours. Therefore the coolant water will be maintained accordingly and the temperature registration will be continued.

Two days after the test, careful inspection and disassembly of the test rig will start. Sectioning of the solidified melt in the residual crucible will be performed to complete post test analysis.

Table 8: Planned conduct of COMET-L3

Time, s	Event
- 600	Main argon cover gas flow 50 m^3/h
- 150	Start of induction heating system with 2.2 kV induction voltage
-90	Ignition of thermite
-20	Increase induction voltage to 2.6 kV
0	Start of test **phase 1** with melt pour to crucible, 460 kg steel melt + 160 kg oxide melt
~30	End of pouring
~60	Hood closed, melt heated internally by induction power, concrete erosion in progress
> 120	Maintain net heating power between 200 and 230 kW
~600	After ongoing axial and radial erosion, melt reaches the – 90 mm erosion level. **Phase 2** initiated by start of surface flooding through activation of the shower with 0.375 kg H2O/s.
further on	Maintain net heating power near 200 kW -230 kW. Keep melt surface covered by water from the shower. Observe melt propagation into axial and radial direction and influence of top flooding
further on	In case of further concrete erosion, allow melt propagation until lowest thermocouples or light guides detect melt near the bottom line of the crucible. Terminate induction heating.
subsequently	After some minutes of melt cooling without heating, start flooding the porous bottom layer and the porous lateral insulation to protect the facility. Observe cool down of the solidifying melt.
further on	Maintain cooling from top, bottom and sidewalls as required, possibly over hours
post test	After more than ~ 40 h cool down, start post test inspection and dismantling of the crucible

3.3 Course of the test

The test was conducted on November 12, 2005, starting with the pour of the melt at 11:00 local time. Several hours before the test, the experimental team made the final preparations of the test. At 10:25 the personal left the experimental hall. Control of the experiment took place from the control room with all equipment for online measurements and control. The test proceeded as planned. The realized test sequence is given in Table 9. Time zero in the table and in all diagrams refers to start of melt pour which occurred at 11:00 o’clock.

Table 9: Sequence of COMET-L3 as observed during the test and from video-film

Time, s	Event
until -90	Test preparation as planned, induction coil operating
-90	Ignition of thermite powder, thermite burn complete after 60 s, separation of metal and lighter oxide phases by segregation
0 → 200	Start of 636 kg melt pour: 425 kg metal + 211 kg oxide melt with 1665°C, completed after 24 s. Hood of crucible closed after 38 s. Dry erosion of concrete cavity: Melt very intensively agitated until 60 s, some melt splattered to the MgO liner. Melt agitation somewhat reduced until 200 s, some melt ejections driven by gas release. Simulated decay power below 200 kW: from 140 to 170 kW with major oscillations, at maximum allowed input voltage of 2.6 kV. Hydrogen flame at end of off-gas line ends after 115 s. Flow meter inserted into off-gas tube at 180 s.
200 → 400	Agitation of melt pool continuing. Melt reaches 30 mm downward erosion at 220 s. With progress of downward erosion, slow increase of net induction power from 180 to 200 kW with 2.61 kV constant voltage. Some periods show transport of dark material (oxide crust or splashed concrete) to the free surface of the oxide melt, which is then dissolved in the hot oxide. Surface of the oxide melt layer further on bright and well agitated. Viscosity of the oxide slightly increasing, reaches a maximum at ~350 s. Flow of the oxide melt is upwards at the concrete wall, driven by gas, and downwards in the centre. Main gas flow at the sidewalls, but gas bubbles penetrate also through the central surface of the oxide. Moderate steam flow at the end of the off-gas tube.
400 → 500	Some further melt eruptions with dark particles/crusts transported to the surface of the melt. Net power increases from 210 to 230 kW at 500 s. Off-gas with condensing steam flow at end of off-gas line.
500 → 800	To maintain 200 kW, reduction of induction voltage to compensate for the higher induction efficiency because of ongoing downward erosion: at 520 s: from 233 kW to 205 kW (1070 kW total at 2.37 kV) at 590 s: from 235 kW to 200 kW (943 kW total at 2.20 kV) at 690 s: from 250 kW to 209 kW (820 kW total at 2.01 kV) Downward erosion reaches 60 mm at 540 s and 90 mm before 800 s. Melt bright and well agitated. Eruptions with transfer of dark particles are reduced, steady melt conditions.
800 →1000	Top flooding initiated by shower at 800 s with 0.375 litres/s after failure of 2 thermocouples in the -90 mm plane. Strong steam flow in off-gas line. Melt covered by water after about 10 s. Surface of melt bright under the water layer, no eruptions from the melt surface due to water contact. At 860 s, some parts of the surface become darker (quenched), others are still bright. Power after voltage reduction 220 kW net/738 kW total at 1.86 kV. At 880 s surface of melt darkens, 3 to 4 spots remain bright. Some gas driven melt eruptions have little effect on crust formation. At 920 s, 1 hot spot remains on the surface, otherwise the surface is dark. Induction power again reduced to 200 kW/650 total. At 940 s melt surface totally dark. At 950 s, lights on in crucible, shows intensely boiling water layer on dark surface. Structure of surface can not be identified. Flooding by shower continues. Power at 975 s: 210 kW/670 kW total at 1.77 kV. Short “lights off” confirms that surface is totally dark (quenched), no hot spots exists. Water layer several cm thick.

1000 → 1750	Top flooding by spray continues. Steady conditions with moderate boiling. At 1025s, downward erosion reaches 120 mm level. 1060 s: Net power to the melt is relatively constant, that means no fast fluctuations as would be caused by an intensely agitated metal melt: Metal fraction has probably formed a stable geometry. At 1100 s, camera view changed to wide angle. At 1120 s, induction power 213 kW/675 kW total at 1.76 kV. Absence of power fluctuations indicates stable metal layer. Surface crust totally dark as confirmed by short “lights off”, and covered by a boiling water layer. Further power readings without readjustment of induction voltage shows slow increase of heating efficiency by ongoing downward erosion: 1200 s: 216 kW/675 kW total at 1.76 kV 1320 s: 216 kW/674 kW total at 1.76 kV 1390 s: 220 kW/675 kW total at 1.76 kV 1450 s: 220 kW/674 kW total at 1.75 kV 1520 s: 218 kW/674 kW total at 1.75 kV 1600 s: 225 kW/680 kW total at 1.75 kV 1730 s: 229 kW/685 kW total at 1.75 kV. At 1300 s, water level rises to mid of MgO ring. At 1520 s, water level reaches some 10 cm below upper edge of MgO ring. Radial erosion by metal layer is close to 60 mm (BT 87 – BT 90). H2 content detected in off-gas is less than 3 %. No increase of H2 content had been observed during flooding. At 1700 s, flooding stopped as water level reaches upper edge of MgO ring. Maximum of steam/gas release as observed by video camera from the hood is slightly north of the central surface.
1750 → 1878	At 1760 s, start of 1st volcanic eruption of melt through surface crust. Bright melt particles ejected into the water layer, causing intense boiling but no pressure spikes. Eruption ends after 120 s at 1870 s. Centre of the eruption as viewed through the water surface, is slightly west of the central surface. At 1825 s, again reduction of induction voltage: Net power from 240 kW to 200 kW, 572 kW total at 1.59 kV.
1878	Automatic end of induction heating by failure of light guide CX4 in the north section of the crucible at -180 mm level. Thermocouples at the –150 mm and –170 mm level, however, do not yet show arrival of the melt front. But the light guide signal is judged to be reliable, as light guides cover a wider surface than the thermocouples. Intense boiling is continuing.
1880 → 2060	Boiling from the crust surface continues, especially W of the centre. Lights off in crucible shows totally dark surface.
2060 → 2160	2nd volcanic eruption of bright melt particles slightly east of centre of the surface over a period of 100 s until 2160 s, causing intense boiling. Argon cover gas flow through the porous concrete layer below the crucible is still cold, therefore no indication that the eroding melt penetrated into this layer. Water level at 2160 s is reduced by some 10 cm below the edge of the MgO ring probably by evaporation.
2230	2nd light guide CX 10 fails at the –180 mm level. Thermocouples in the –170 mm plane register 450°C maximum.

2300 → 2400	Slow boiling from the melt crust continues mainly in the centre. Light guide CX3 fails at the –180 mm level. Thermocouples register radial erosion through the steel layer of about 60 mm (BT 87 – 90 up to 1160°C).
2650 → 2930	Reactivation of spray flooding, as water level was reduced to some 150 mm below the upper edge of the MgO ring. Addition of cold water has no influence on TC measurements in the lower crucible: Continuation of slow temperature increase in the lowest level of the crucible. Main Ar cover gas flow reduced from 50 to 20 m3/h to avoid steam condensation and haze in the crucible that occurred before. Clear view to the water surface. End of spray at 2930 s as water level reaches upper edge of the MgO ring.
3000 → 3300	Thermocouple readings in plane –150 mm: 2 TCs failed, others show >1000°C. Plane –170 mm shows temperatures up to 700 °C. Temperature in the bottom porous layer 60°C. This layer is still flooded by Ar.
3300 → 4200	At 3300 s, start of flooding the porous concrete layer under the crucible with 0.6 litres water/s, without any energetic event. Flooding the bottom and sidewalls shall stabilize crucible and melt in accordance with the planning. Thermocouples at –170 mm level register onset of bottom cooling at 3430s. Weak boiling from the upper melt crust continues, resulting in small steam release through the off-gas line. Flooding of the bottom porous layer resumed and maintained after some interruption.
4240	End of experiment declared. Flooding maintained to stabilize the crucible and to extract energy from the solidified melt.
10000	In spite of permanent flooding, temperature at the lower steel/concrete interface still 1000°C. Water filled crucible allowed to cool down over 2 days.

After careful preparation of the test and check of all measurement and control systems, inertisation of the test rig by argon cover gas flow started 30 min before pour of the melt. The induction heating system was started at –150 s and operated under the nominated voltage. The mixed and pre-heated thermite powder was ignited in the external thermite vessel 90 s before pouring. After separation of the metal and the oxide phases, the major part of the melt (initial temperature 1665°C) was discharged into the concrete vessel, starting at time zero (Figure 12). Melt release to the concrete vessel was completed after 24 s, and the hood of the crucible was closed at 38 s, so that all gases from the crucible are forced through the off-gas line.

The initial phase of the dry melt concrete interaction was characterized by a vigorous interaction with high gas release which resulted in a hydrogen flame at the outlet of the off-gas tube, and a strongly agitated melt that splattered parts of the melt to the MgO liner (Figure 13). End of the hydrogen flame at 115 s indicates transition to a more moderate interaction, which after 220 s is characterized by a well agitated, bright melt. Some eruptions which probably develop at the melt concrete interface, transport dark material to the oxide melt surface that is dissolved subsequently (Figure 14). This material is either splashed concrete, or oxide melt crusts that detach from the concrete interface. Some more vigorous melt ejections may indicate accumulation of gases and molten concrete under a detaching crust (Figure 15).

In the early test phase, decay power to the melt is 10 to 15 % less than the planned 200 kW, limited by the low efficiency of coupling, while the bottom concrete layer is still thick. As downward erosion proceeds, better coupling allows heating with the planned 200 kW after 260 s. Thereafter, further increase of coupling is compensated for by reduction of the induction voltage. Downward melt progression is monitored by failure of the thermocouples in the bottom concrete layer, and reaches -60 mm at 540 s and ~ -90 mm at 800 s.

The video observation of the agitated oxide melt surface allows an estimate of the oxide viscosity. The viscosity of the oxide melt in the initial test phase until ~250 s is similar to glycerine (~ 1 Pa · s) in the early interaction phase until ~250 s. Then the viscosity, predominantly of the surface layer, increases by ~ 2 orders of magnitude until 350 s where a maximum is achieved. Further on, the viscosity is reduced, and is again similar to glycerine until start of surface flooding.

As the melt did reach the –90 mm concrete level, bottom flooding was started at 800 s by the shower in the crucible hood with 0.375 litres/s. The spray contacted the surface of the bright and well agitated oxide melt without any significant energetic interaction or eruption of melt. The melt surface appeared to be covered by a continuous water layer after ~10 s. Figure 16 shows the formation of a viscous surface layer under the water layer, and a small area with bright bulk material. 60 s after start of flooding parts of the surface became dark, which indicates onset of quenching the surface crust. Subsequently, 4 hot spots existed at 880 s. Some melt eruptions occurred which were driven by gas release from the concrete, but had little effect on crust formation, nor did they provoke strong melt-water interaction. At 940 s the melt was totally dark in that no hot spot nor volcanic eruptions were visible. The spotlight in the hood was switched on, and showed the intensively boiling water layer and the continuous spray from the shower. Evidently, a stable crust had formed on the surface of the melt, and no melt eruptions nor crust failure were visible. A large amount of steam was released through the off-gas tube.

Flooding was maintained until 1700 s when the spray was stopped as the water layer reached the upper edge of the MgO ring. Downward erosion had continued, as indicated by failure of further thermocouples and by increase of the heating efficiency, which was compensated by further reduction of the induction voltage. Figure 17 shows continuous boiling from the melt surface.

A first volcanic eruption of melt occurred at 1760 s over a period of 120 s through a hole that developed in the surface crust. Bright melt particles were ejected into the water layer (Figure 18). They caused intense boiling but no pressure spikes.

At 1878 s, automatic end of induction heating was generated through failure of one of the 4 light guides in the –180 mm level of the crucible. This ended the heating period of the test. At this time, thermocouples at the –150 mm and –170 mm level did not yet register arrival of the melt front.

A 2nd volcanic eruption of hot particles through the surface crust occurred at 2060 s over a period of 100 s and produced intense boiling. Later on, 2 further light guides in the bottom of the crucible were destroyed. To exclude any penetration of the concrete crucible, its bottom and outer sidewalls were flooded at 3300 s by flooding the porous concrete layer under the crucible. This occurred without problems and no indications for penetration of the crucible were found. At 4200 s, end of the test was declared. Registration of the temperatures as measured by the thermocouples continued over 6 hours and showed slow cool down of the solidifying melt (~ 500°C after 6 hours at the concrete interface). After 2 days, disassembly of the test rig was started.

In conclusion, the test was performed as planned and the important phases of dry MCCI and subsequent surface flooding could be realized so that good experimental data were obtained.

The following pictures illustrate important events during the test as seen by the video camera looking from the centre of the hood to the surface of the melt.

Figure 12: Pour of the oxide melt fraction at 11 s

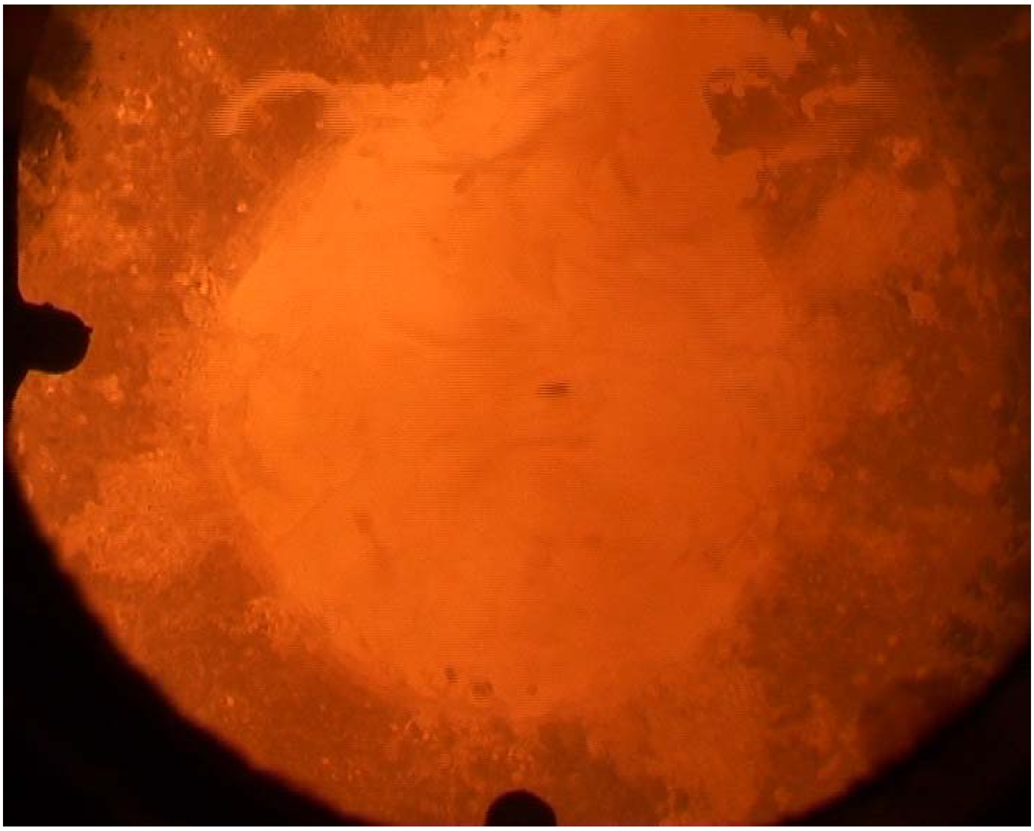

Figure 13: Intense melt concrete interaction with melt splashing at 115 s

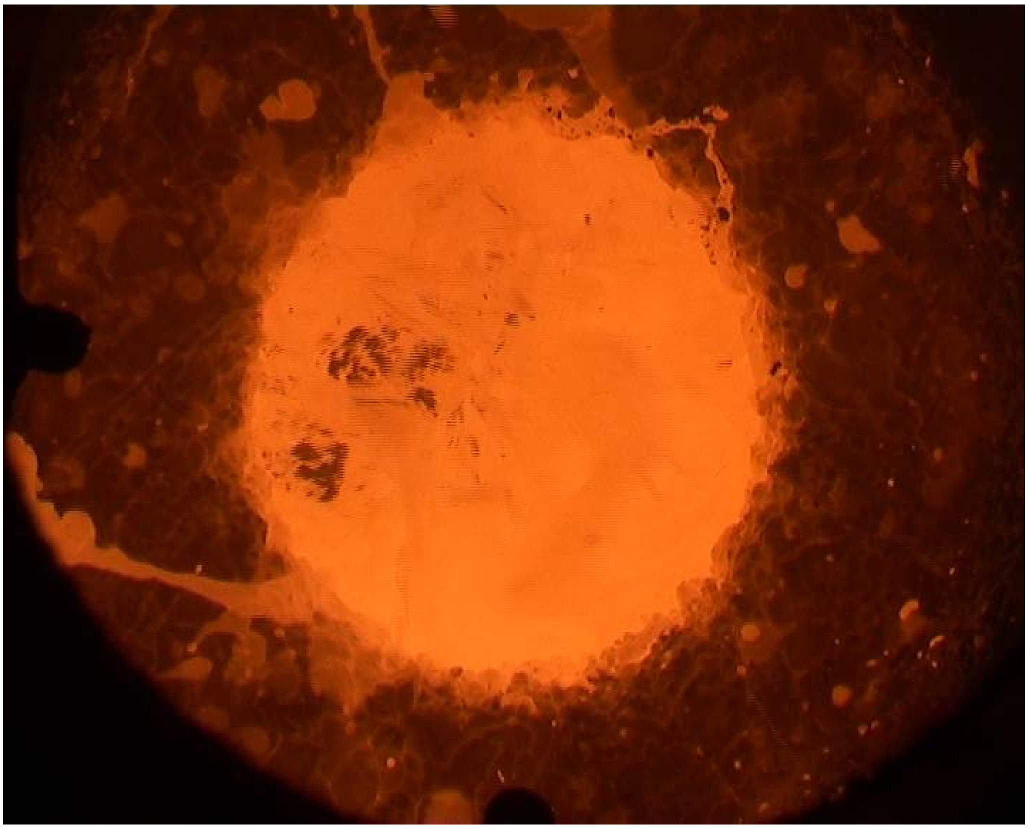

Figure 14: Steady erosion with dark oxide material expelled from below (240 s)

Figure 15: Eruption of melt upon removal of interfacial crust (290 s)

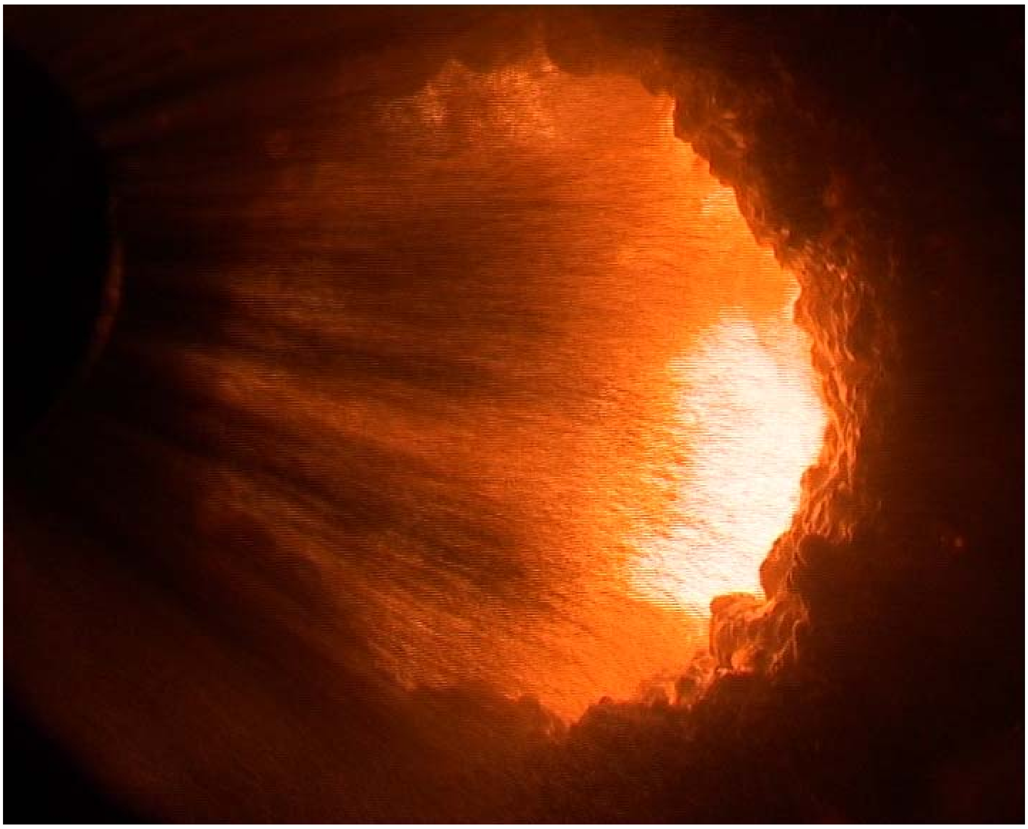

Figure 16: Flooding the melt surface by a showerhead (840 s). The melt forms a darker, viscous surface layer

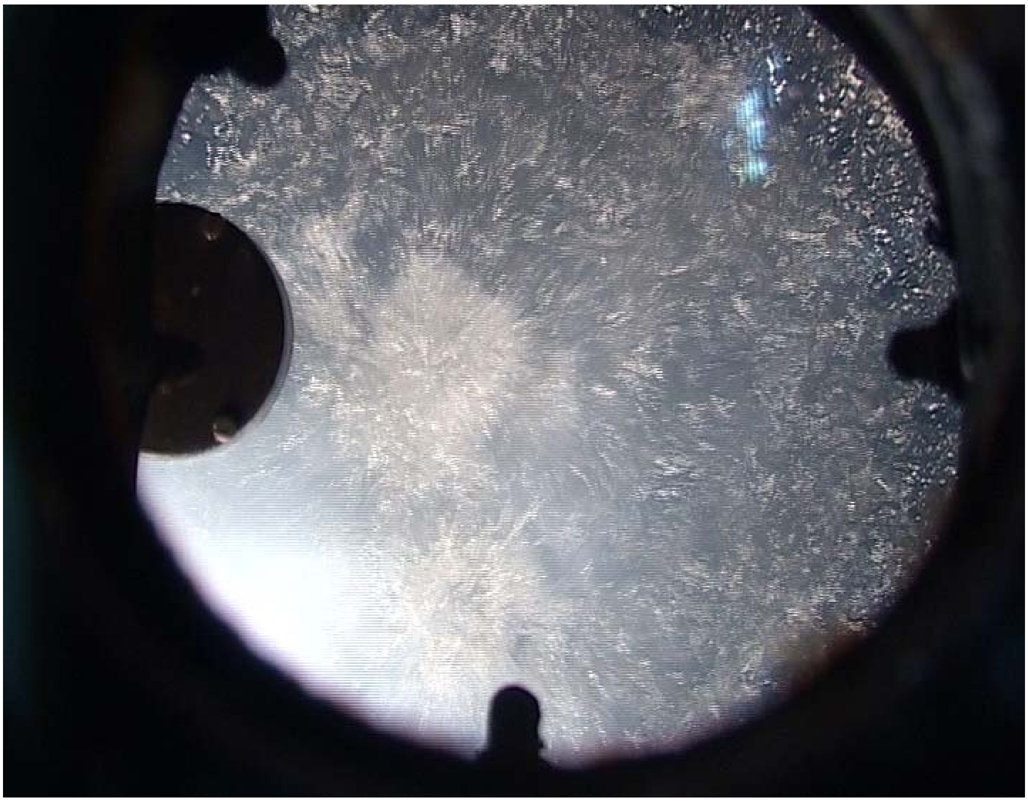

Figure 17: Continuous boiling of the flooded melt surface (1680 s)

Figure 18: Volcanic melt eruption through the flooded surface at 1760 s. Hot oxide particles are injected into the boiling water layer.

4 Experimental Results

4.1 Mass and temperature of the melt

As mentioned above, the mixed and pre-heated thermite powder was ignited in the external thermite vessel 90 seconds before pouring. Figure 19 gives the weight of the thermite vessel during thermite burn and melt release. The thermite reaction was completed after 60 seconds. After further 30 s to allow separation of the metal and oxide phases, the major part of the melt was discharged into the concrete vessel starting at time 0 s. Melt release to the concrete vessel was completed after 24 s, at which time the residual melt was directed into the slag wagon. Figure 19 shows a sharp transition during the pour at 12 s which indicates the transition from release of steel to oxide. Evaluation of this plot yields a total melt mass of 636 kg that was released to the crucible from time 0 to 24 s. This pour consisted of 425 kg steel and 211 kg oxide with slight deviations from the planned masses.

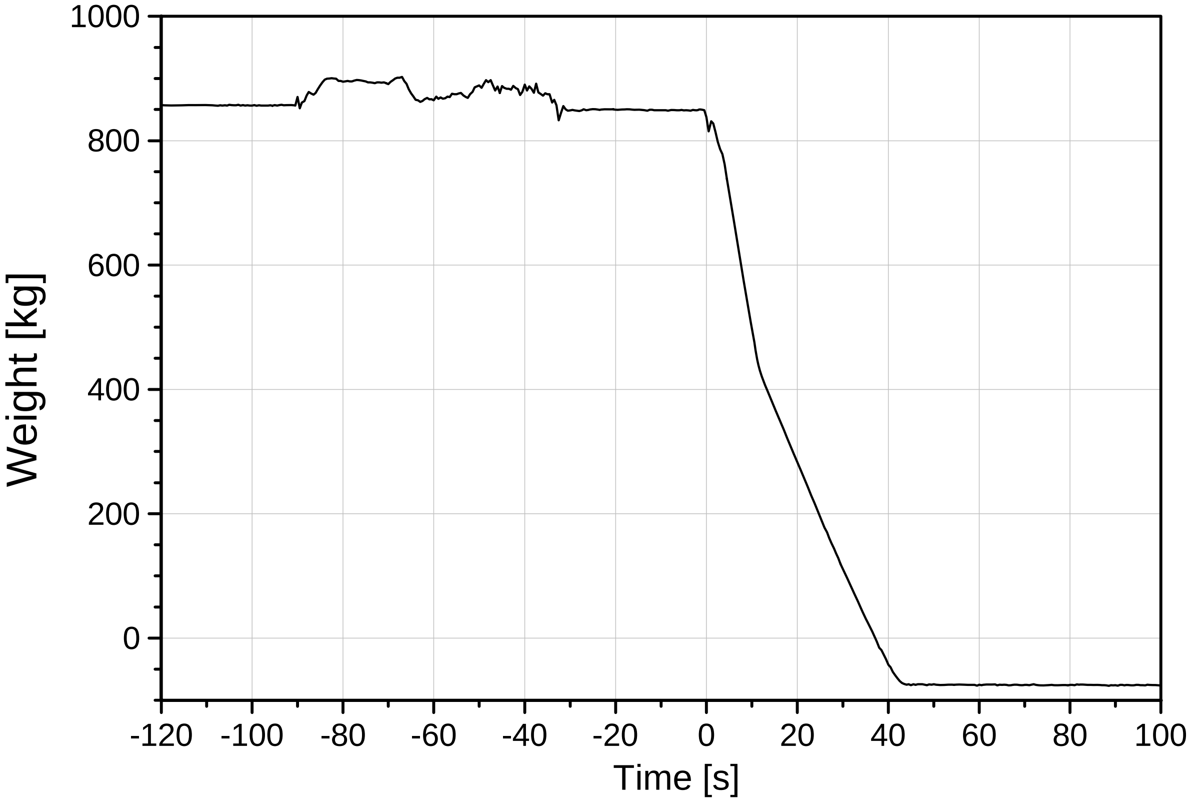

Figure 19: Weight of thermite vessel during thermite reaction and melt release

The initial temperature of the melt as measured in the spout by a W-Re thermocouple for the released steel phase at 10 s, was 1664°C (see Figure 20). The oxide temperature is assumed to be identical, however the thermocouple response is less reliable – as also found in the previous tests. The declining curve after 25 s shows cool down of the spout after end of pouring.

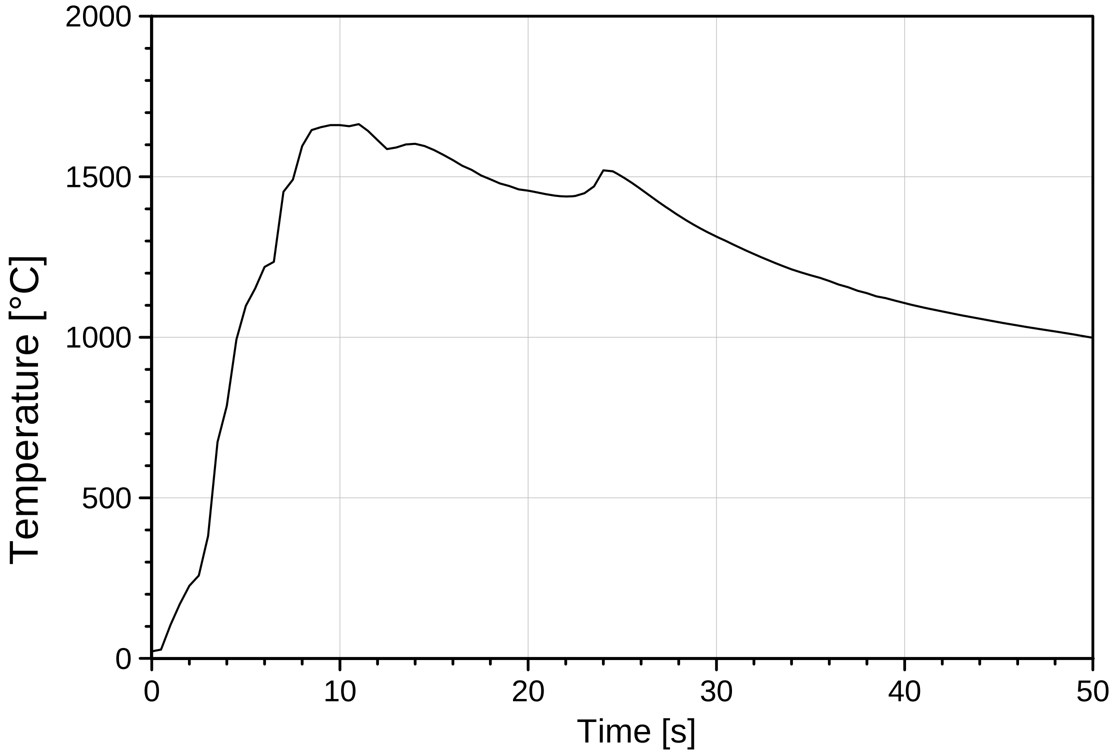

Figure 20: Melt temperature in the spout

An infrared video camera was installed on top of the hood of the crucible at a distance of ~2.5 m from the melt surface. This camera operates in the near infrared spectrum from 3.4 to 5.0 μm to produce a video film and, every 15 s, up to 240 high precision thermal images of the melt surface during 60 min. The camera utilizes a 3.9 micron flame suppression filter and is placed behind a 3 mm thick sapphire window which has a transmission coefficient of ~0.9 at the considered wavelength.

Two thermal images during pour of the iron and oxide melt stream, respectively, have been taken to measure the initial temperature of the melt and to check the emissivities that were determined in the COMET-L1 and -L2 experiments. These thermal images, corresponding visual pictures from a standard video camera, and temperature histograms of the melt pouring process in the COMET-L3 test are shown in Figure 21. The used emissivities are 0.3 for the metal phase and 0.92 for the oxide phase.

Thermographic analysis of the metal pour (left figure) shows that the estimated temperatures of the melt stream are within a range of 1600-1850°C with a distinct maximum at 1650-1700°C. These estimates are in fairly good agreement with the 1664°C measured by a W/Re thermocouple in the spout (compare Figure 20). The brighter areas in the thermograms are due the oxide film on the surface of the iron melt pool, that forms immediately upon onset of the concrete erosion and has a higher emissivity.

The IR-measured temperature of the oxide film is about 100°C below the thermocouple measurement. This is probably due to the presence of aerosols that develop in the crucible and that absorb part of the radiation.

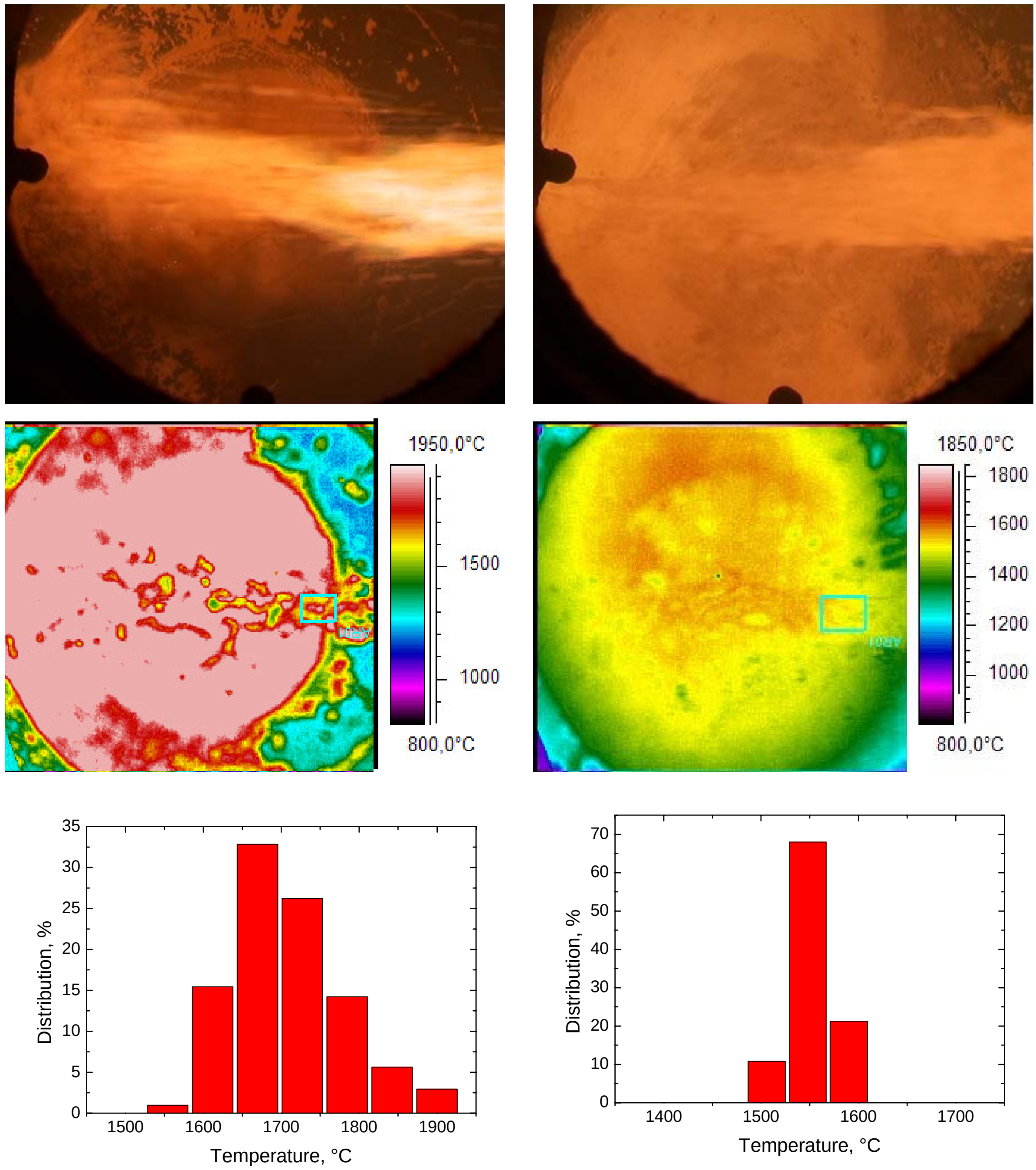

Figure 21: Temperature of the metallic melt jet (left) and of the oxidic melt jet (right).

The upper video picture corresponds to the infrared picture in the middle. Temperature histograms from the melt jet are plotted below.

Figure 22 gives the surface temperature of the oxide melt as measured by the IR camera during the further course of the test. The emissivity of the oxide is assumed as 0.92, in agreement with the evaluation in Figure 21. Two curves are evaluated: The red, upper one gives the maximum temperature registered on the surface, the blue, lower gives the minimum temperature. Both registrations end at 800 s with onset of flooding: Coolant water and steam absorb the IR radiation from the melt surface and therefore useful data are restricted from 0 to 800 s. During this period the melt is strongly agitated and no surface crust exists. Fresh material from the bulk of the oxide melt is transported to some fluctuating sections of the surface, and consequently, the red temperature is a good representation of the oxide bulk temperature. On the other side thermal radiation cools down other parts of the surface layer, represented by the blue line, which is 100 to 200°C below the bulk temperature. Nevertheless, the blue curve represents a temperature that is above the solidus temperature of the oxide melt as no crust is growing on the melt surface during this period of the test.

The red curve clearly shows the fast decrease of the temperature of the oxide melt during the first 100 s from 1665°C to ~1350°C, and a slower temperature drop to ~1000°C until 800 s. These temperatures are in the expected freezing range of the oxide melt, that changes its composition by the ongoing admixture predominantly of silica from the decomposing concrete. It is evident, that these low temperatures exclude major erosion of the concrete cavity by the oxide melt, as confirmed by the erosion data.

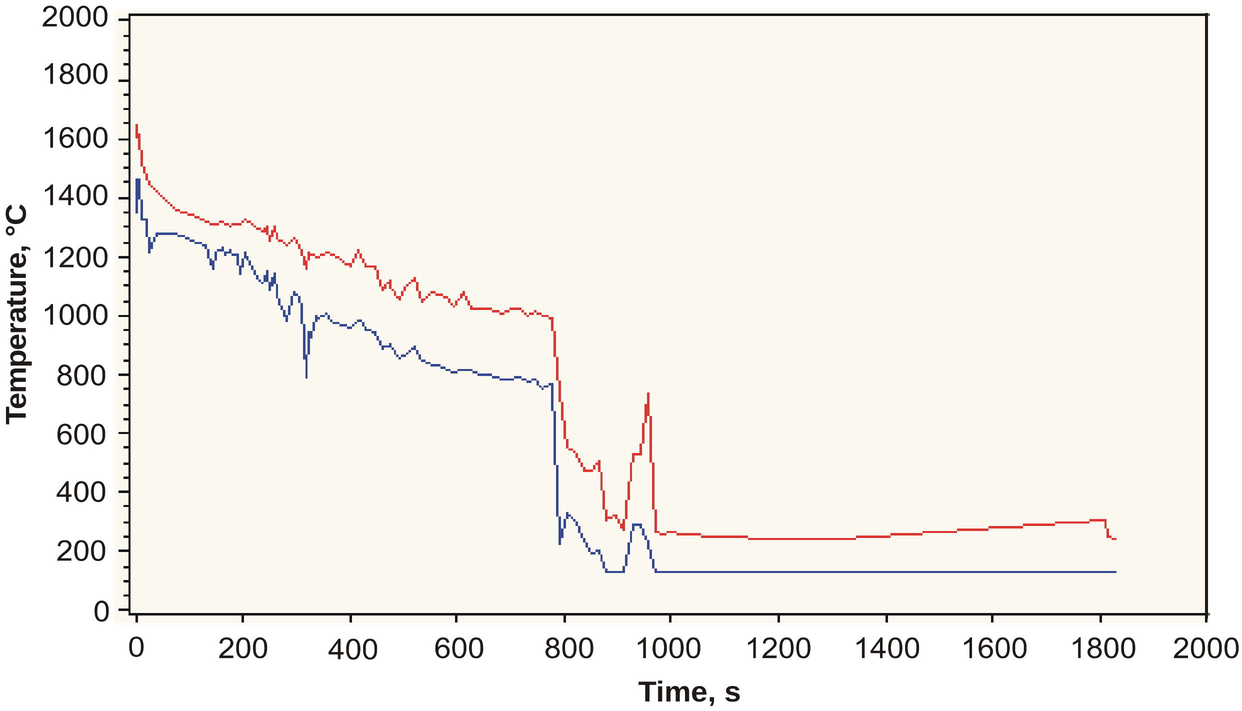

Figure 22: IR measured temperatures of the melt surface assuming the oxide emissivity of 0.92

4.2 Decay heat simulation and melt behaviour

Operation of the induction system to simulate the internal decay heat in the melt was started some 2 minutes before the melt was poured into the crucible. The voltage of the induction coil was controlled by the operator throughout the heating period, to achieve and maintain the net power input to the melt of 200 kW according to the test plan. Online measurements of the net power and of the total power gave the necessary information to the operator. We repeat that the induction heat is deposited in the metal phase at the bottom only.

Figure 23 to Figure 25 show the characteristics of decay heat simulation. Besides the important information on induction voltage and power input, the efficiency of heating and the power fluctuations allow some estimates on the status of the steel melt, as the geometry of the metal influences the electromagnetic coupling to the induction field.

The voltage for the induction coil was at its constant maximum value of 2600 V from –20 s to 500 s. Later on, the voltage is reduced step by step down to 1600 V (Figure 23), because the heating efficiency (Figure 25) improves as the melt comes closer to the induction coil with ongoing downward erosion. Fluctuations of net power and of the efficiency during the first 500 s are therefore directly related to a change of the geometry of the metal layer. The vigorous gas release during the initial test phase generates substantial oscillations of the power / efficiency. Some of the stronger melt ejections correlate with a short increase of the net power/efficiency, as the effective metal surface may be increased for a short time period.

In the long term, melt progression results in a clear increase of the efficiency from 0.15 to 35 %, in agreement with the preceding COMET-L2 experiment [8]. This is best seen in Figure 25, as the efficiency plot is independent of the actual induction voltage.

Flooding the melt surface with coolant water at 800 s has two important consequences:

- The increase of efficiency with time slows down considerably, as compared with the earlier period and with COMET-L2. This is probably related to a slower downward concrete erosion.
- There is a significant reduction of power fluctuations for the subsequent time period. Only during the period of crust formation, some eruptions between 880 and 925 s still occur, that eject some melt and generate some positive and negative power fluctuations. Thereafter, the existence of the crust after 950 s reduces the agitation of the melt pool and thus stabilizes the geometry of the steel layer. It is remarkable that the 1st volcanic eruption, that occurred between 1700 and 1870 s has no influence on the heating efficiency. This indicates that in this eruption only oxide melt was involved. Indeed, the ejected granulate that was found after the test, is totally oxidic.

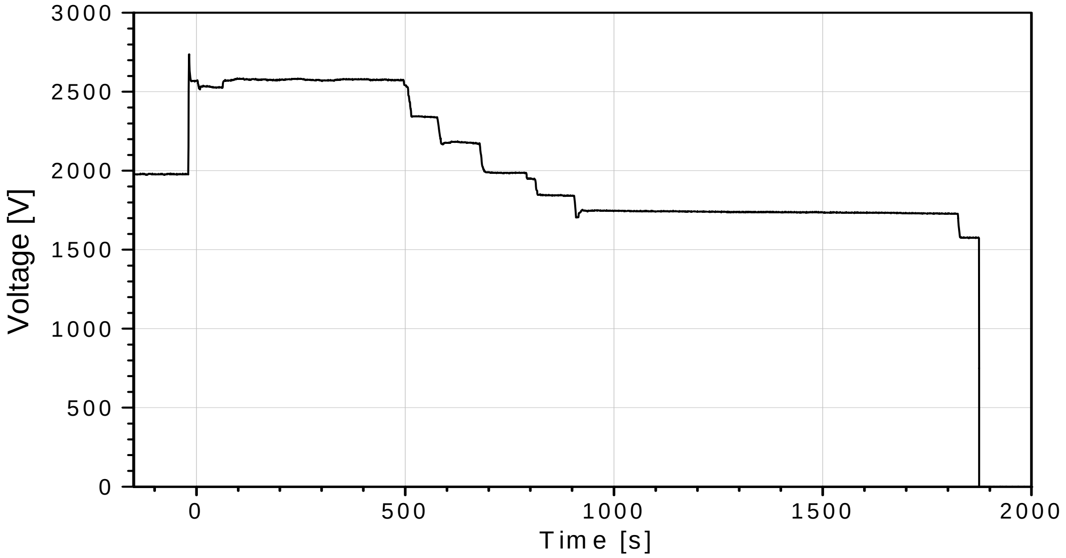

Figure 23: Voltage to operate the induction coil

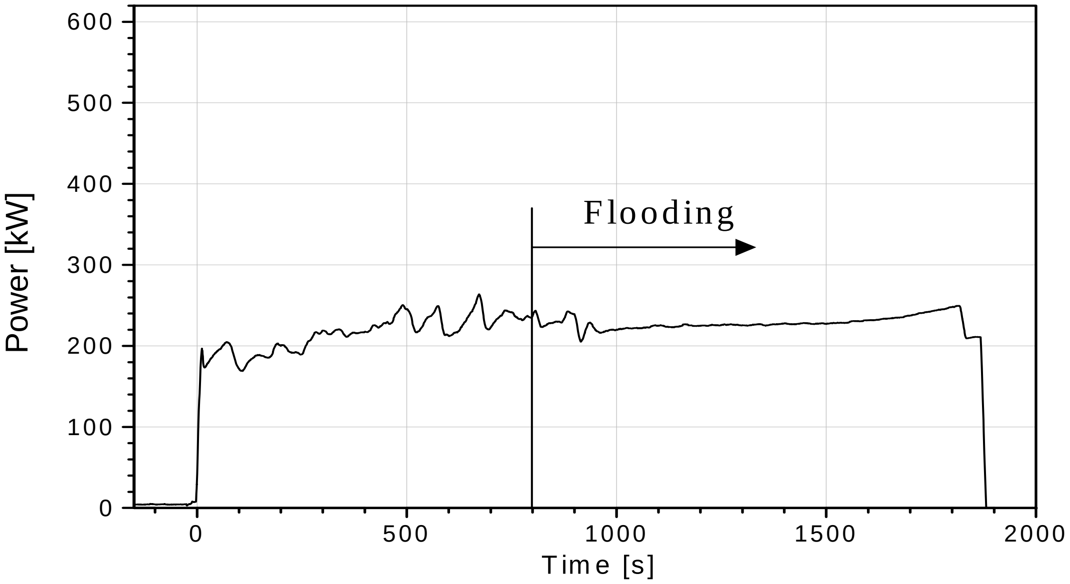

Figure 24: Net heating power in the melt by induction

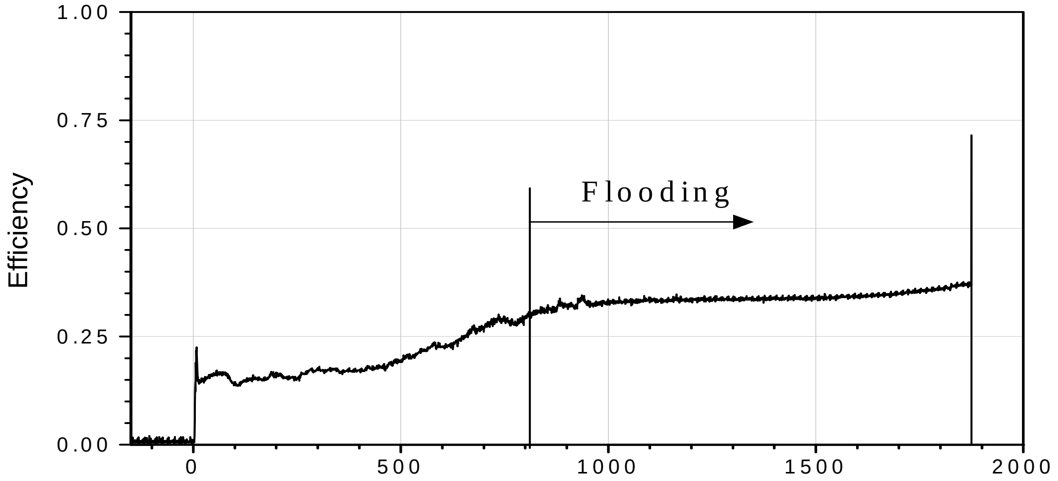

Figure 25: Efficiency of the induction heating, referred to the gross heating power

4.3 Concrete erosion and cavity shape

For a detailed analysis of concrete erosion rates and cavity shape, the failure times of thermocouples in the concrete cavity are evaluated. This information together with notation and position of the thermocouples are given in Table 10. As an exception, BT 87 – 89 show a “slow” failure, in that a slow temperature rise is registered but no clear failure. However, the thermocouples register temperatures after 2000 s that exceed their measurement range. Therefore, new junctions have probably formed. The melt may have reached these thermocouples between 1500 and 2000 s. Their failure times are however taken to be close to 1900 s.

The measurements of all thermocouples that are located in the concrete crucible are given in Appendix C, Figure C- 1 to Figure C- 33. They are grouped in accordance with the instrumentation lines T1 – T9 that are introduced in Figure 26.

Figure 26 gives the recorded failure times in a scaled drawing of the concrete crucible in the 2 instrumentation planes SW-NE and SE-NW, respectively. For each position, the name of the thermocouple and its failure time are given. As an example, 16/1040 s means: Thermocouple BT16 fails at 1040 s. For thermocouples which did not fail, the time information is replaced by “-“. In addition, arrows with a notation such as “T2|SW” are placed in the initial cavity area. These arrows define instrumentation lines, that is a series of 1 to 6 thermocouples along one line either in the lateral or axial direction, for which an erosion versus time plot is generated further below. The extensions SW, NE, SE, and NW define the particular section of the crucible with symmetric thermocouple positions. CL is the group of thermocouples on the vertical centre line of the crucible.

Figure 27 to Figure 30 give the plotted erosion fronts in the crucible vs. time as defined by failure of the thermocouples along the instrumentation lines T1 through T9. For the crucible planes SW-NE and SE-NW, a similar erosion history is observed with minor deviations from symmetric behaviour. The upper plots represent erosion in the bottom of the crucible into the downward (axial) direction (T1-T3). The lower plots give the lateral erosion into the cylindrical wall (T5 – T9).

Table 10: Position and failure times of thermocouples in the concrete cavity

Plane SW-NE				**Plane SE-NW**			
Name	**Radius,mm**	**Height, mm**	**Failure, s**	**Name**	**Radius,mm**	**Height,mm**	**Failure, s**
BT01	0	-30	113	BT01	0	-30	113
BT02	140	-30	116	BT03	140	-30	117
BT04	-140	-30	237	BT05	-140	-30	255
BT06	250	-30	310	BT07	250	-30	243
BT08	-250	-30	323	BT09	-250	-30	270
BT10	310	-30	1580	BT11	310	-30	1514
BT12	-310	-30	1413	BT13	-310	-30	1350
BT14	350	-30	-	BT16	0	-60	1040
BT15	-350	-30	-	BT18	140	-60	454
BT16	0	-60	1040	BT20	-140	-60	474
BT17	140	-60	346	BT22	250	-60	645
BT19	-140	-60	462	BT24	-250	-60	518
BT21	250	-60	775	BT25	0	-90	1811
BT23	-250	-60	557	BT27	140	-90	731
BT25	0	-90	1811	BT29	-140	-90	686
BT26	140	-90	737	BT31	250	-90	797
BT28	-140	-90	768	BT33	-250	-90	1365
BT30	250	-90	1245	BT35	310	-90	-
BT32	-250	-90	1435	BT37	-310	-90	-
BT34	310	-90	-	BT38	0	-120	2123
BT36	-310	-90	-	BT40	140	-120	1023
BT38	0	-120	2123	BT42	-140	-120	1437
BT39	140	-120	1023	BT44	250	-120	1448
BT41	-140	-120	1253	BT46	-250	-120	-
BT43	250	-120	1448	BT47	0	-150	-
BT45	-250	-120	-	BT49	140	-150	-
BT47	0	-150	-	BT51	-140	-150	-
BT48	140	-150	-	BT53	250	-150	-
BT50	-140	-150	-	BT55	-250	-150	-
BT52	250	-150	-	BT56	0	-170	-
BT54	-250	-150	-	BT58	140	-170	-
BT56	0	-170	-	BT60	-140	-170	-
BT57	140	-170	-	BT62	250	-170	-
BT59	-140	-170	-	BT64	-250	-170	-
BT61	250	-170	-	BT68	310	290	24
BT63	-250	-170	-	BT70	-310	290	90
BT65	310	350	291	BT76	310	90	18
BT66	-310	350	86	BT78	-310	90	20
BT67	310	290	189	BT82	310	15	100
BT69	-310	290	255	BT84	-310	15	187
BT71	310	190	27	BT88$^{*)}$	360	15	~1874
BT72	-310	190	17	BT90$^{*)}$	-360	15	~1963
BT73	330	190	292				
BT74	-330	190	234				
BT75	310	90	20				
BT77	-310	90	30				
BT79	330	90	116				
BT80	-330	90	125				
BT81	310	15	170				
BT83	-310	15	25				
BT85	330	15	1101				
BT86	-330	15	745				
BT87$^{*)}$	360	15	~1876				
BT89$^{*)}$	-360	15	~1875				

*) Thermocouples failed by “slow” attack, new junctions give too high temperatures

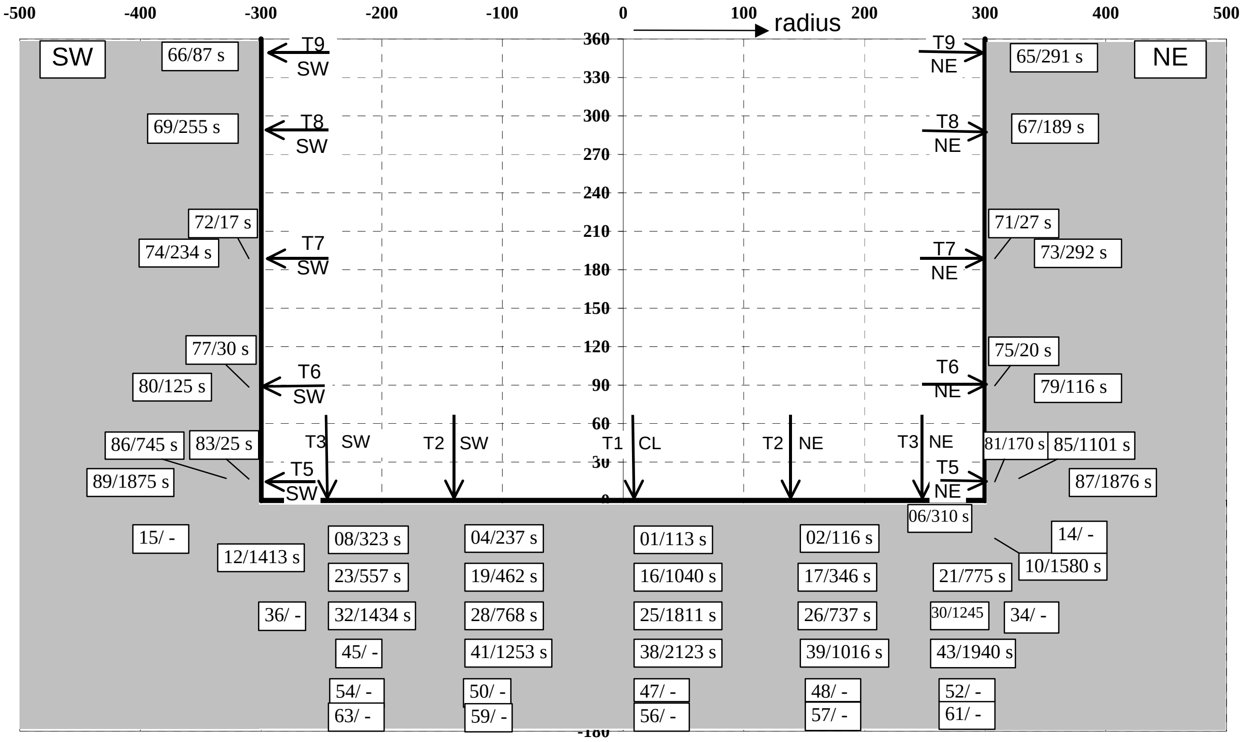

a) Plane SE-NW

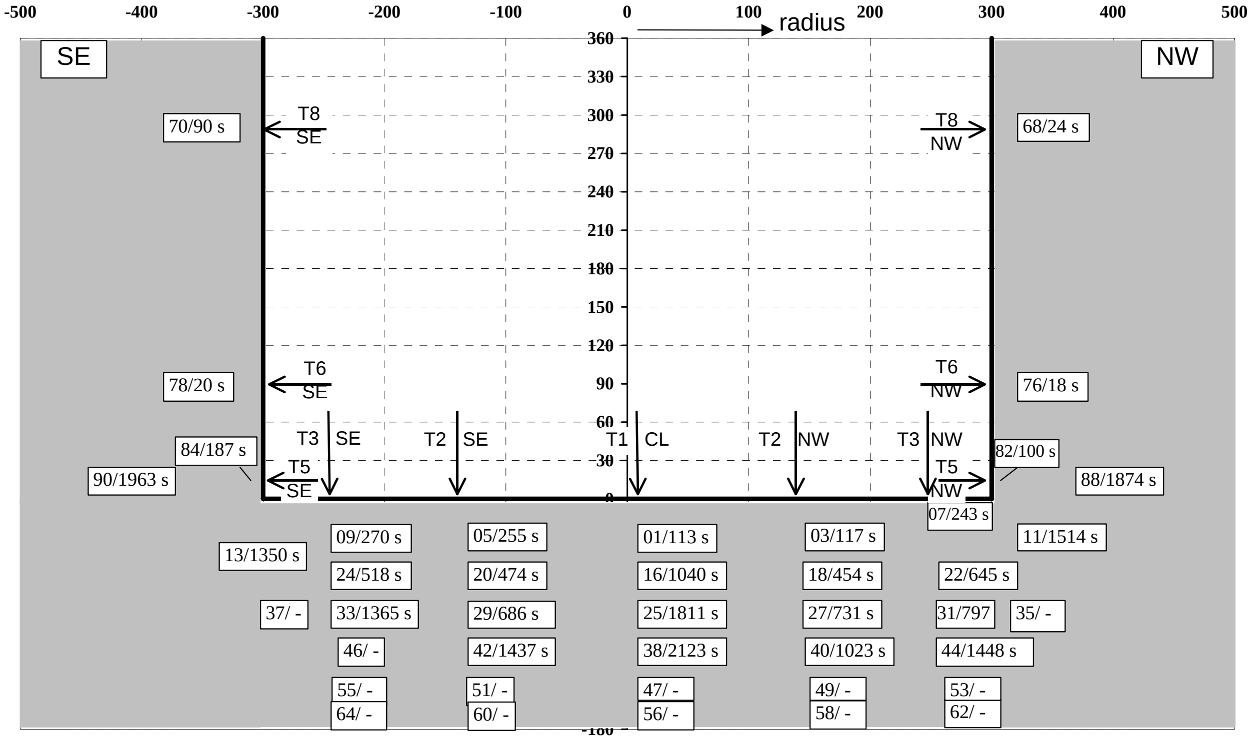

b) Plane SW-NE

Figure 26: Failure times of thermocouples in the concrete crucible through erosion of the heated melt. a) Plane SW-NE b) Plane SE-NW

The subsequent Figure 31 and Figure 32 give the end state of the eroded cavity as defined by the failed thermocouples. The dotted line, that is generated by a slight extrapolation of the thermocouple signals nearby, is close to the final cavity shape that became available after sectioning of the crucible, see chapter 4.6 on “Post Test Analyses”. These figures are useful to understand the erosion history:

The time resolved erosion histories in Figure 27 to Figure 30 show a fast axial and lateral erosion in the early test period for about 100 s. Initial erosion rates in those areas of the cavity that are contacted by the steel melt are same 0.15 mm/s into axial and lateral direction, but last not more than 100 s or 30 mm into the axial direction. The peak axial rates are found near the centre (Lines T1 and T2) with 0.3 mm/s. This high erosion evidently slows down as the overheat of the melt is reduced as indicated by the IR temperature plot in Figure 22. The average stationary erosion rate into axial direction until 800 s is 0.07 mm/s ±0.03 mm/s.

The erosion by the oxide melt in the upper part of the cylindrical crucible ends very soon as the oxide cools down beyond the “melting temperature” of the siliceous concrete. In the lower cylindrical regions that are contacted by the steel melt, erosion continues, however strongly reduced, and do not exceed some 60 mm until end of heating.

The axial erosion continues during the further course of the test. Addition of water to the melt surface at 800 s does not stop the melt until end of heating at 1880 s. The thermocouple signals alone, however, do not allow to detect a clear influence of surface flooding on erosion, partly because of their limited special resolution. There is, however, a reduction of downward erosion rate , that becomes more clear as the data from the sectioned cavity are applied (see chapter 4.7 using post test data). For the period after surface flooding downward erosion is further reduced to about 0.04 mm/s as is derived from Figure 57 and Figure 58.

The maximum downward erosion that was detected by clear failure thermocouples is 120 mm only. The light guides that switched off the simulated decay power, were located at the –190 mm plane. 3 out of 4 light guides were interrupted. They fail at lower temperatures (~400°C) than the Type K thermocouples (< 1300°C), and because of their wider spreading in the –190 mm instrumentation plane, detect irregular propagation of the melt front. Therefore, their response is ahead of the thermocouples. The sectioned crucible shows the maximum propagation of the steel melt at 175 mm. This information is discussed in chapter 4.7, Figure 53 and Figure 54.

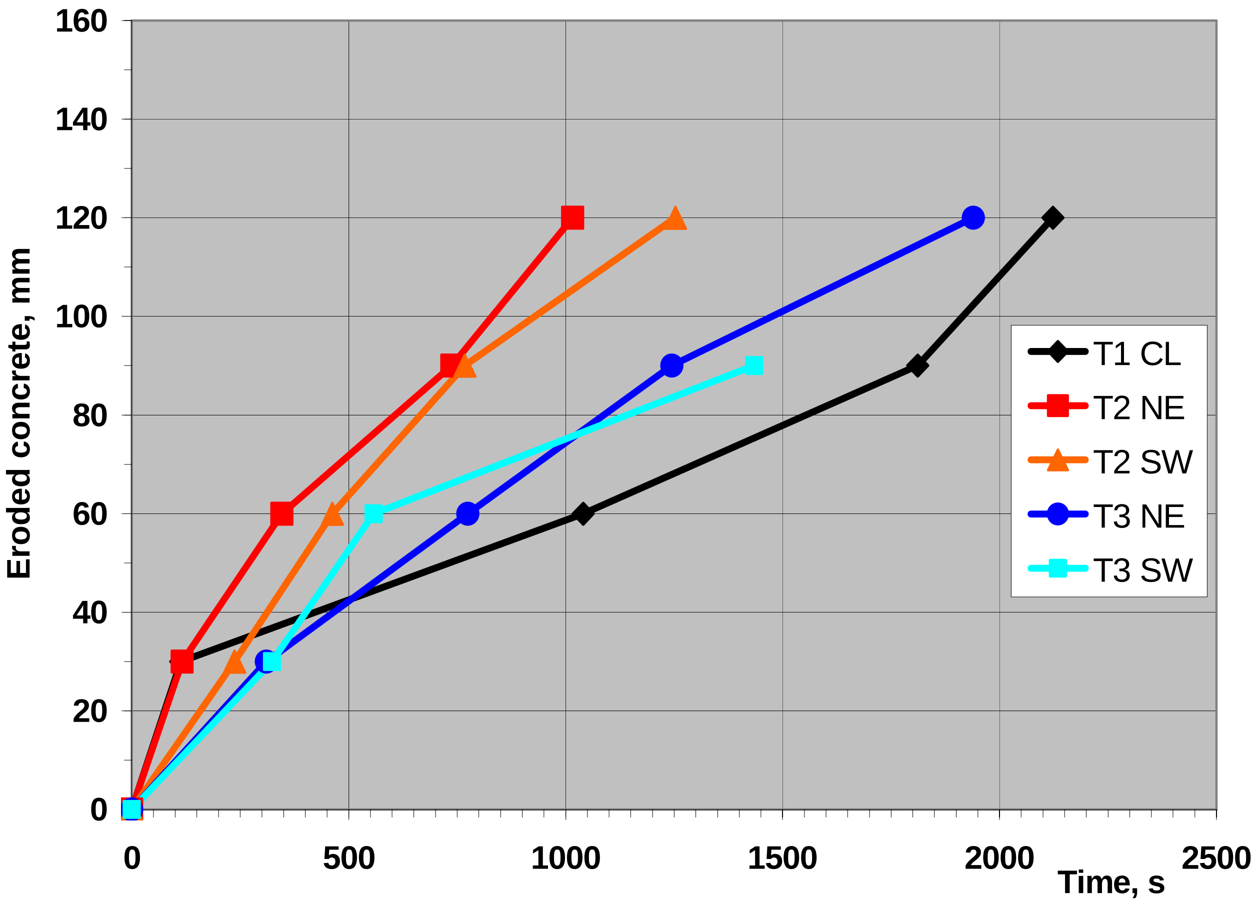

Figure 27: Axial erosion front of propagating melt in plane SW-NE of the concrete cavity

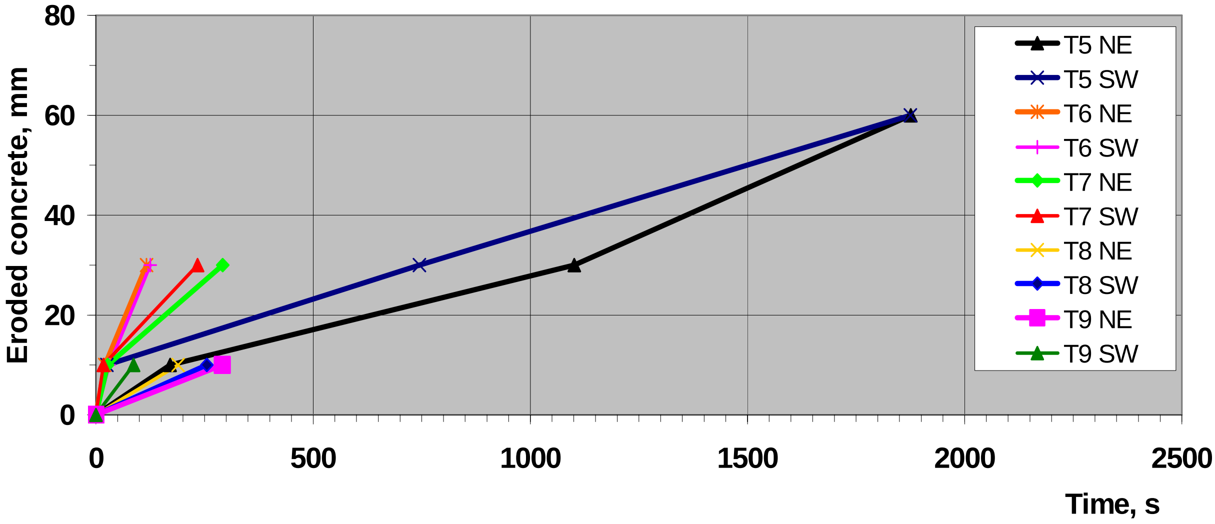

Figure 28: Lateral erosion front of propagating melt in plane SW-NE of the concrete cavity

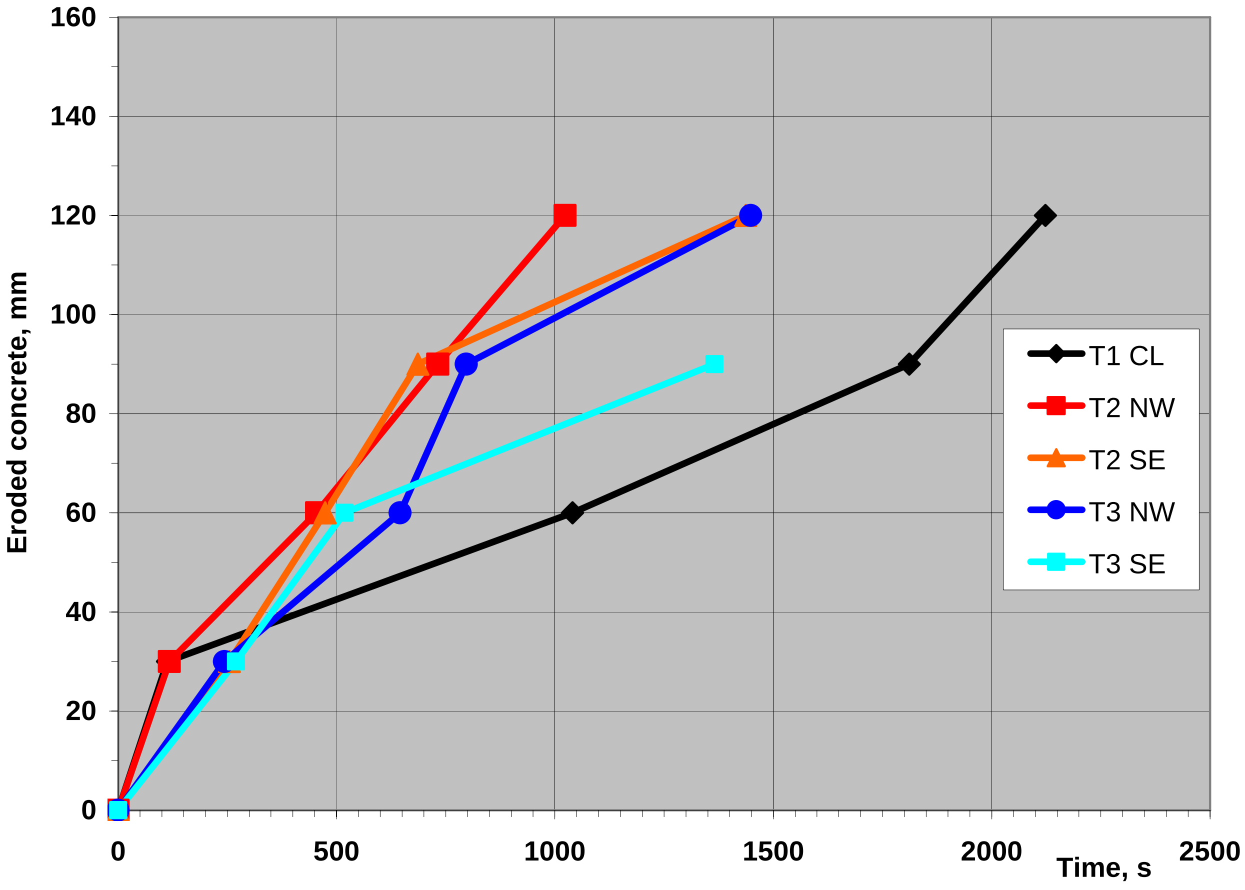

Figure 29: Axial erosion front of propagating melt in plane SE-NW of the concrete cavity

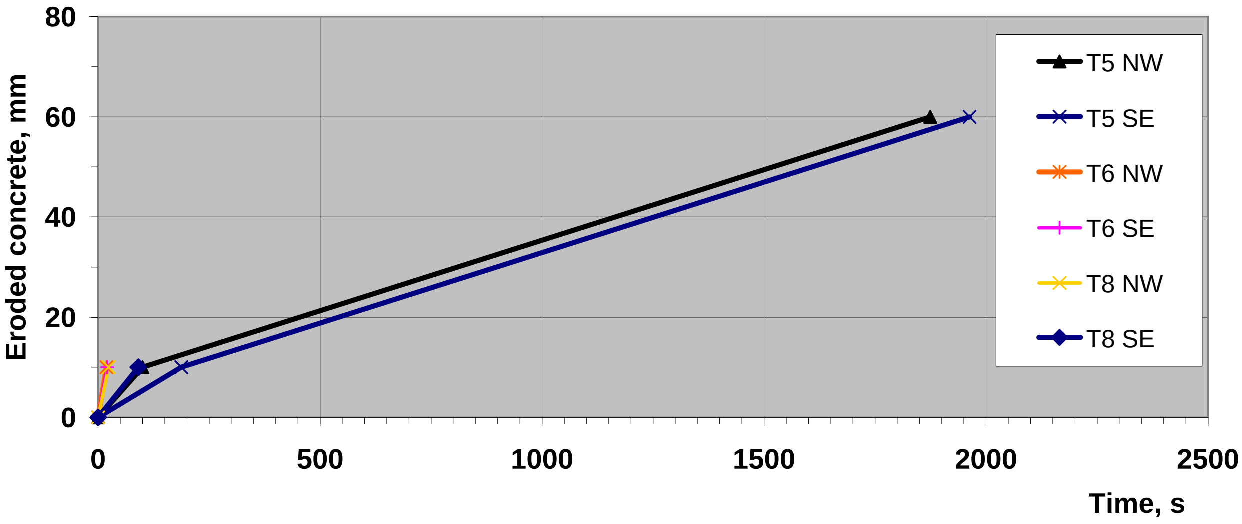

Figure 30: Lateral erosion front of propagating melt in plane SE-NW of the concrete cavity

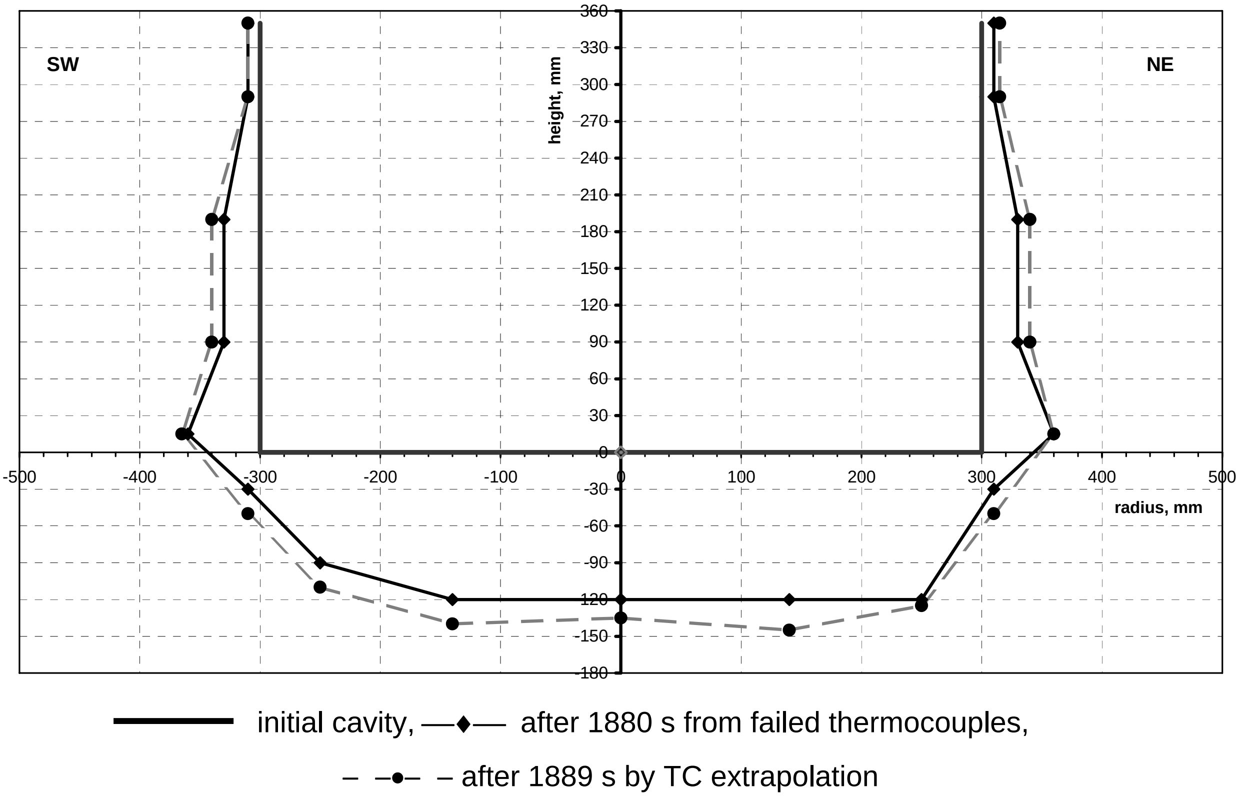

Figure 31: Eroded concrete cavity in plane SW-NE from TC measurements

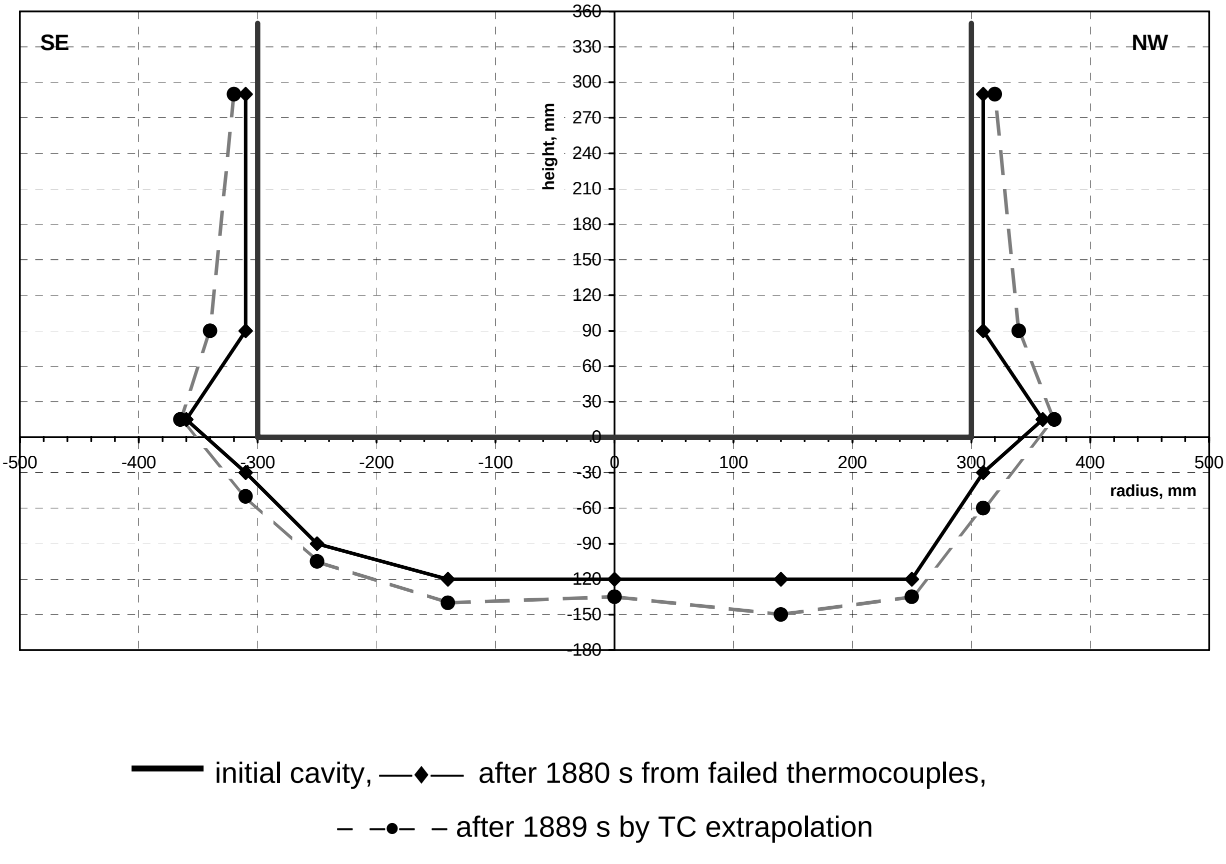

Figure 32: Eroded concrete cavity in plane SE-NW from TC measurements

4.4 Gas release

The gases that are released during MCCI and subsequent flooding are measured in the hood of the crucible and in the off-gas line that connects the crucible with the open atmosphere.

The gas pressure in the hood is given in Figure 33. The pressure remains constant at the ambient pressure throughout the test. No pressure spike did occur during flooding, as flooding was mild and did not produce energetic interactions.

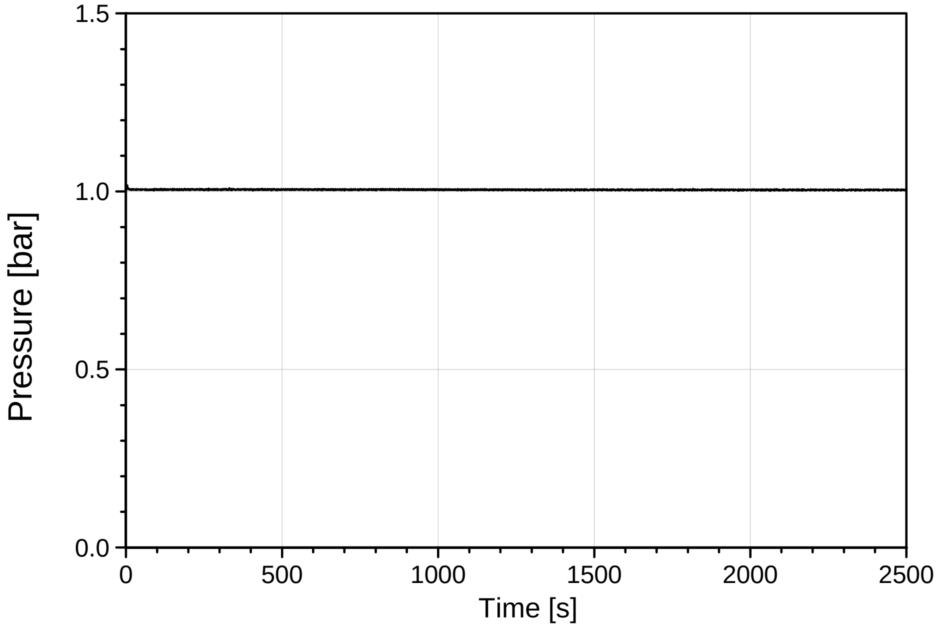

Figure 33: Gas pressure in the hood of the concrete crucible

The gas temperature in the hood is given in Figure 34. This temperature is a result of hot gas release from the melt surface, admixture of the cold argon cover gas, and heat transfer to the ceramic liner of the test section. During dry MCCI, the gas temperature falls from 300 to 240°C. With start of surface flooding by water spray, the temperature reduces to about 100°C.

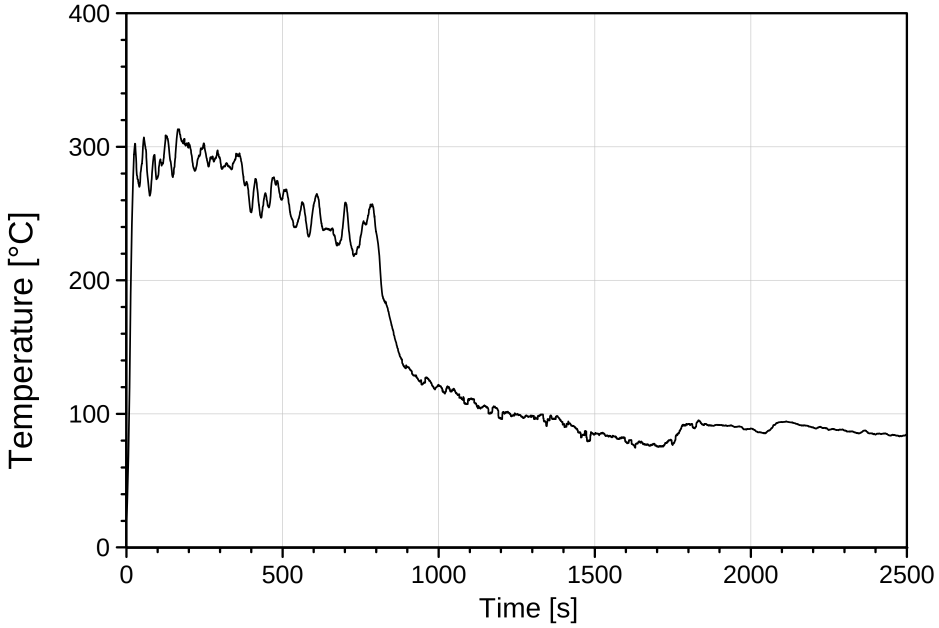

Figure 34. Gas temperature in the hood of the concrete crucible

Gas measurements to determine flow rate and gas composition were performed in the off-gas line, that was preheated to some 110°C to prevent steam condensation. However, measurement of the total gas flow rate was only partly successful. The Prandtl-tube that was positioned in the tube throughout the test gave reasonable results for the gas flow only from start of concrete erosion until start of surface flooding as shown in Figure 35.

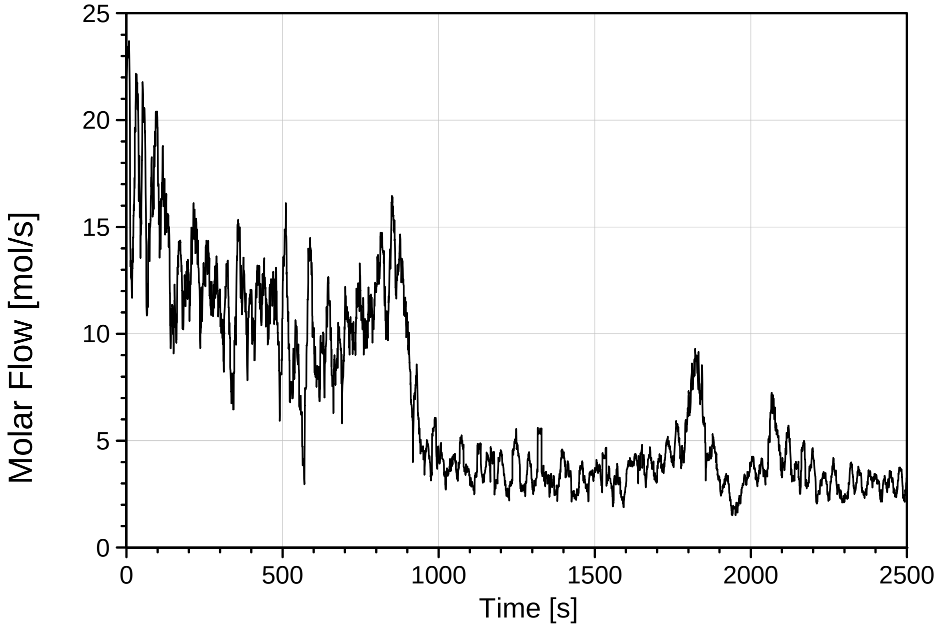

Figure 35: Approximate gas flow in the off-gas tube measured by the Prandtl tube

Registration is incorrect after onset of flooding at 800 s

Because of the very low dynamic pressure, the measurement signal was disturbed by noise, but could be restored by smoothing. The evaluated molar flow rate is, however, only tentative, as the specific composition of the gases is not taken into account for the evaluation. We see the typical tendency of the gas flow rate, namely higher gas release in the first 100 s and reduced, nearly stationary flow rate until onset of flooding at 800 s.

The interesting phase of steam release at flooding and thereafter, however, could not be detected. We believe that with activation of the spray water droplets were transported into the off-gas line and eventually blocked the fine holes in the Prandtl tube, so that the signal dropped to nearly zero. These droplets may also have prevented operation of the turbine flow-meter that gave no results at all. The consequence is that no gas measurements are available that allow direct quantification of steam release from the flooded surface of the melt.

The concentrations of H_2, CH_4, CO, and CO_2 in the off-gas were measured by the online mass spectrometer. This analysis was performed by G. Schumacher [10] and is plotted in Figure 36 and Figure 37. The flow rates of these gases are determined using the known argon cover gas flow that was kept constant during the test. The gas rates are referred to standard conditions, that is to 0°C and 1 bar pressure (22.4 litre/s correspond to 1 mol/s). The steam content could not be measured, as it had to be separated from the sample gas flow by condensation to protect the mass spectrometer. It must be noted that the spectrometer has a slow response time of some 30 s which does not allow detection of fast events. As gas release is coupled to the erosion rate, its time behaviour indicates the concrete erosion.

Figure 36 shows the dominant role of hydrogen during dry MCCI. Water vapour that is released from the decomposing concrete is reduced to hydrogen as penetrating through the metal melt. For the actual metal composition this results in formation of iron oxides, whereas Ni oxidation is not expected. Similarly, CO is reduced from CO_2, and results from carbonates which are present in small quantities in the concrete Both reactions are under present conditions not complete. Before flooding at 800 s, the CO:CO_2 ratio is of the order 2:1, with an exception between 200 and 600 s. A similar ratio may be assumed for the ratio H_2:H_2O during that period of the test. Very little methane is released. As typical for siliceous concrete, CO release is significantly smaller than H_2 release. It is expected to be of the order of 1/10 of the H_2 release as measured e.g. in COMET-L1 [7]. The significantly higher CO content after 500 s is at present unclear.

The pronounced initial gas peak is a consequence of the initial overheat of the melt and the fast concrete erosion. H_2 release slows down after 200 s as the melt cools down, reaching a nearly constant release rate until onset of surface flooding at 800 s. Referring also to the release of CO and CO_2, surface flooding reduces release of the measured gases from concrete in the actual test. This is probably due to a reduction of concrete erosion by the metal melt, and is probably in line with formation of a stable metal crust at the concrete interface, that is derived from the stop of oscillations in the net power history (Figure 24) and in the heating efficiency (Figure 25). Furthermore, a metal crust would reduce the reaction rates of H_2O and CO_2 with the metal layer, as is confirmed by the reduced CO:CO_2 ratio. For a further discussion of the consequences of flooding see section 4.5.

Further reduction of gas release occurs after end of heating at 1880 s. Ongoing heat up of the concrete because of slow cool down of the melt is the reason for the slow decay of the measured H_2 rates.

Figure 37 provides the integrated gas release as determined by integration of the data given in Figure 36. During the heating period of the test approximately 7000 l of hydrogen were released.

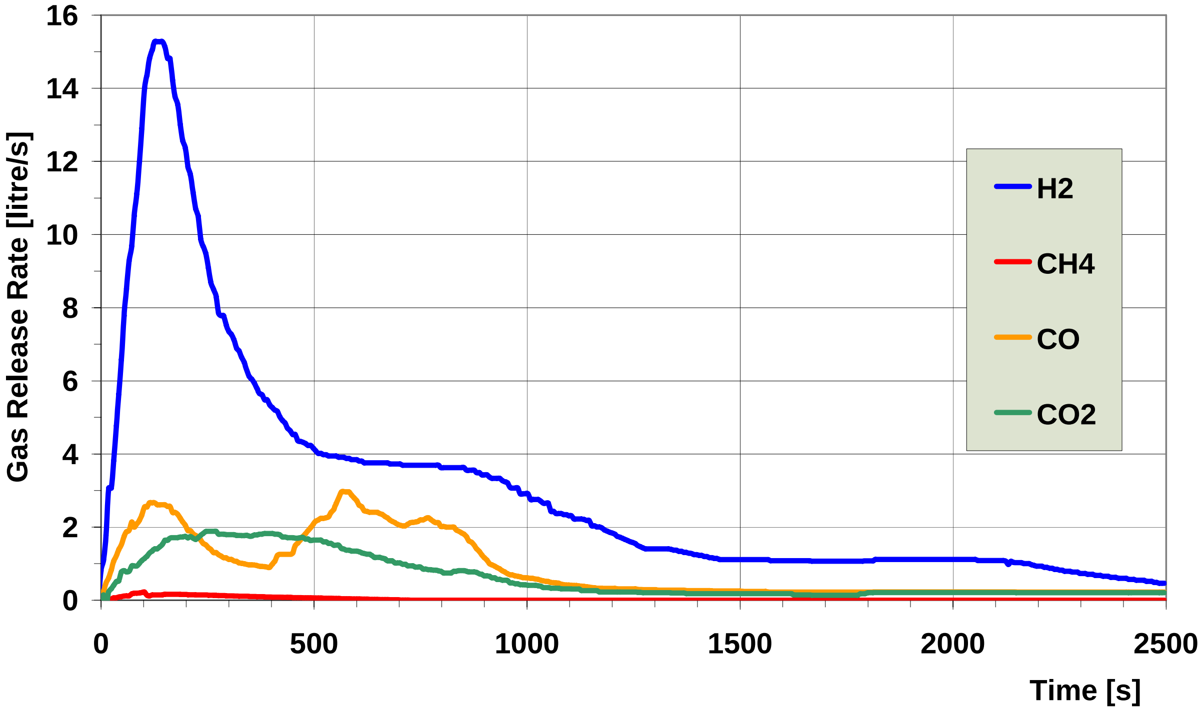

Figure 36: Gas release rates as measured in the off-gas line (without H2O)

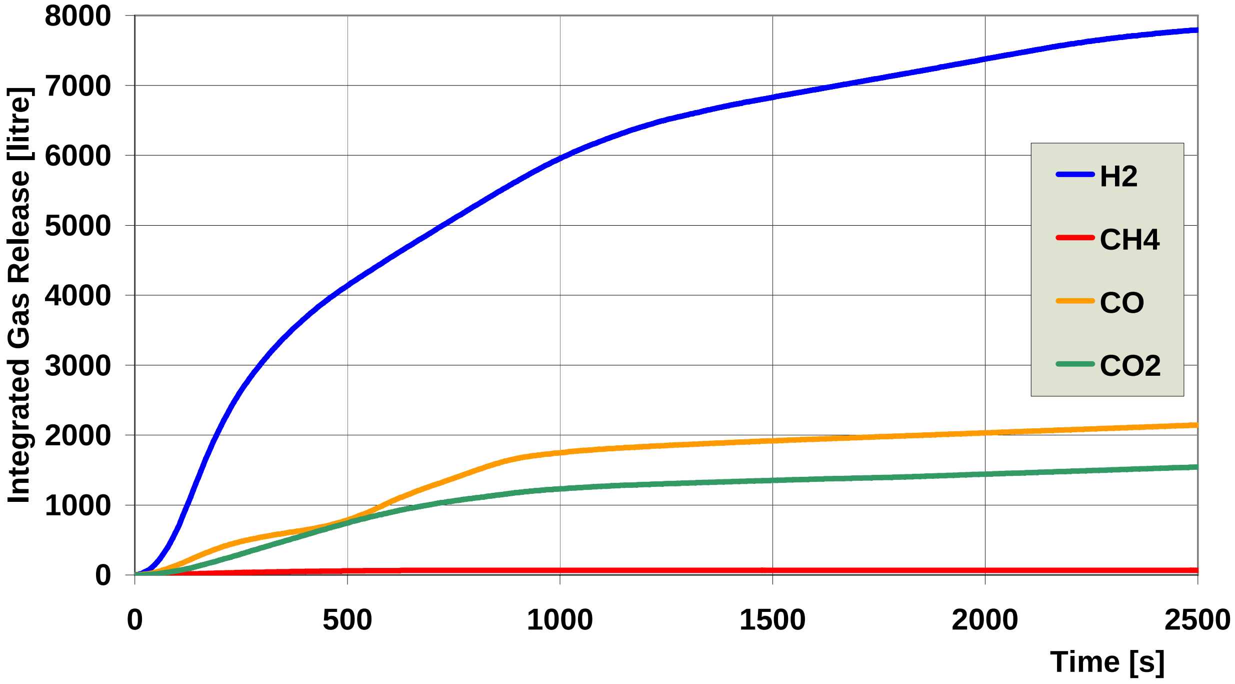

Figure 37. Integrated gas release as measured in the off-gas line (without H2O)

4.5 Flooding and long-term melt behaviour

As described in Chapter 3.3, flooding of the melt surface was initiated by activation of the shower head when the thermocouples had indicated progression of the melt to the –90 mm level. Figure 38 gives the flooding rate versus time.

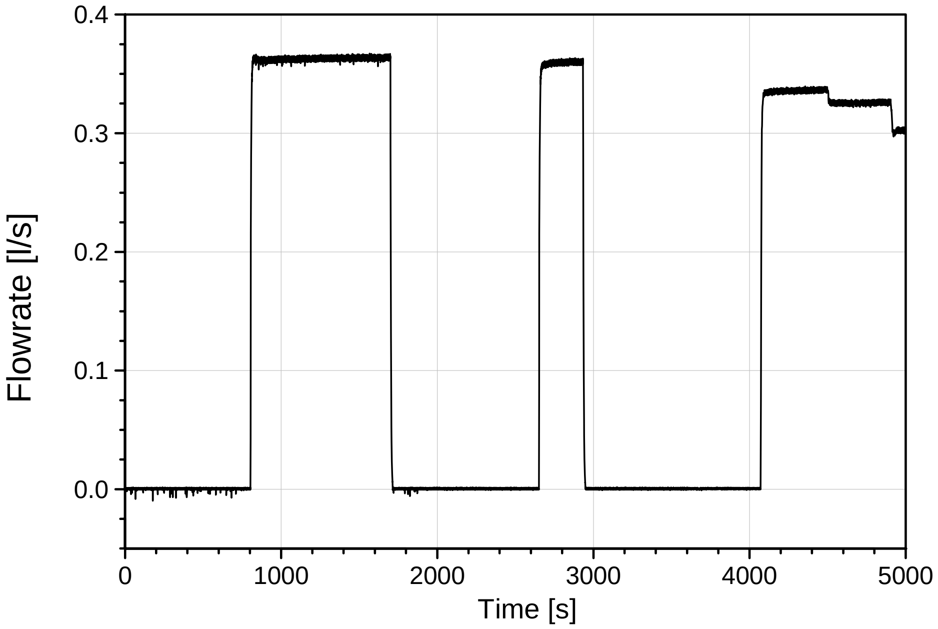

Figure 38: Flow rate of coolant water to flood the melt surface

The flooding rate was 0.375 litres/s in the periods from 800 to 1700 s, from 2650 to 2930 s, and after 4050 s. At 1700 s, the water level had reached the upper rim of the MgO ring, that is more than 70 cm above the initial melt level, at what time flooding was interrupted. Later activation of the shower was performed to replenish the water level, and to extract the energy later on after end of heating.

The coolant spray contacted the melt surface without any significant energetic interaction. Of course, the critical phase is the initial contact phase with the oxide melt while the melt is continuously agitated by the gases from the concrete. However, no mayor melt eruption was observed that would have been caused by entrapment or penetration of water into the melt layer. Several mild eruptions of melt were observed which all were driven by the gases from the concrete. This is valid during the initial phase of formation of a surface crust, but also for the later occurrence of gas driven volcanic eruptions through the crust.

The sequence of crust formation is characterized by the following events (the time refers to start of flooding):

- after ~10 s, the melt surface appears to be covered by a continuous water layer, while the surface is still bright
- after 60 s, first parts of the surface become dark, indicating onset of quenching of a surface crust.
- after 80 s, surface is mostly dark with the exception of 4 hot spots showing ongoing agitation of the melt below, and some gas driven melt eruptions
- at 140 s (940 s after start of melt pour), the melt surface is totally dark, that is: covered by a closed and quenched crust, and submerged with the intensively boiling water layer. Under the surface crust, the hot liquid melt persists. It is important to note, that at this time, the oscillations of the net heating and of the heating efficiency come to an end (Figure 24 and Figure 25).
- from 140 to 960 s: No change in the dark surface crust is observed for this period. Intense boiling from the crust continues. Analysis of the sectioned crucible (Figure 48) indicates that the level of the crust was about 40 cm above the initial bottom.
- at 960 s (1760 s after start of melt pour) start of 1st volcanic eruption. Over a period of 120 s, bright particles of oxide melt are ejected without intense interaction with the water layer. The eruption is driven by gases from the decomposing concrete. Induction heating ends at 1078 s by a signal from the light guide safety instrumentation.
- at 1260 s (2069 s after start of melt pour) start of 2nd gas-driven volcanic eruption over a period of 100 s. Eruption is similar to the 1st. The total amount of particles expelled during the two eruptions is 2.8 kg glassy oxide (Figure 47). .
- after 1360 s (2160s after start of melt pour) slow cool-down of the melt over several hours. At about 1800 s (2600 s after start of melt pour), significant reduction of intensity of boiling.

As heating was switched off at 1078 s (1878 s after start of melt pour), slow cool-down was controlled mainly by transient heat conduction in the solidifying melt. The occurrence of the 2nd volcanic eruption after power-off, however, shows that the bulk of the melt was still liquid. An open point is at what time the large void under the crust was generated that is visible in the sectioned crucible. The reduction of the boiling intensity about 2600 s after start of melt pour may indicate this event. It is supposed that the driving mechanism is pressure build up under the crust which could bulge the crust and separate from the oxide layer. The large void is a highly effective insulator and minimizes heat removal to the overlaying water layer. No ingression of water occurred through the surface crust, as can be derived from the inspection of the completely closed surface crust in Figure 49 and Figure 50. Buckling of the crust by the internal gas pressure and the formation of the volcanic vents explains the rough and irregular crust surface.

Temperature measurements by the thermocouples at the lower interface of the steel and in the concrete show the very slow cool-down after end of heating, which lasts over several hours. This is seen in the Figure 39, which gives the temperatures measured in the instrumentation line T2 in the NW section of the crucible. For the localisation of T2 and the involved thermocouples, see Figure 26a.

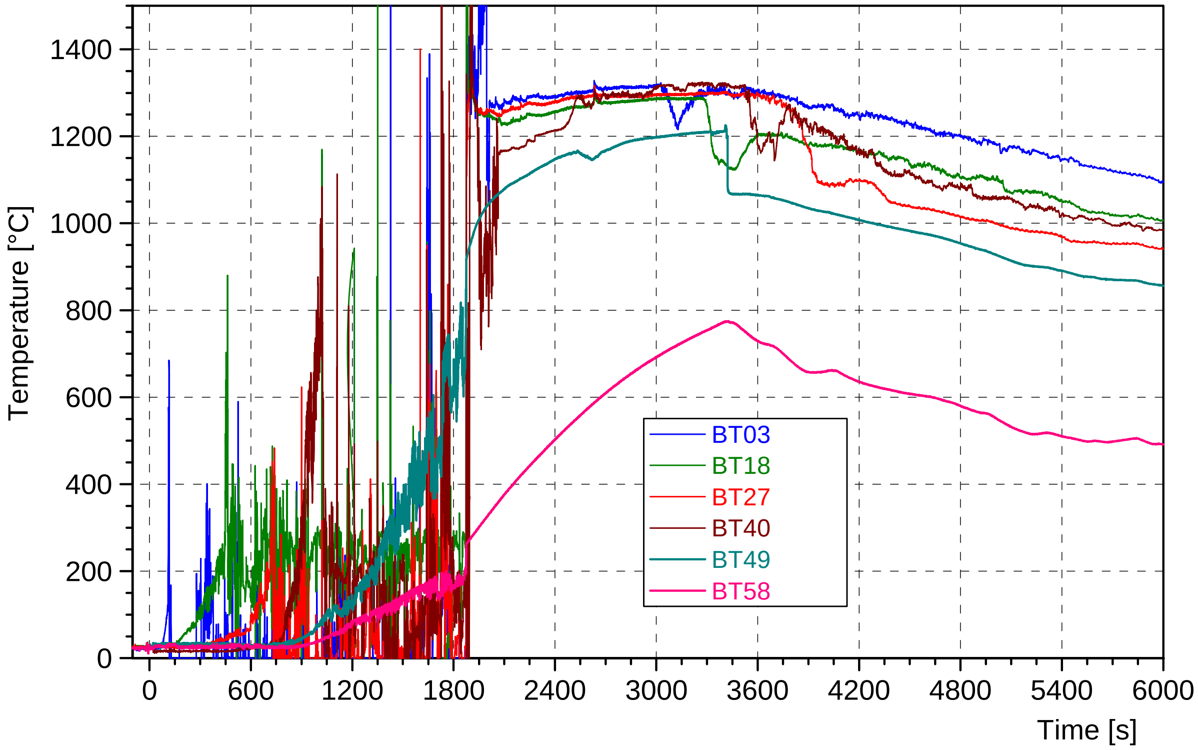

Figure 39: Thermocouples in the bottom of the crucible in instrumentation line T2

After end of heating at 1880 s, the previously melted thermocouples BT03 – BT40 form a new junction at the “melt front” and give reasonable temperatures, that are in fair agreement with BT49. The unbroken thermocouple BT 58 measures the temperature of the concrete some 30 mm from the melt front which is some 500 °C below the front temperature. The important point is that the interface is initially at the melting temperature of the siliceous concrete and cools down only very slowly. This excludes cooling by water contact from above.

This is also confirmed by further thermocouple measurements at the melt/concrete interface in Figure 39, and in the concrete some 10 to 30 mm below the erosion front in Figure 40, registered over more than 6 hours. For the position of the thermocouples see Figure 26. The temperature at the interface after 6 hours is still at 500°C, although complete flooding of the concrete cylinder exists, from the top as well as afterwards from the bottom and the sidewall.

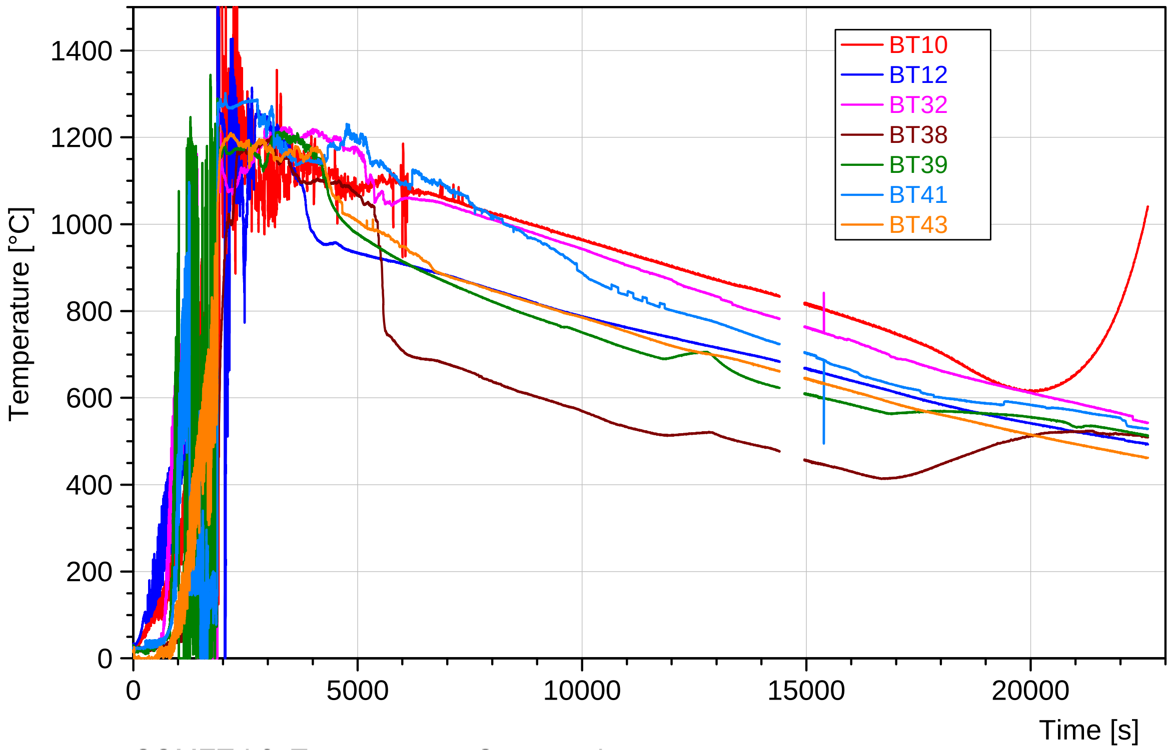

Figure 40: Long term temperatures at the erosion front at the bottom of the cavity

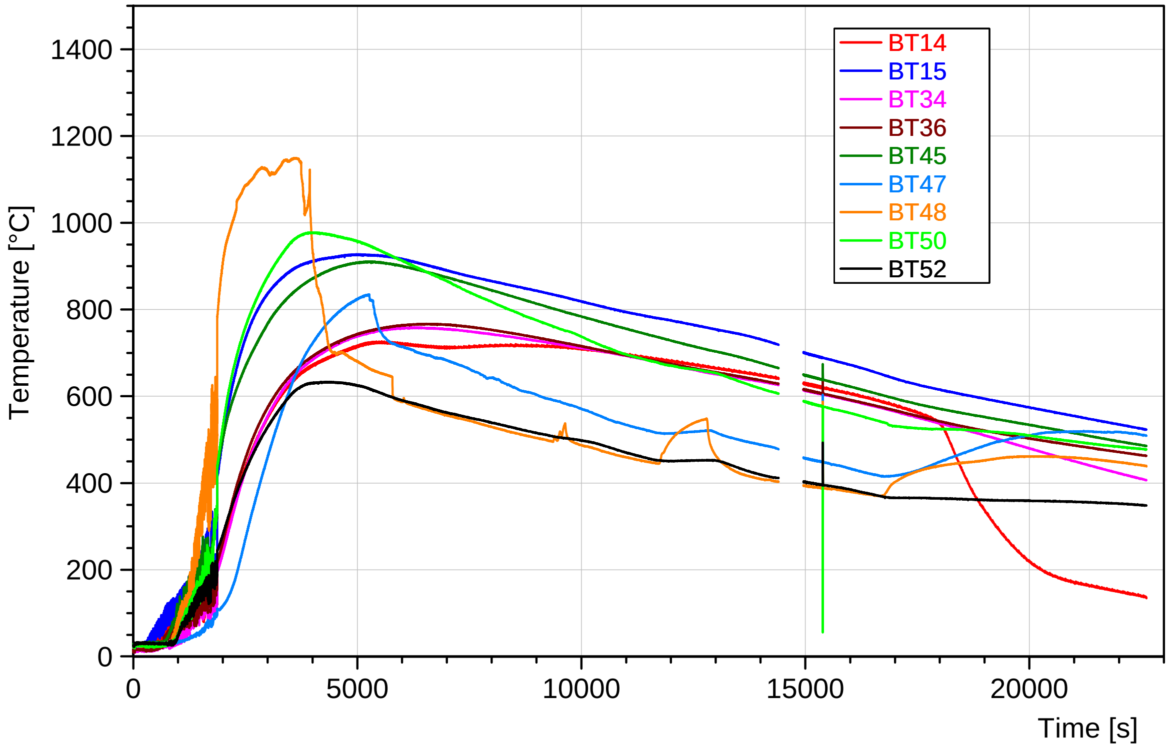

Figure 41: Long term temperatures in the concrete below the erosion front of the cavity

4.6 Post test analyses

Two days after the test, disassembly of the test rig was started to document the status of the cavity and the debris configuration. A first view from above into the open crucible enclosed by the outer protection tube is shown in Figure 42 and a closer view in Figure 43. The schematic of the test rig in Figure 1 gives a better understanding of the geometrical situation.

The outer ring (5) in Figure 42 represents the upper rim of the protection tube. The distance to the melt surface in the centre of the crucible is about 1.7 m. The lower section of the inner cylinder wall (4) of the protection tube is splattered with an oxide melt layer, up to 15 mm thick, which occurred in the initial phase of intense melt/concrete interaction. The surface 3 and 4 represent the rim of the MgO tube and of the concrete crucible, respectively, which are covered by a thicker oxide layer that is black and shiny, and a very thin metal layer directly on the MgO surface. The fee surface of the solidified crust (1) is highly uneven and very rough, and this structure is a result of the ongoing melt agitation during flooding. The volcanic eruptions that occurred later on, may have contributed to the irregular shape, in that mountains were piled up to 180 mm above the crust at the sidewall. The inner diameter of the encrusted upper concrete cavity is 480 mm in direction SW-NE and 450 mm in direction SE-NW.

The central surface and parts of surface (2) are covered by a thin layer of fine oxide particles that were evidently ejected into the water layer during the two volcanic eruptions and settled on the surfaces.

Figure 44 to Figure 46 give further views to the concrete crucible after further disassembly of the protection tubes. No penetrating cracks nor any openings in the crust surface are visible that would allow water penetration to the lower melt. The loose debris consists of green to black glassy oxides, mostly in the form of broken hollow spheres or broken particles, and some in the form of fine whiskers (in the lower part of Figure 46). The size distribution is from 5 to below 1 mm (Figure 47). The structure of the particles is a result of the interaction of the hot ejected glassy melt material with the “cold” coolant water which provokes cracking by thermal stresses. No metal melt was ejected. The mass of the debris is 2.8 kg, the typical layer thickness on the surface is 1 cm. No large loose particles were generated during cooling or during the volcanic eruptions.

Figure 48 is a drawing of the crucible that was completed in the lower part after sectioning of the crucible. It illustrates the subjects described above.

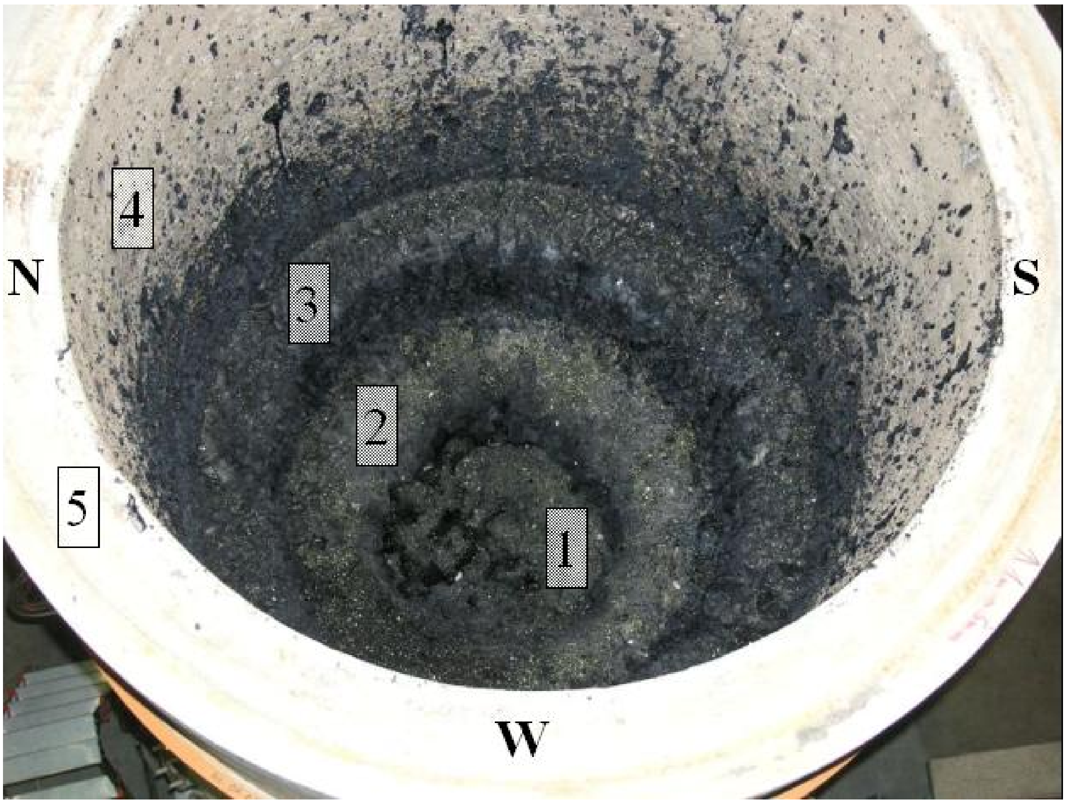

1 solidified melt **2** rim of concrete crucible **3** rim of MgO ring
4 inner surface of protection tube **5** upper rim of protection tube

Figure 42: View into the open facility with the solidified melt (1) at the central bottom

Figure 43: Closer view to the central melt and the rim of the concrete cavity

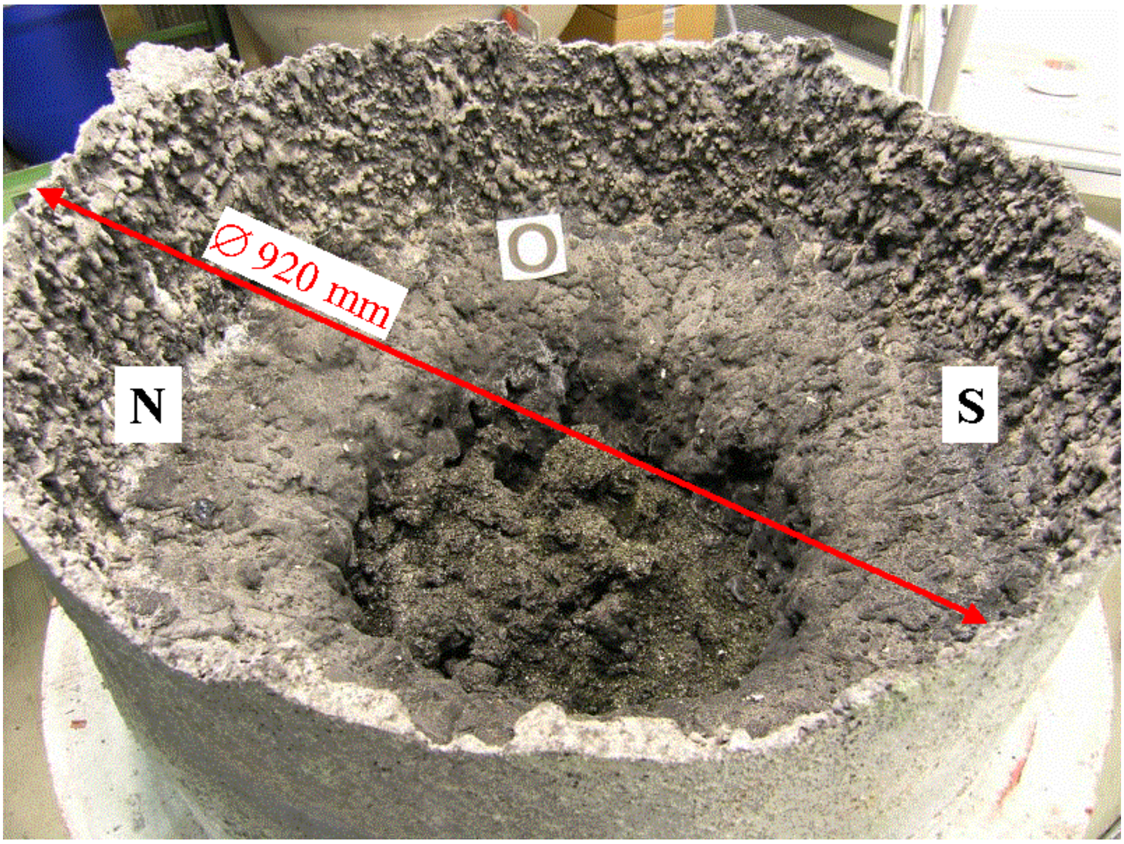

Figure 44: View to melt in the concrete cavity after removal of the protection tube

Figure 45: Closer view to the melt surface and the concrete cavity

Figure 46: Close-up view showing the rough surface partly covered by ejected debris

ll

Figure 47: Loose oxidic/glassy debris ejected during volcanic eruption

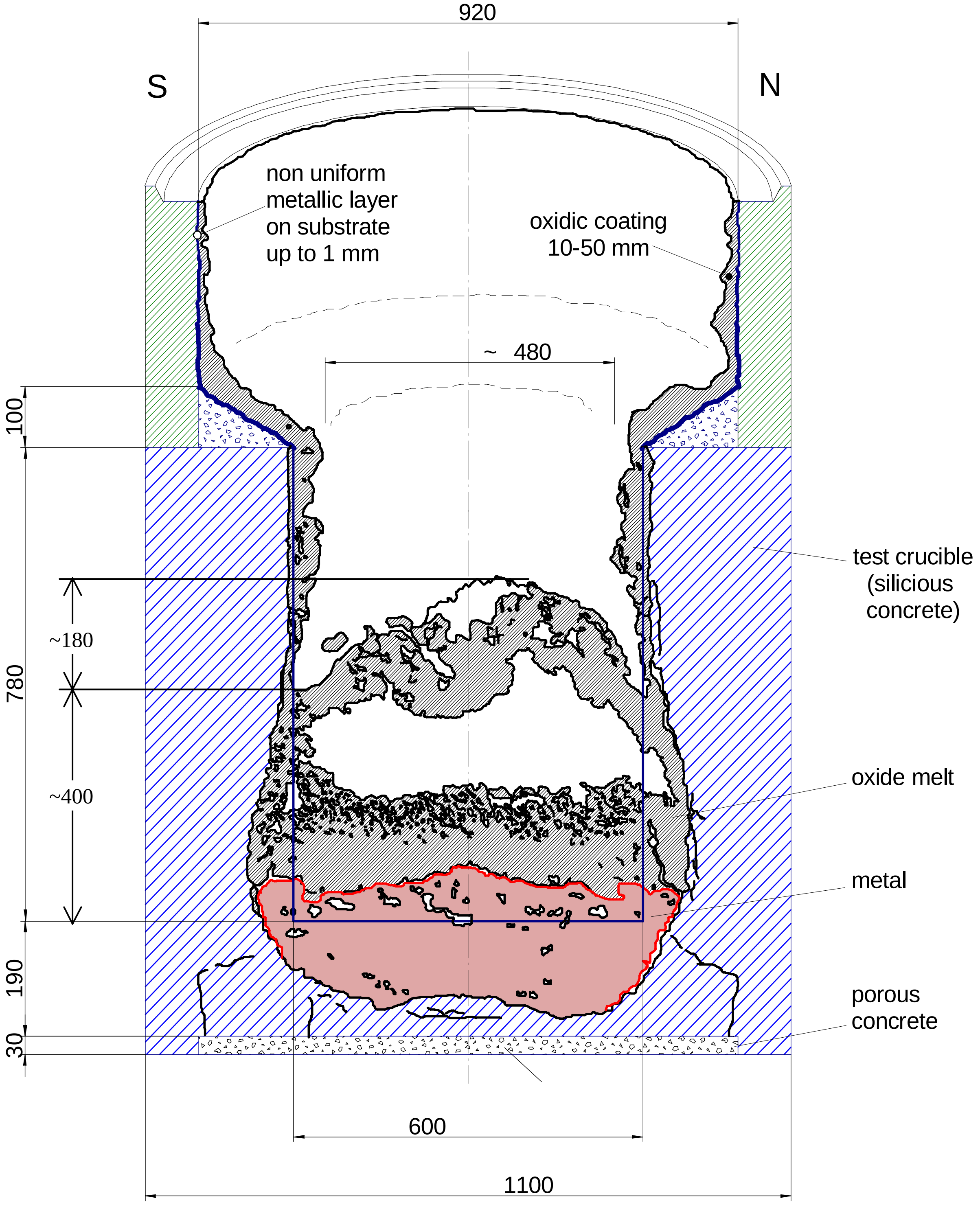

Figure 48: Contour of the melt after the test, taken from the sectioned crucible

Figure 48 to Figure 52 show the crucible after sectioning along the direction S-N. This is 45° rotated against the main instrumentation planes to check the symmetry of the erosion process. The original cavity, 60 cm wide, is indicated by white lines.

The erosion is nearly symmetric with respect to the central axis, but overall downward erosion is about a factor 3 more pronounced than lateral erosion. The maximum downward erosion in is 160 mm, and is about 20 mm more progressed in the north than in the south. Concrete erosion is limited to the contact area with the heated metal melt, whereas erosion by the oxide melt is very low as the temperature of the oxide melt rapidly drops below the “melting” temperature of the concrete. This is a consequence of the restriction of the induction heating technique which does not allow to simulate a representative decay power in the oxide melt.

An other point of interest is the lower erosion near the centreline of the crucible. The reason is the inhomogeneous power distribution in the melt, which is a result of the imperfect heating technique as the induction field is zero at the axis. Fluctuation of the metal melt is evidently not sufficient to compensate this effect. This effect must be taken into account by an “average” erosion process to allow comparison with calculations.

The metal layer has very little void, whereas the void in the oxide varies significantly. The oxide directly above the metal is very dense with few gas bubbles only. The void increases towards the free inner surface, at the transition to the large voided cavity, where it is close to a foamy structure, but with thick lamellas probably determined by the high viscosity of the oxide. The estimated diameter of the gas bubbles in this region is 4 to 10 mm. The free surface of this layer is very rough, like a network that forms when the small gas bubbles collapse.

The large voided cavity in the upper part of the of the oxide layer, is like a huge bubble, 60 cm wide and 10 to 20 cm high. It fills practically the whole cross section of the concrete cylinder. The inner surface of this voided cavity has the same very rough structure everywhere as described above, possibly generated by the collapse of fine gas bubbles. This is also true for the inner surface in the upper dome that is shown in Figure 52. This photo is taken by placing the camera in the cavity, lens upwards.

The upper layer of the oxide above the cavity is a massive crust, some 100 to 200 mm thick, again with some enclosed gas bubbles, but with no open porosity, holes or cracks. A closer view to this upper crust in Figure 51 shows that the crust consists of 2 or 3 different layers of slightly different colour and structure, each 20 to 30 mm thick, that developed from top to bottom. The highest closed porosity in the crust is at the lower interface to the open cavity. As outlined in chapter 4.5, the large cavity has probably formed at about 2600 s, when after surface flooding the gas tight surface crust excluded further gas release, and pressure build up bulged the hot surface crust, starting from the 400 mm level (Figure 48). Also, the two volcanic eruptions may have contributed, especially to the peculiar structure of the crust surface. The highest elevations may represent the volcanic vents. Eventually, the residual oxide melt with a higher content of gas bubbles separated into two layers, the lower and thicker one above the metal layer, and a thinner one attached to the upper crust.

Another important aspect is the presence of un-melted silica gravels in the lower oxide layer, which have a similar size distribution as in the original concrete. The reason for the existence of these gravels is the modified decomposition process of the concrete under low heat flux. The cement matrix decomposes between 700 – 1000°C. The larger gravels with a higher melting temperature loose their mechanical bonding, and thus may be transferred with low temperature melt from the concrete interface into the oxide melt, where they float according to their density on a denser liquid. In the present situation, they are overlaid by a layer of voided oxide melt with lower density. Incomplete melting of the concrete may result in different heat flux distribution and erosion resulting from the lower „melting“ enthalpy of concrete, and bulk cooling of the melt by delayed melting of the aggregates.

The total eroded volume of the concrete cylinder is determined according to the north and south part of the cavity, assuming axis symmetry for each of the contours. Table 11 gives the results and the required decomposition energy, assuming the decomposition enthalpy of 2075 kJ/kg as given in Table 2. The statistical error due to the uncertainty of the eroded volume corresponds to 4.5 %. It is remarkable that the net energy delivered by induction heating (integral of Figure 24), which is 417 MJ, is only some 20 % higher than the calculated erosion energy. It is concluded that for the high concrete erosion the additional initial overheat of the melt and the lower effective decomposition enthalpy play an important role.

Table 11: Eroded concrete volume and related energy

Cavity	**Eroded volume, m^3**	**Eroded mass, kg**	**Energy for erosion, MJ**
contour north	0.0734	163	338
contour south	0.0773	172	356
average	0.0754 ± 0.0033	168	347

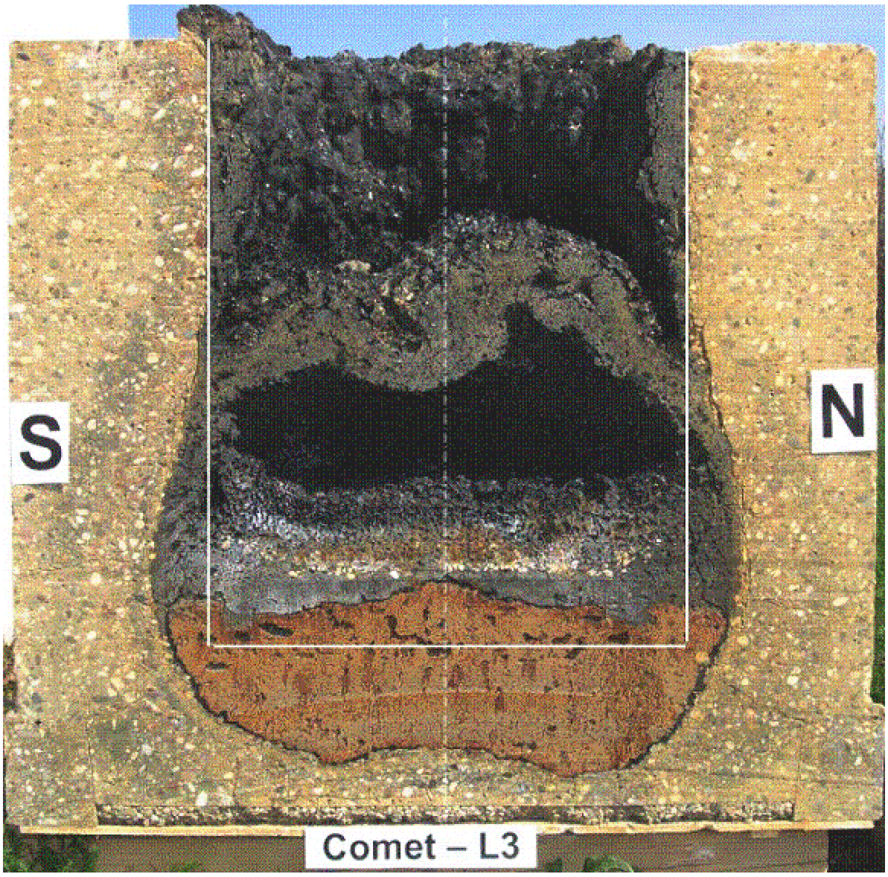

Figure 49: Sectioned crucible. View to plane S-N. White lines show the initial cavity

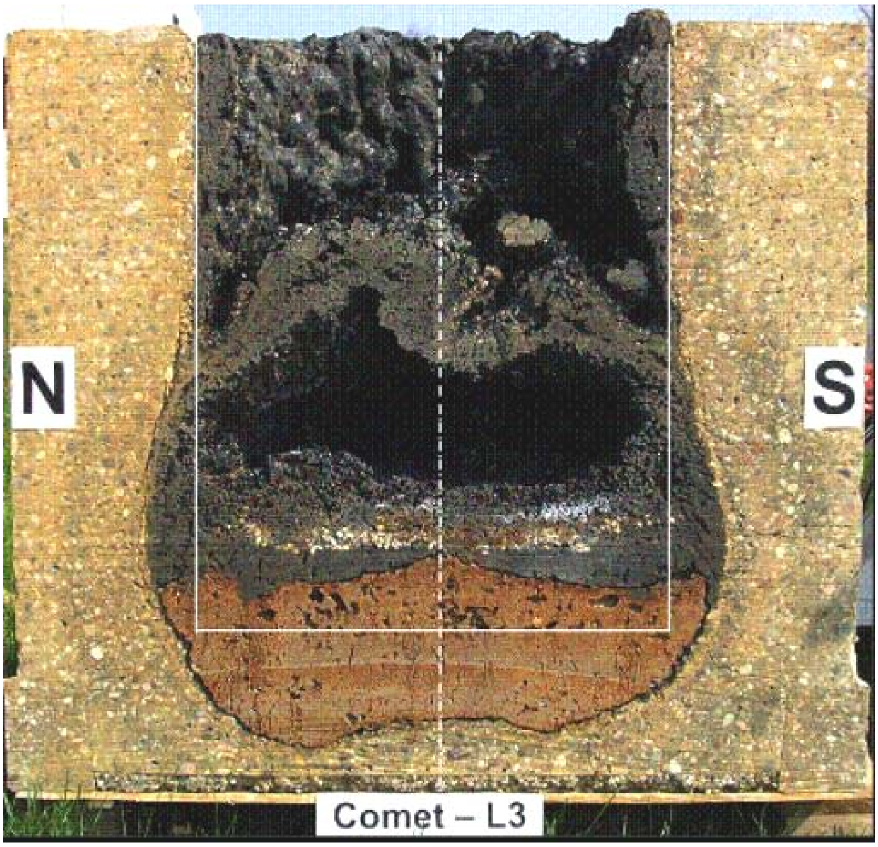

Figure 50: Sectioned crucible. View to plane N-S. White lines show the initial cavity.

Figure 51: Close-up view of the solidified oxide with large inner cavity and crust

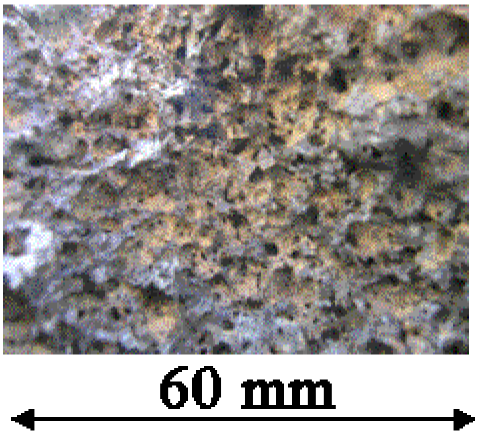

Figure 52. Inner surface of the upper oxide crust as seen from the bottom of the cavity

4.7 Concrete erosion using post test data

The evaluation of concrete erosion is improved, using the data from the sectioned crucible.

Figure 53 and Figure 54 show the photo of the sectioned crucible in comparison with the erosion fronts of Figure 31 and Figure 32 which were determined by the failure of the thermocouples in the concrete crucible. Downward erosion is registered in good agreement, especially if the extrapolated thermocouple data (green line) are considered. Lateral erosion is however underestimated, as the number of thermocouples in the cylindrical section was not sufficient to catch the total erosion. This calls for a supplemental evaluation of the lateral erosion histories that is performed below. Although the plane S-N differs from the instrumentation planes SW-NE and NW-SE, the agreement confirms nearly symmetric erosion. Figure 55 and Figure 56 show the cavity erosion in a different plot.

Figure 57 to Figure 60 give the erosion versus time along all thermocouple instrumentation lines (from chapter 4.3), improved by the information from the sectioned crucible. The dotted lines were drawn as straight lines between the last thermocouple measurement points and the final cavity position. This implicitly assumes that concrete erosion stopped at 1880 s when heating was stopped. The linear interpolation seems a good approximation for the downward erosion histories. However, for the lateral erosion this interpolation may be uncertain and a smoother transition from the early to the late erosion rate may be more appropriate. For any code comparison, these figures are recommended.

For downward erosion rates, the following estimates are confirmed as already listed in chapter 4.3: For the initial high erosion from 0 to 100 s: ~0.15 mm/s; for the subsequent quasi-stationary dry interaction phase from 100 to 800 s: ~0.07 mm/s ± 0.03 mm/s; after start of surface flooding for the period 800 to 1900 s: ~0.04 mm/s.

With the aid of Figure 57 to Figure 60, intermediate cavity forms are constructed using the data at the times 100 s, 200 s, 400 s, 800 s(= start of surface flooding), 1300 s, and 1880 s. These data in Figure 61 are especially useful for code comparison, although the lateral erosion for the times 400 to 1300 s is somewhat uncertain.

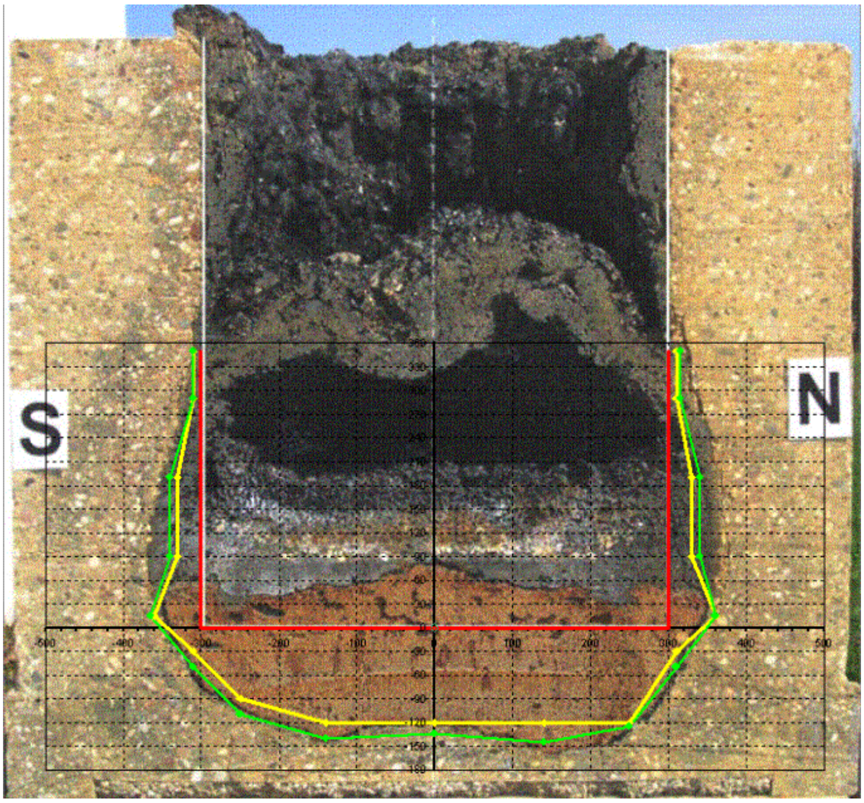

Figure 53: Comparison of sectioned crucible with erosion as measured by thermocouples in plane SW-NE

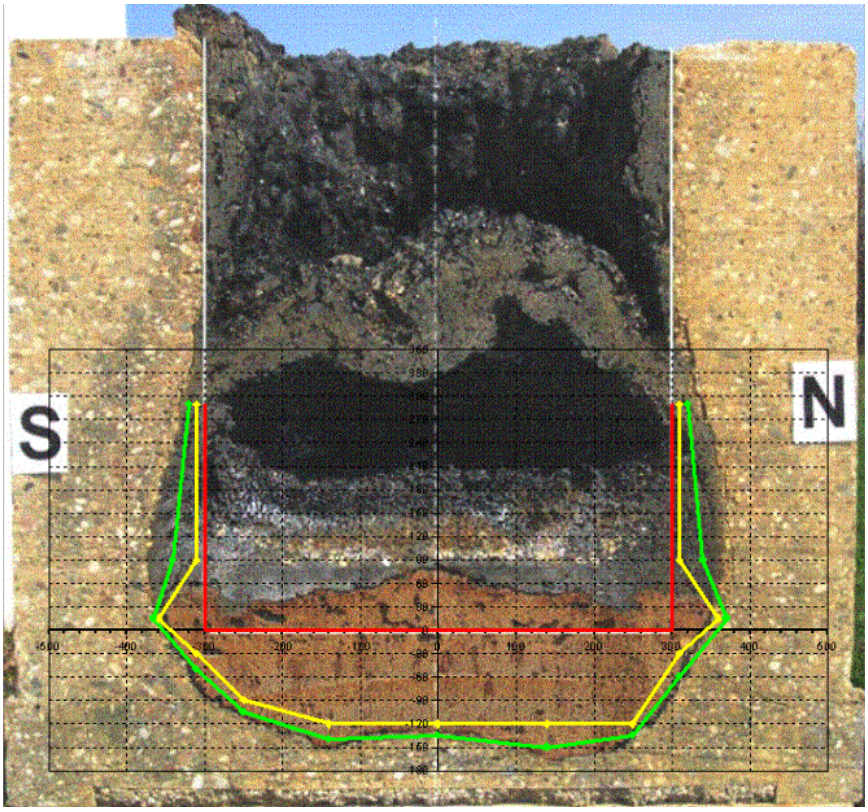

Figure 54: Comparison of sectioned crucible with erosion as measured by thermocouples in plane NW-SE

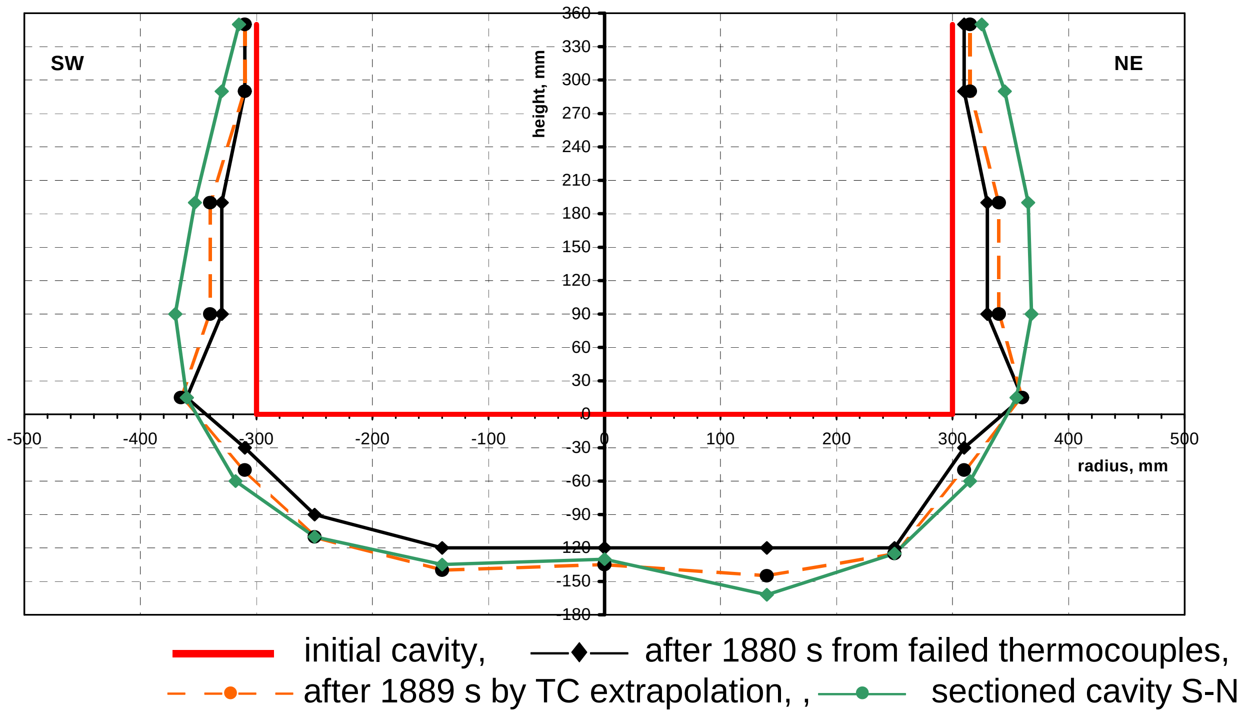

Figure 55: Eroded cavity SW-NE: TC measurements compared with sectioned crucible

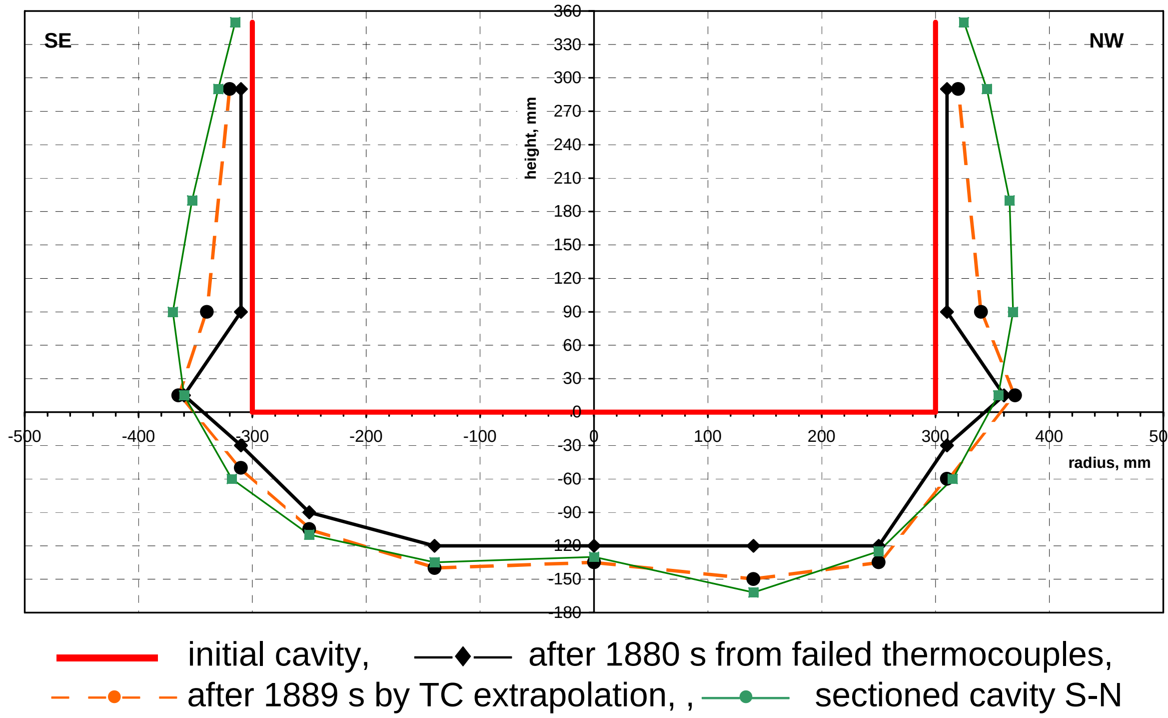

Figure 56: Eroded cavity SE-NW TC measurements compared with sectioned crucible

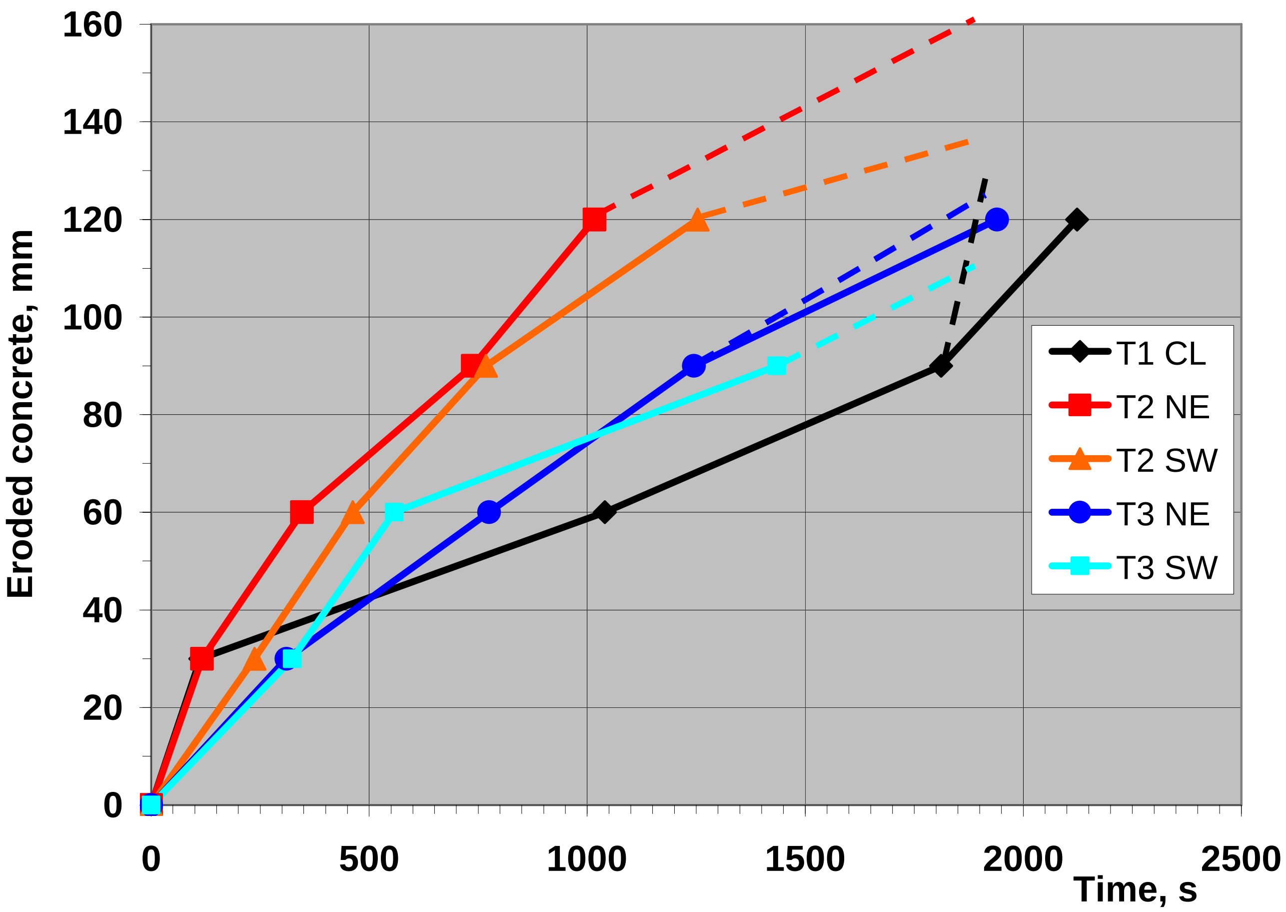

Figure 57: Axial erosion vs time in plane SW-NE, completed by data from sectioned cavity (dotted lines)

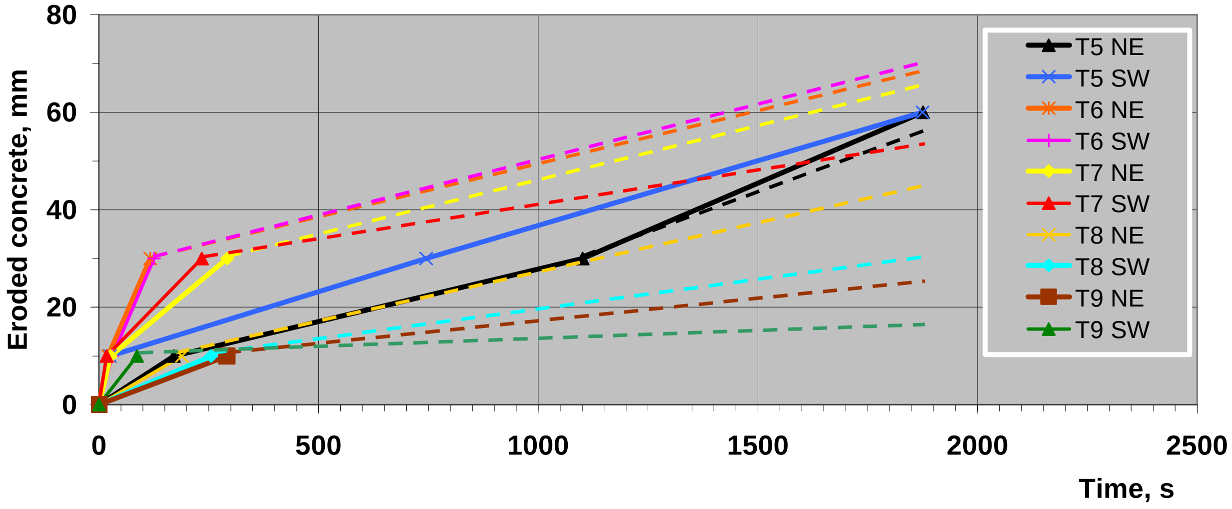

Figure 58: Lateral erosion vs time in plane SW-NE, completed by data from sectioned cavity (dotted lines)

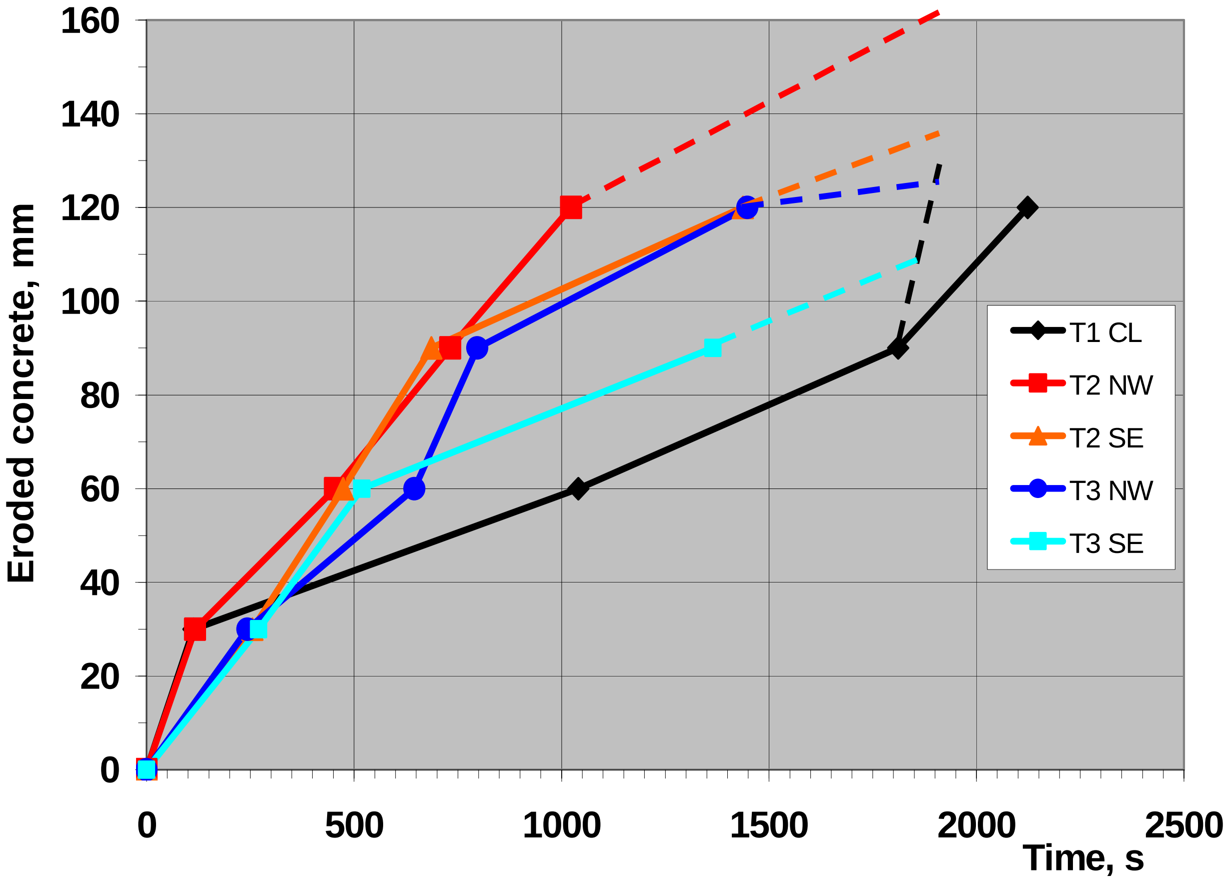

Figure 59: Axial erosion vs time in plane SE-NW, completed by data from sectioned cavity (dotted lines)

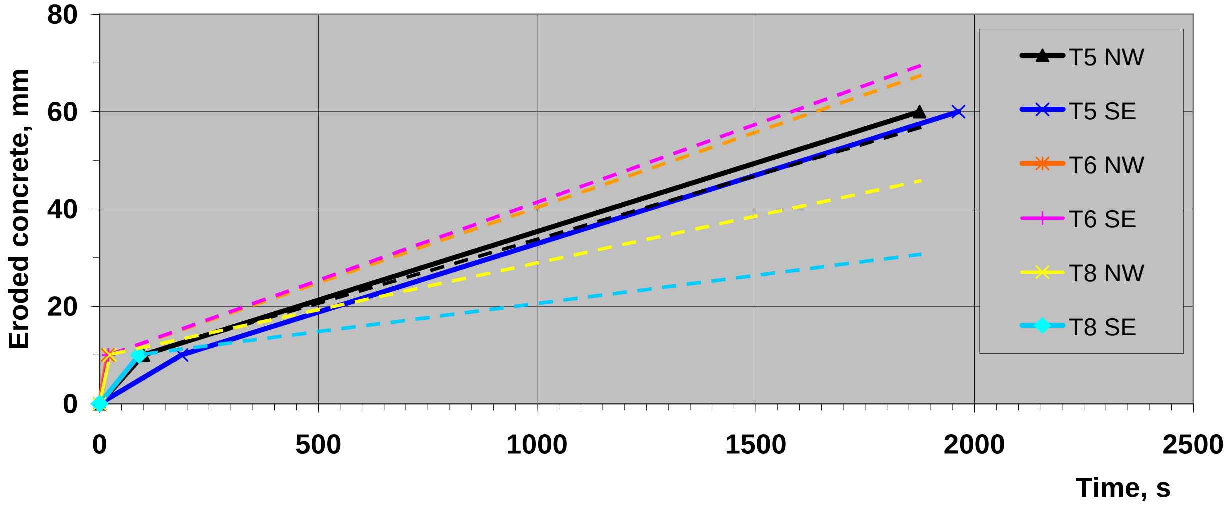

Figure 60: Lateral erosion vs time in plane SE-NW, completed by data from sectioned cavity (dotted lines)

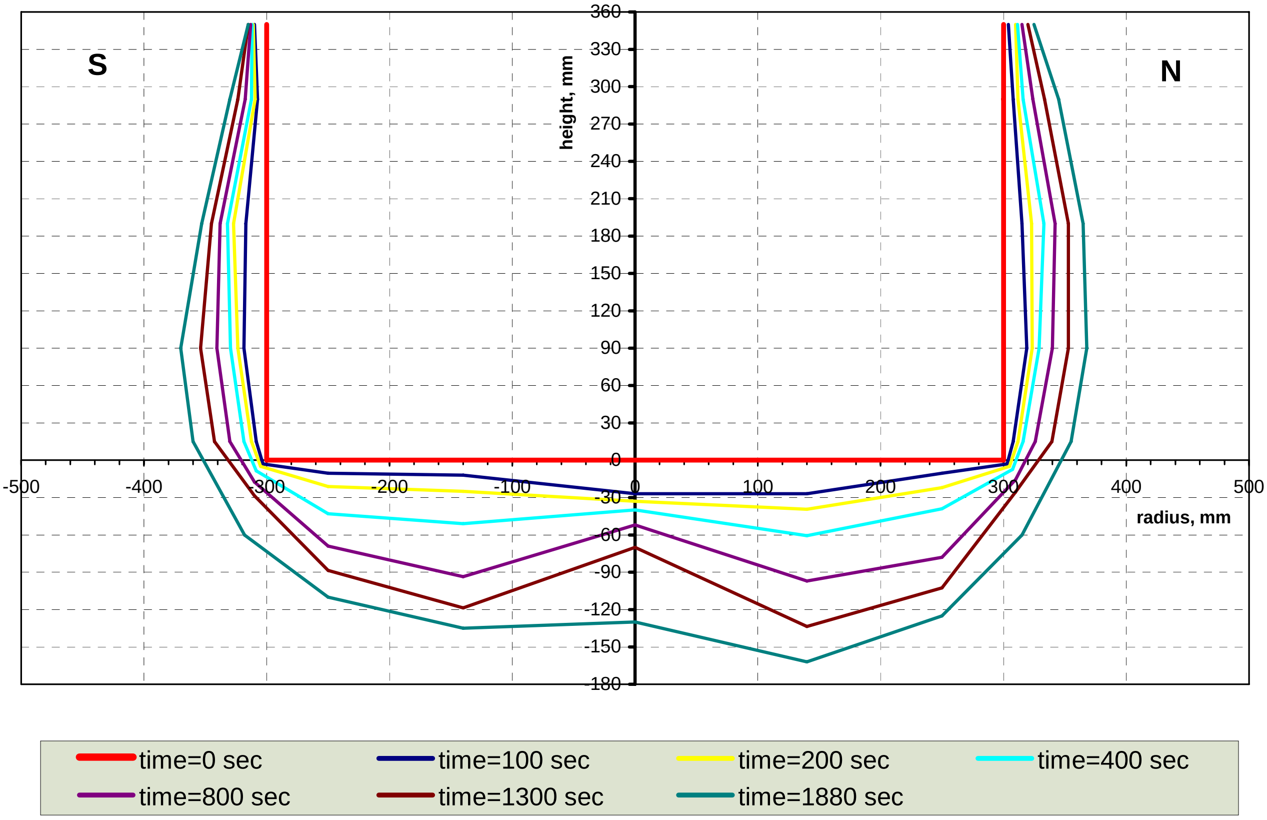

Figure 61: Evolution of cavity versus time during concrete erosion

5 Conclusions

The experiment COMET-L3 was performed successfully as planned. It investigates the two-dimensional concrete erosion in a cylindrical crucible fabricated from siliceous concrete in the first phase of the test, and the influence of surface flooding in the second phase. Decay heating in the 2-component metal + oxide melt is simulated by sustained induction heating of the metal phase that is overlaid by the oxide melt.

The inner diameter of the concrete crucible was 60 cm, the initial mass of the melt was 425 kg steel and 211 kg oxide at 1665°C. The net power to the metal melt was about 220 kW from 0 to 1880 s. Surface flooding was initiated at 800 s with continuous heating that was eventually terminated when the maximum allowed erosion was reached. The experiments aims to quantify process that are important during long-time concrete erosion of a core melt accident.

The main observations and results of the test are as follows:

Dry melt/concrete interaction

- In the initial phase of the test (less than 100 s), the overheated, highly agitated melt causes an intense interaction with the concrete. Parts of the melt are splashed to the upper structures. The intense interaction leads to fast decrease of the initial melt overheat and reduction of the initially high concrete erosion rate. In the initial phase of some 100 s. The erosion rate by the steel phase is similar into the axial and radial direction and is ~0.15 mm/s. Concrete erosion by the oxide melt in the upper part of the crucible is however small and stops after not more than 10 mm erosion, as the oxide temperature falls below the “melting” temperature of concrete.
- Thereafter, under quasi-stationary conditions until about 800 s, the erosion by the metal melt slows down and is some 0.07 mm/s into the axial direction. Lateral erosion is a factor 3 smaller. This is in agreement with the results of COMET-L1 [7] and –L2 [8], and the former BETA experiments [2] at low power density.
- Video observation of the melt surface shows an agitated melt with ongoing gas release from the decomposing concrete. Some periods of more intense gas release, gas driven splashing and release of crusts from the concrete interface indicate the existence and iterative break-up of crusts that probably form at the steel/concrete interface. This

correlates with fluctuations of induction power that is due to a changing geometry of the melt and results in a different coupling efficiency to the induction field.

- During this period burnable gases are released as a result of chemical reaction of steam and CO_2 with iron. The dominant gas is H_2.
- After about 800 s the melt exceeds the -80 mm downward erosion level and surface flooding is initiated.

Influence of surface flooding

- Surface flooding of the oxide melt is initiated at 800 s by a shower from the crucible head with 0.375 litre water/s. At start of flooding, the melt has no surface crust and the surface is moderately agitated by gases from below.
- Flooding does not lead to strong melt/water interactions and no entrapment reactions or penetration of water into the melt did occur. Any melt ejections or volcanic actions that occur, are driven by gases from the concrete.
- A nearly closed surface crust forms within 60 s after start of flooding and quenches after not more than 140 s. Residual holes in the crust are closed and the crust separates the coolant water overlayer and the hot melt below. The surface crust prevents strong agitation of the melt and favours the existence of a settled steel layer, possibly with a crust at the concrete interface, as the power fluctuations of induction heating come to an end. At the same time, the release of H_2, CO and CO_2 is reduced, which may indicate the existence of the bottom steel crust with a certain contact resistance for downward heat transfer.
- The concrete erosion continues, although reduced with some 0.040 mm/s, and eventually the melt reaches the maximum erosion limit of the crucible, at what time the simulated decay power is cut off.
- Two volcanic melt eruptions, that developed at the crust surface for a duration of 2 min each, had minor influence on coolabilty. Only 2.8 kg oxide particles were ejected into the overlaying water pool. Finally, the volcanic vents were blocked, and there are no indications that water ingression occurred through the surface crust.
- Cool-down after end of heating was very slow, although additional flooding brought water to all sides of the concrete crucible. After 6 hours, the bulk temperature of the (solidified) melt was still at 500°C.

Post test analyses

- Post test analysis of the solidified melt shows that a large void had developed under the surface crust. The crust was bulged some 20 cm above its initial level, probably by pressure build-up from the gases of decomposing concrete. Water ingression to the bulk of the oxide and metal material was prevented by the massive and tight crusts and by the absence of cracks and holes. No efficient fragmentation mechanism was identified that could contribute to melt cooling

- Unmelted aggregates of the concrete are found in the oxide layer. This refers to an incomplete melting of the concrete which is due to the destruction of the cement matrix at lower temperatures and low heat fluxes.

- A course energy balance, neglecting heat conduction in the concrete and the initial melt overheat, shows that the energy which is needed to melt the eroded concrete volume corresponds to about 80 % of the energy that is supplied by the simulated decay heat. Consequently, while most of the decay power is used to melt the concrete, only some 20 % of the decay power are transferred directly through the upper melt surface or to the water overlayer. This confirms, that the influence of surface flooding is indeed small in this experiment and unable to stop downward erosion

The present experiment considers the long-term situation of corium/concrete interaction, after the metal melt is layered beneath the oxide melt. Experimental restrictions did not allow to deposit decay heat also in the oxide melt. Nevertheless, the experiment shows many phenomena that are important to understand and to model the late phase of a core melt accident, and shall be used for model and code validation. Detailed experimental data are given, especially for concrete erosion by the metal melt, for time dependent cavity formation, and for the influence of surface flooding. Other experimental data, that become available from experiments with pure oxidic corium melts with UO_2-ZrO_2 mixtures [5,6], extend and complement our understanding on corium behaviour.

With respect to the limitation of surface cooling by formation of a surface crust as observed in the present experiment, the question arises if a surface crust would be stable in a much larger scale e.g. of 6 m diameter, as is typical for LWRs. The large scale ECOKATS-2 experiment that was carried out at Forschungszentrum Karlsruhe in a 2 m x 2 m wide concrete cavity with 3200 kg melt has indeed shown that further phenomena may occur [11]. In agreement with the present test, very fast formation of a surface crust was observed as well as very limited ejection of oxide melt by volcanic eruptions. The long term gas release from ongoing concrete decomposition, that caused bulging of the surface crust and formation of one single, large gas bubble in COMET-L3, elevated the initial crust in ECOKATS-2 incoherently over the large surface and led to formation of several superposed crusts, up to 20 cm high with open and closed porosities, that were cooled and stabilized by the overlaying coolant water. The melt underneath, however, subsequently solidified without open porosities and was not coolable. Common to both experiments is that formation of elevated crusts and porosities is driven by gases from the concrete, and not by ingress of the overlaying water, as is hypothesized by some research groups [5, 6].

In summary, the new experiments show intense coupling of very complex physical and chemical processes that are extremely difficult to quantify. Uncertainties in our understanding, in code modelling, and in the application to reactor scale will undoubtedly persist. It is therefore necessary under the aspect of safety assessment to give a reasonable estimate of the remaining uncertainty band.

6 References

[1] H. Alsmeyer, M. Reimann, Hydrodynamics and Heat Transfer Processes of Dry Ice Slabs Sublimating in Liquid Pools, 7th Int. Heat Transfer Conf. 1982, Munich, Vol. 5, 167-173, (Eds.: U. Grigull et al. Washington, DC: Hemishere Publ. Co.)

[2] H. Alsmeyer, BETA Experiments in Verification of the WECHSL Code: Experimental Results on Melt-Concrete Interaction, Nucl. Eng. and Design, 103 (1987) 115-125.

[3] I.B. Wall, B.R. Sehgal, Molten Corium Concrete Interactions. Advanced Containment Experiments (ACE) Project: Summary Report, EPRI TR-103483 (1993)

[4] J.J. Foit, Modeling of Oxidic Molten Core-Concrete Interaction in WECHSL, Nucl. Eng. and Design, 170 (1996) 73-79

[5] M.T. Farmer, S. Lomperski, S. Basu, Results of Reactor Material Experiments Investigating 2-D Core-Concrete Interaction and Debris Coolability, ICAAP ’04, ICAPP-4102, Pittsburgh, PA, June 13-17 (2004)

[6] M.T. Farmer, S. Lomperski, S. Basu, The Results of the CCI-2 Reactor Material Experiment Investigating 2-D Core-Concrete Interaction and Debris Coolability, 11th International Topical Meeting on Nuclear Reactor Thermal-Hydraulics, Avignon, Oct. 2-6 (2005)

[7] G. Doubleva, H. Alsmeyer, T. Cron, B. Fluhrer, J. Foit, G. Messemer, A. Miassoedov, S. Schmidt-Stiefel, T. Wenz, I. Ivanov, M. Cranga, The COMET-L1 Experiment on Long-Term MCCI and Late Melt Surface Flooding, SAM-LACOMERA-D14, FZKA 7213, 2006.
H. Alsmeyer, et al., The COMET-L1 Experiment on Long-Term Concrete Erosion and Surface Flooding, 11th International Topical Meeting on Nuclear Reactor Thermal-Hydraulics, Avignon, Oct. 2-6 (2005)

[8] G. Sdouz, R. Mayrhofer, H. Alsmeyer, T. Cron, B. Fluhrer, J. Foit, G. Messemer, A. Miassoedov, S. Schmidt-Stiefel, T. Wenz, The COMET-L2 Experiment on Long-Term MCCI with Steel Melt, SAM-LACOMERA-D15, FZKA 7214, 2006.

[9] Miassoedov et al., Large Scale Experiments on Core Degradation, Melt Retention and Coolability (LACOMERA). FISA-2003: EU Research in Reactor Safety, Luxembourg, L, November 10-13, 2003, Preproc. p. 239-244.

[10] G. Schumacher, Internal note, November 2005.

[11] H. Alsmeyer, T. Cron, G. Messemer, W. Haefner, ECOKATS-2: A large scale experiment on melt spreading and subsequent cooling by top flooding, Proc. ICAPP ’04, Pittsburgh, PA, 2004, Paper 4134.

Appendices

Appendix A: Summary of the realized test conditions

- **Concrete crucible**

Siliceous concrete crucible, 1100 mm $\varnothing_a$ x 1000 mm high, 600 mm $\varnothing_I$ x 780 mm high, fabricated with cement of the type blast furnace cement CEM III/B 32.5 NW/HS; crucible instrumented with 90 NiCr-Ni thermocouples

- **Melt**

Melt generated by thermite mixture (preheated to 250°C control temperature during > 36 h) and poured into concrete crucible.
425 kg steel (Fe with 10 w% Ni) and 211 kg oxide (56 % Al2O3 and 44 % CaO)
(residual oxide transferred to the slag wagon)
initial temperature of melt 1665°C

- **Cover gas into hood**

Ar gas flow: 50 m^3/h main flow plus (8 + 9) m^3/h from windows

- **Cameras**

On top of crucible: 1 Video (Sony), 1 Infrared camera
spout: 1 Video; end of off-gas tube: 1 Video; experimental hall: 3 Videos

- **Induction heating**

Net power deposited in the metal melt: ~220 kW from 0 – 1880 s

Initial voltage of inductor: 2.6 kV, maximum voltage 2.6 kV, reduction of voltage when heating efficiency increases during concrete erosion

- **Test procedure**

<u>Phase 1:</u> Dry MCCI test until –80 mm downward concrete erosion during about 13 min, erosion detected on-line by thermocouples
<u>Phase 2:</u> Onset of surface flooding by shower head with 22.5 litre/min until –170 mm concrete are erosion or upon failure of light guides.
Subsequently, flooding of bottom and sidewalls of the concrete crucible to protect the test rig and to cool down the melt.

- **Further details:**

The turbine flow-meter was inserted into the off-gas line but no measurements were received. Prandtl tube in the off-gas line gave no valid signals after flooding was started.

Small Ar gas flow through the porous bottom layer allows measurement of T-increase if melt approaches or penetrates lowest concrete interface. No significant T-increase measured as melt did not reach the lower interface.

Appendix B: Data acquisition and channel assignments

Table B-1 lists all signals that are registered on the MICROLINK data acquisition system. The blocks 1, 2, 3, 5, 7, 9, and 11 of MICRLONK are equipped with high quality differential amplifiers, the blocks 4, 6, 8, 10,and 12 have ”single ended“ amplifier inputs with less noise reduction.

Table B-1: COMET-L3 Channel assignment for Microlink-data acquisition system

Log. Kan	HW Kan.	Block	Name	Variable	Sensor	Position: r,Φ,h
1	0	01:00	BT 1	Betontemperatur	NiCr/Ni	0, 0, -30
2	1	01:01	BT 2	Betontemperatur	NiCr/Ni	140, 45, -30
3	2	01:02	BT 3	Betontemperatur	NiCr/Ni	140, 135, -30
4	3	01:03	BT 6	Betontemperatur	NiCr/Ni	250, 45, -30
5	4	01:04	BT 7	Betontemperatur	NiCr/Ni	250, 135, -30
6	5	01:05	BT 10	Betontemperatur	NiCr/Ni	310, 45, -30
7	6	01:06	BT 11	Betontemperatur	NiCr/Ni	310, 135, -30
8	7	01:07	BT 14	Betontemperatur	NiCr/Ni	350, 45, -30
9	8	01:08	BT 16	Betontemperatur	NiCr/Ni	0, 0, -60
10	9	01:09	BT 17	Betontemperatur	NiCr/Ni	140, 45, -60
11	10	01:10	BT 18	Betontemperatur	NiCr/Ni	140, 135, -60
12	11	01:11	BT 21	Betontemperatur	NiCr/Ni	250, 45, -60
13	12	01:12	BT 22	Betontemperatur	NiCr/Ni	250, 135, -60
14	13	01:13	BT 25	Betontemperatur	NiCr/Ni	0, 0, -90
15	14	01:14	BT 26	Betontemperatur	NiCr/Ni	140, 45, -90
16	15	01:15	BT 27	Betontemperatur	NiCr/Ni	140, 135, -90
17	32	02:16	TE-3	TE-Ref. Modul 3	Pt 100	Mainframe
18	33	03:00	BT 30	Betontemperatur	NiCr/Ni	250, 45, -90
19	34	03:01	BT 31	Betontemperatur	NiCr/Ni	250, 135, -90
20	35	03:02	BT 34	Betontemperatur	NiCr/Ni	310, 45, -90
21	36	03:03	BT 35	Betontemperatur	NiCr/Ni	310, 135, -90
22	37	03:04	BT 38	Betontemperatur	NiCr/Ni	0, 0, -120
23	38	03:05	BT 39	Betontemperatur	NiCr/Ni	140, 45, -120
24	39	03:06	BT 40	Betontemperatur	NiCr/Ni	140, 135, -120
25	40	03:07	BT 43	Betontemperatur	NiCr/Ni	250, 45, -120
26	41	03:08	BT 44	Betontemperatur	NiCr/Ni	250, 135, -120
27	42	03:09	BT 4	Betontemperatur	NiCr/Ni	140, 225, -30
28	43	03:10	BT 5	Betontemperatur	NiCr/Ni	140, 315, -30
29	44	03:11	BT 8	Betontemperatur	NiCr/Ni	250, 225, -30
30	45	03:12	BT 9	Betontemperatur	NiCr/Ni	250, 315, -30
31	46	03:13	BT 12	Betontemperatur	NiCr/Ni	310, 225, -30

32	47	03:14	BT 13	Betontemperatur	NiCr/Ni	310, 315, -30
33	48	03:15	BT 15	Betontemperatur	NiCr/Ni	350, 225, -30
34	65	04:16	TE-5	TE-Ref. Modul 5	Pt 100	Mainframe
35	66	05:00	BT 19	Betontemperatur	NiCr/Ni	140, 225, -60
36	67	05:01	BT 20	Betontemperatur	NiCr/Ni	140, 315, -60
37	68	05:02	BT 23	Betontemperatur	NiCr/Ni	250, 225, -60
38	69	05:03	BT 24	Betontemperatur	NiCr/Ni	250, 315, -60
39	70	05:04	BT 28	Betontemperatur	NiCr/Ni	140, 225, -90
40	71	05:05	BT 29	Betontemperatur	NiCr/Ni	140, 315, -90
41	72	05:06	BT 32	Betontemperatur	NiCr/Ni	250, 225, -90
42	73	05:07	BT 33	Betontemperatur	NiCr/Ni	250, 315, -90
43	74	05:08	BT 36	Betontemperatur	NiCr/Ni	310, 225, -90
44	75	05:09	BT 37	Betontemperatur	NiCr/Ni	310, 315, -90
45	76	05:10	BT 41	Betontemperatur	NiCr/NI	140, 225, -120
46	77	05:11	BT 42	Betontemperatur	NiCr/Ni	140, 315, -120
47	78	05:12	BT 45	Betontemperatur	NiCr/Ni	250, 225, -120
48	79	05:13	BT 46	Betontemperatur	NiCr/Ni	250, 315, -120
49	80	05:14	BT 47	Betontemperatur	NiCr/Ni	0, 0, -150
50	81	05:15	BT 50	Betontemperatur	NiCr/Ni	140, 225, -150
51	98	06:16	TE-7	TE-Ref. Modul 7	Pt 100	Mainframe
52	99	07:00	BT 51	Betontemperatur	NiCr/Ni	140, 315, -150
53	100	07:01	BT 54	Betontemperatur	NiCr/Ni	250, 225, -150
54	101	07:02	RT 1	Kühlwasser ein Joche	NiCr/Ni	Jochkühlung
55	102	07:03	RT 2	Kühlwasser aus Joche	NiCr/Ni	Jochkühlung
56	103	07:04	RT 10	Rückfl. Schm.KW Nord	NiCr/Ni	Rücklaufleitung N.
57	104	07:05	BT 48	Betontemperatur	NiCr/Ni	140, 45, -150
58	105	07:06	BT 49	Betontemperatur	NiCr/Ni	140, 135, -150
59	106	07:07	BT 52	Betontemperatur	NiCr/Ni	250, 45, -150
60	107	07:08	BT 53	Betontemperatur	NiCr/Ni	250, 135, -150
61	108	07:09	BT 57	Betontemperatur	NiCr/Ni	140, 45, -170
62	109	07:10	BT 55	Betontemperatur	NiCr/Ni	250, 315, -150
63	110	07:11	BT 56	Betontemperatur	NiCr/Ni	0, 0, -170
64	111	07:12	BT 59	Betontemperatur	NiCr/Ni	140, 225, -170
65	112	07:13	BT 60	Betontemperatur	NiCr/Ni	140, 315, -170

66	113	07:14	BT 63	Betontemperatur	NiCr/Ni	250, 225, -170
67	114	07:15	BT 64	Betontemperatur	NiCr/Ni	250, 315, -170
68	131	08:16	TE-9	TE-Ref. Modul 9	Pt 100	Mainframe
69	132	09:00	BT 58	Betontemperatur	NiCr/Ni	140, 135, -170
70	133	09:01	BT 61	Betontemperatur	NiCr/Ni	250, 45, -170
71	134	09:02	BT 66	Betontemperatur	NiCr/Ni	310, 225, +350
72	135	09:03	BT 69	Betontemperatur	NiCr/Ni	310, 225, +290
73	136	09:04	BT 62	Betontemperatur	NiCr/Ni	250, 135, -170
74	137	09:05	BT 65	Betontemperatur	NiCr/Ni	310, 45, +350
75	138	09:06	BT 67	Betontemperatur	NiCr/Ni	310, 45, +290
76	139	09:07	BT 68	Betontemperatur	NiCr/Ni	310, 135, +290
77	140	09:08	BT 70	Betontemperatur	NiCr/Ni	310, 315, +290
78	141	09:09	BT 72	Betontemperatur	NiCr/Ni	310, 225, +190
79	142	09:10	RT 11	Rückfl. Schm.KW Süd	NiCr/Ni	Rücklaufleitung S.
80	143	09:11	BT 74	Betontemperatur	NiCr/Ni	330, 225, +190
81	144	09:12	BT 71	Betontemperatur	NiCr/Ni	310, 45, +190
82	145	09:13		Microlink Kanal defekt !		
83	146	09:14	BT 73	Betontemperatur	NiCr/Ni	330, 45, +190
84	147	09:15	KT 10	Temp. Gießrinne	W3Re/25	
85	164	10:16	TE-11	TE-Ref. Modul 11	Pt 100	Mainframe
86	165	11:00	BT 76	Betontemperatur[1]	NiCr/Ni	310, 135, +90
87	166	11:01		nicht belegt		
88	167	11:02	BT 78	Betontemperatur[1]	NiCr/Ni	310, 315, +90
89	168	11:03		nicht belegt		
90	169	11:04		nicht belegt		
91	170	11:05	CT 1	GFK-Rohr-Temp. Innen	NiCr/Ni	571, 135
92	171	11:06	CT 2	GFK-Rohr-Temp. Innen	NiCr/Ni	571, 45
93	172	11:07	CT 3	GFK-Rohr-Temp. Innen	NiCr/Ni	571, 315
94	173	11:08	CT 4	GFK-Rohr-Temp. Innen	NiCr/Ni	571, 225
95	174	11:09	BT 87	Betontemperatur	NiCr/Ni	360, 45, +15
96	175	11:10	BT 88	Betontemperatur	NiCr/Ni	360, 135, +15
97	176	11:11	BT 89	Betontemperatur	NiCr/Ni	360, 225, +15

---

[1] BT 76 and BT 78 use Pt-Rh-compensating cables. This may result in a small error in the temperature

98	177	11:12	BT 90	Betontemperatur	NiCr/Ni	360, 315, +15
99	178	11:13	KM 1	Einguss - Masse	Waage	Reaktionstiegel
100	179	11:14	BT 77	Betontemperatur	NiCr/Ni	310, 225, +90
101	180	11:15	BT 80	Betontemperatur	NiCr/Ni	330, 225, +90
102	197	12:16	TE-13	TE-Ref. Modul 13	Pt 100	Mainframe
103	16	02:00	BT 83	Betontemperatur	NiCr/Ni	310, 225, +15
104	17	02:01	BT 84	Betontemperatur	NiCr/Ni	310, 315, +15
105	18	02:02	BT 75	Betontemperatur	NiCr/Ni	310, 45, +90
106	19	02:03	BT 86	Betontemperatur	NiCr/Ni	330, 225, +15
107	20	02:04	BT 79	Betontemperatur	NiCr/Ni	330, 45, +90
108	21	02:05	BT 81	Betontemperatur	NiCr/Ni	310, 45, +15
109	22	02:06	WP 10	Wasserdruck	DMS	Tiegel-SW
110	23	02:07	BT 82	Betontemperatur	NiCr/Ni	310, 135, +15
111	24	02:08	WP 15	Wasserdruck	DMS	W-Zulauf
112	25	02:09	HP 1	Hauben-Druck	DMS	0 - 2 bar absolut
113	26	02:10	HP 2	Hauben Druck	DMS	0 - 10 bar diff.
114	27	02:11	BT 85	Betontemperatur	NiCr/Ni	330, 45, +15
115	28	02:12	AR 1	Frequenz	AEG 13	1,2,W+X
116	29	02:13	AN 3	Leistung Umrichter 3	AEG 5	1,2,C+D
117	30	02:14	AN 4	Leistung Umrichter 4	AEG 7	1,2,H+I
118	31	02:15	AU 2	Anl. Spannung 3000 V	AEG 10	1,2,P+R
119	49	04:00				
120	50	04:01				
122	52	04:03				
123	53	04:04	GC 11	Gas-M., INR 1	Q 100-1	
124	54	04:05	GC 12	Gas-M., INR 2	Q 100-1	
125	55	04:06	GC 13	Gas-M., INR 3	Q 100-1	
126	56	04:07	GC 14	Gas-M., INR 4	Q 100-1	
127	57	04:08	GC 15	Gas-M., INR 5	Q 100-1	
128	58	04:09	GC 16	Gas-M., INR 6	Q 100-1	
129	59	04:10	GC 17	Gas-M., INR 7	Q 100-1	
130	60	04:11	GC 18	Gas-M., INR 8	Q 100-1	
131	61	04:12	GX 1	Empf., INR 9	Q 100-1	
132	62	04:13	GC 10	Gas-Scan, INR 10	Q 100-1	

133	63	04:14	GC 21	Gas-M., INR 11	Q 100-2	
134	64	04:15				
135	82	06:00	GC 22	Gas-M., INR 12	Q 100-2	
136	83	06:01	GC 23	Gas-M., INR 13	Q 100-2	
137	84	06:02	GC 24	Gas-M., INR 14	Q 100-2	
138	85	06:03	GC 25	Gas-M., INR 15	Q 100-2	
139	86	06:04	GC 26	Gas-M., INR 16	Q 100-2	
140	87	06:05	GC 27	Gas-M., INR 17	Q 100-2	
141	88	06:06	GC 28	Gas-M., INR 18	Q 100-2	
142	89	06:07	GX 2	Empfindl., INR 19	Q 100-2	
143	90	06:08		Ind. -Bruttoleistung		Intern berechnet
144	91	06:09	SN 1	Ind. -Nettoleistung		Intern berechnet
145	92	06:10	AU 2	Ind. -Spannung		Intern berechnet
146	93	06:11	AR 1	Ind. -Frequenz		Intern berechnet
147	94	06:12				
148	95	06:13	AA 3	Strom Umrichter 3	AEG 14	1,2,F,E
149	96	06:14				
150	97	06:15				
151	115	08:00	AA 4	Strom Umrichter 4	AEG 8	1,2,K+L
152	116	08:01	AU 1	Umr. Spannung 1000 V	AEG 9	1,2,M+N
153	117	08:02				
154	118	08:03	AA 5	Kond. Teilstrom A	AEG 11	1,2,S+T
155	119	08:04	AA 6	Kond. Teilstrom B	AEG 12	1,2,U+V
156	120	08:05				
157	121	08:06	RF 1	Rückkühlanlage	Wirbelm.	Durchfluß
158	122	08:07				
159	123	08:08				
160	124	08:09		GQ 22	Hygrom. 2	
161	125	08:10		GT 22	Hygrom. 2	
162	126	08:11	GF 1	Gasvolumen	Flügelrad	
163	127	08:12	GP 1	Gasdruck	DMS	bei Meßdüse
164	128	08:13	RQ 1	Leistung Rückkühl-Anl.	RF1,Pt100	Rückkühlanlage
165	129	08:14	SN 3	Pultanzeige Nettoleistg.		Nettoleistung
166	130	08:15				

167	148	10:00	AP 1	Ar-Druck	DMS	Haube ein
168	149	10:01	AP 2	Ar-Druck	DMS	Ar-Batterie
169	150	10:02	AP 3	Ar-Druck	DMS	Periskop Kühlg.
170	151	10:03	AF 1	Ar-Strom	RotaM ?	Haube ein
171	152	10:04	AF 2	Ar-Strom	Meßblende	Periskop Freibl.
172	153	10:05		GQ 21	Hygrom. 1	
173	154	10:06		GT 21	Hygrom. 1	
174	155	10:07				
175	156	10:08				
176	157	10:09	HP 3	Hauben-Druck	DMS	0 - 100 bar diff.
177	158	10:10	AF 4	Ar-Strom	Meßblende	Aerosol-Spülung
178	159	10:11	AF 3	Ar-Strom	Meßblende	Periskop Kühlg.
179	160	10:12	AE 1	Ereignis	Logik	Zündg., Abstich
180	161	10:13				
181	162	10:14	CK 1	Zeitmarke	Clock	Synchronisation
182	163	10:15				
183	181	12:00	HT 1	Hauben Temp.	NiCr/Ni	Haubenflansch
184	182	12:01	GT 1	Gastmp. n. Abscheider	NiCr/Ni	n. Abscheider
185	183	12:02	GT 2	Gastemp. b. Meßdüse	NiCr/Ni	bei Meßdüse
186	184	12:03	KT 1	Wandtemp. Absch.	NiCr/Ni	Abscheider
187	185	12:04	KT 2	Wandtemp. b. Meßd.	NiCr/Ni	bei Meßdüse
188	186	12:05	KT 3	Zuluft-Temp.	NiCr/Ni	Lüftg. Mitte
189	187	12:06	KT 4	Hallentemp.	Pt 100	
190	188	12:07				
191	189	12:08				
192	190	12:09	GP 2	Staurohrmessung	Diff. Druck	bei Meßdüse
193	191	12:10	CL 1	Wasserstand Tiegel	Druck	Tiegel-N
194	192	12:11	WF 16	Wasserdurchfluß	magn.-ind.	W-Zulauf
195	193	12:12	WF 17	Wasserd.fl. Notkühlung	magn.-ind.	Tiegelhaube
196	194	12:13	KU 1	Kontr.Spannung	0 mV	
197	195	12:14	KU 2	Kontr.Spannung	40 mV	
198	196	12:15	LV 115	Steuerung WF 15	Ventil 115	W-Zulauf

* Verstärker berücksichtigt bereits Kartentemperatur

Appendix C: Test data

This appendix provides thermocouple plots showing the temperature rise in the concrete and the failure of those thermocouples, which are hit by the eroding melt. The thermocouples are grouped in accordance with the instrumentation lines in Figure 26 in Section 4.3 to show the progression of the melt in the concrete.

For the temperature signals, the following general remarks are essential:

1. Inductive heating of the melt generates a high frequency noise on some of the thermocouple signals, in spite of moderate high frequency signal filtering.
2. Thermocouple failure is typically characterized by a sharp increase of the temperature, up to ~1200°C maximum, followed by a sudden drop of the signal and extreme oscillations of the signal for the further course of the test until end of induction heating. The reason is the open thermocouple junction in contact with the melt. Negative signals are omitted from the plots.
3. After end of induction heating at 1878 s, the noise on most of the thermocouples disappears and the temperature reading is more accurate. Many of the failed thermocouples form new junctions that evidently give valid temperature information as can be seen by their long term temperature measurements in comparison with those thermocouples that were not destroyed. Also, few previously destroyed thermocouples that come into contact with the boiling coolant water, register 100°C (e.g. BT 80 in Figure C- 32).

In addition to the temperatures, Figure C-34 gives the constant argon cover gas that is the reference for mass-spectrometer analysis of gas composition.

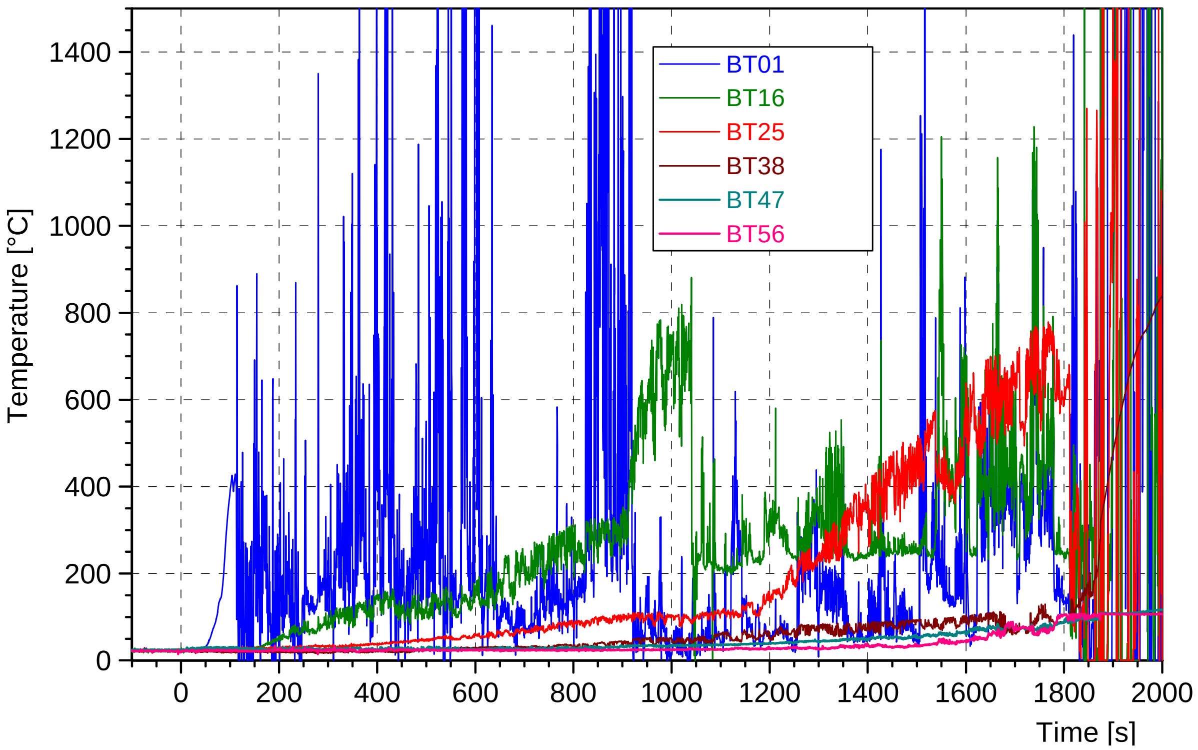

short-term registration

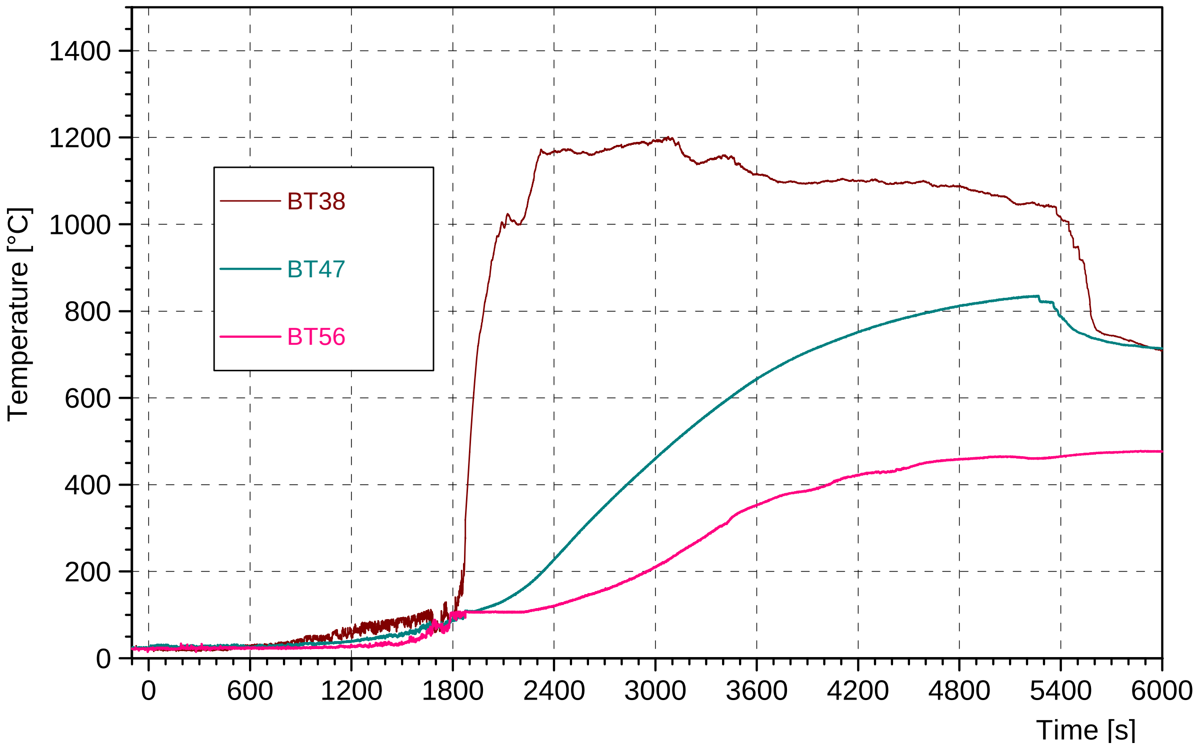

long-term registration

Figure C- 1: T1 | CL - thermocouples on the centre line of the concrete crucible.

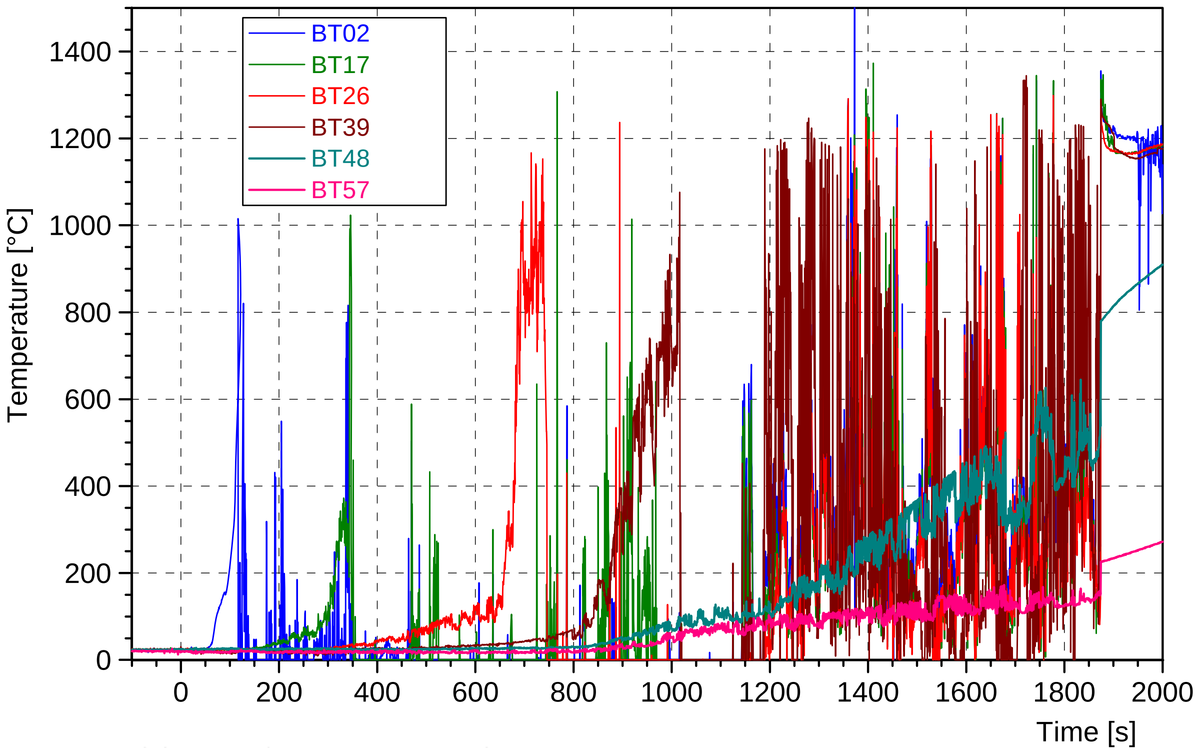

Figure C- 2: T2 | NE - thermocouples in the bottom of the concrete crucible.

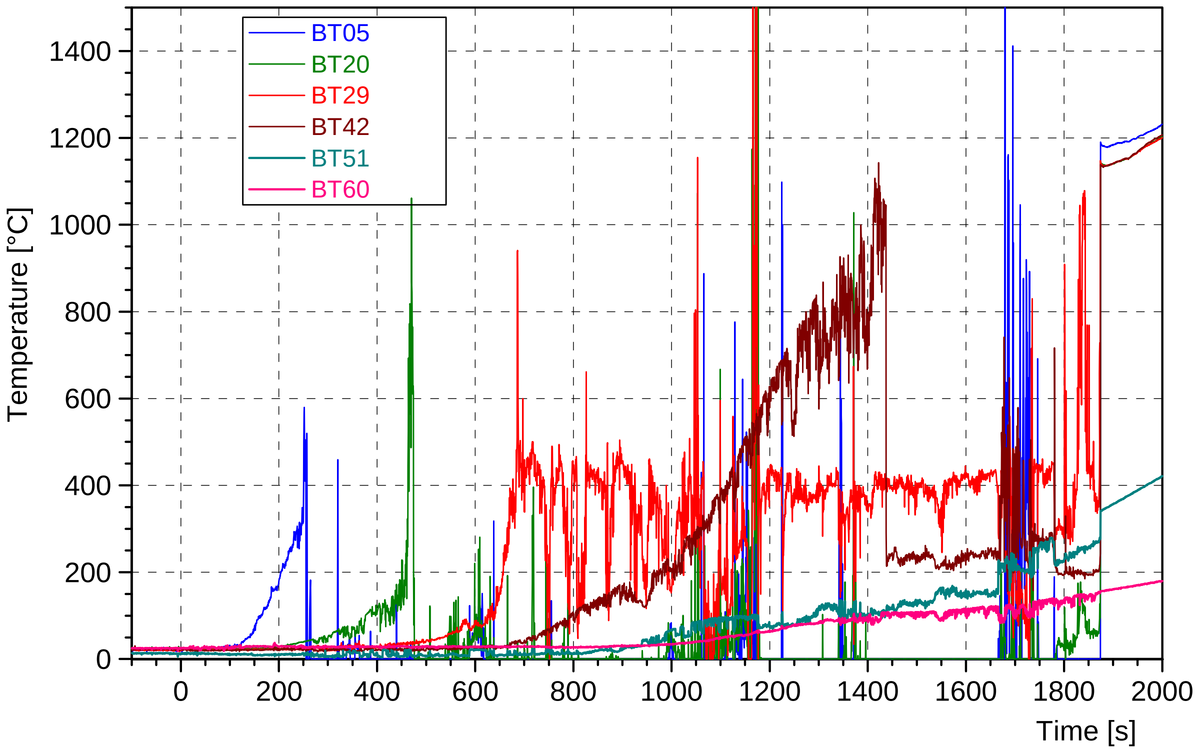

Figure C- 3: T2 | SE - thermocouples in the bottom of the concrete crucible.

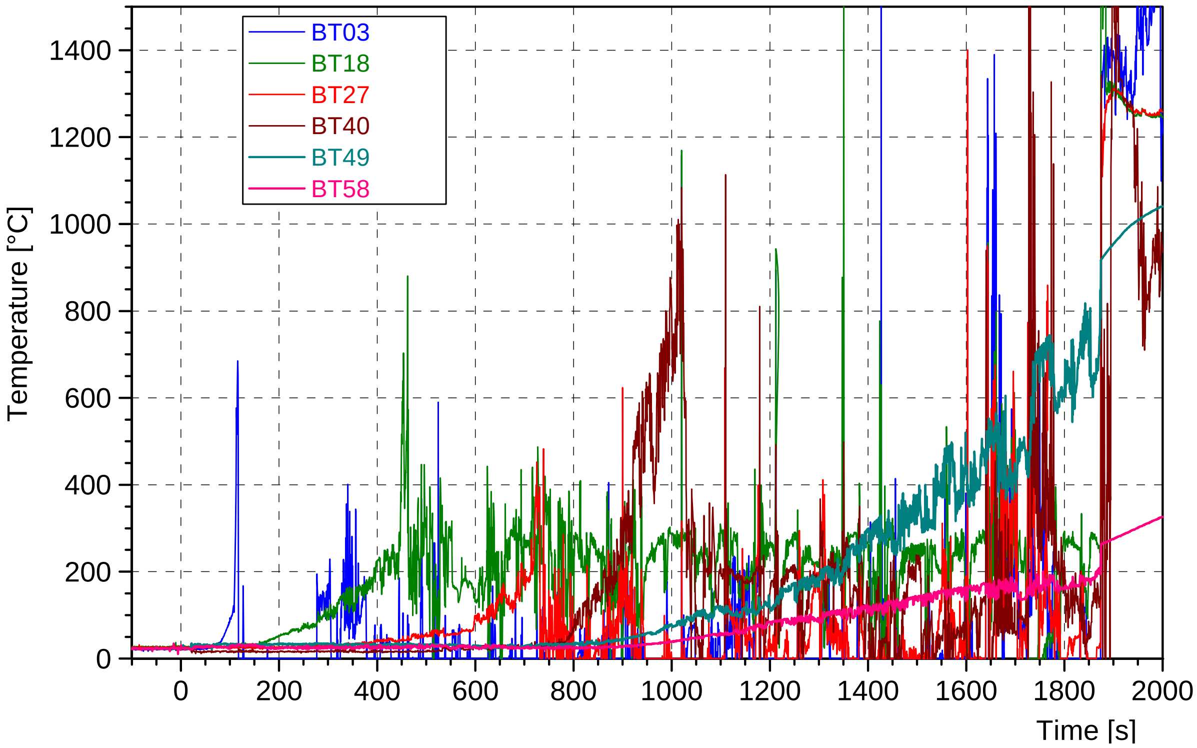

short-term registration

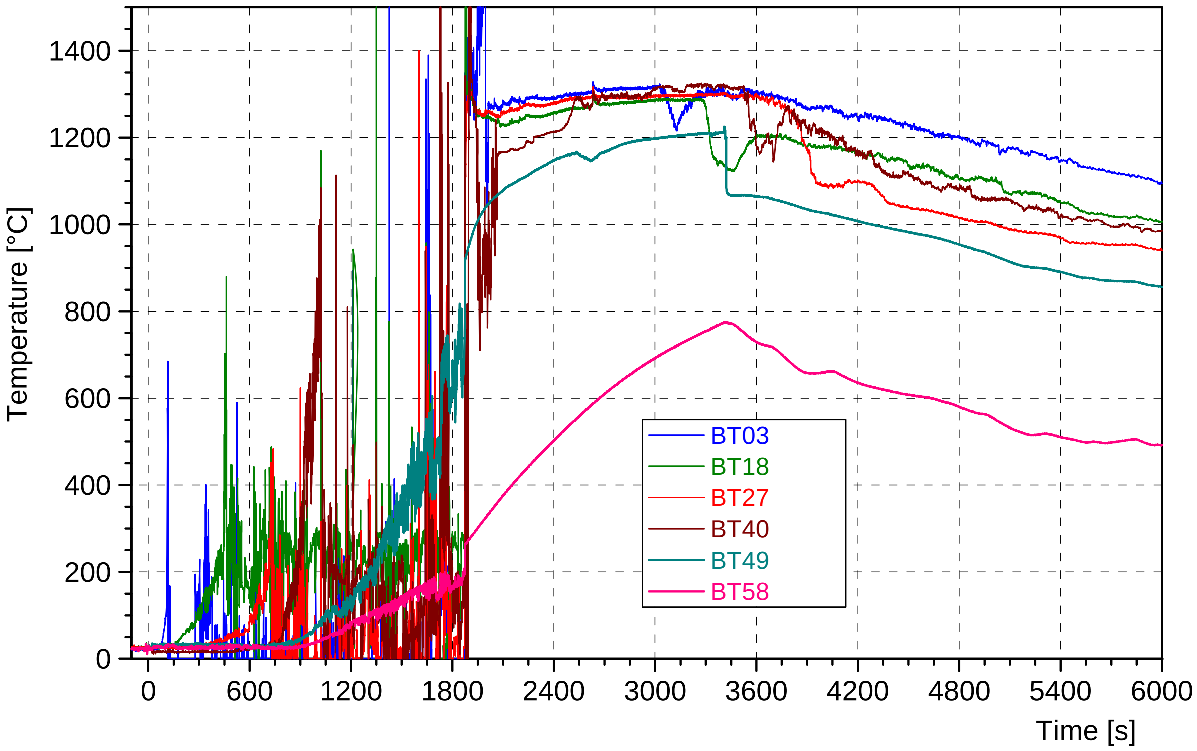

long-term registration

Figure C- 4: T2|NW - thermocouples in the bottom of the concrete crucible.

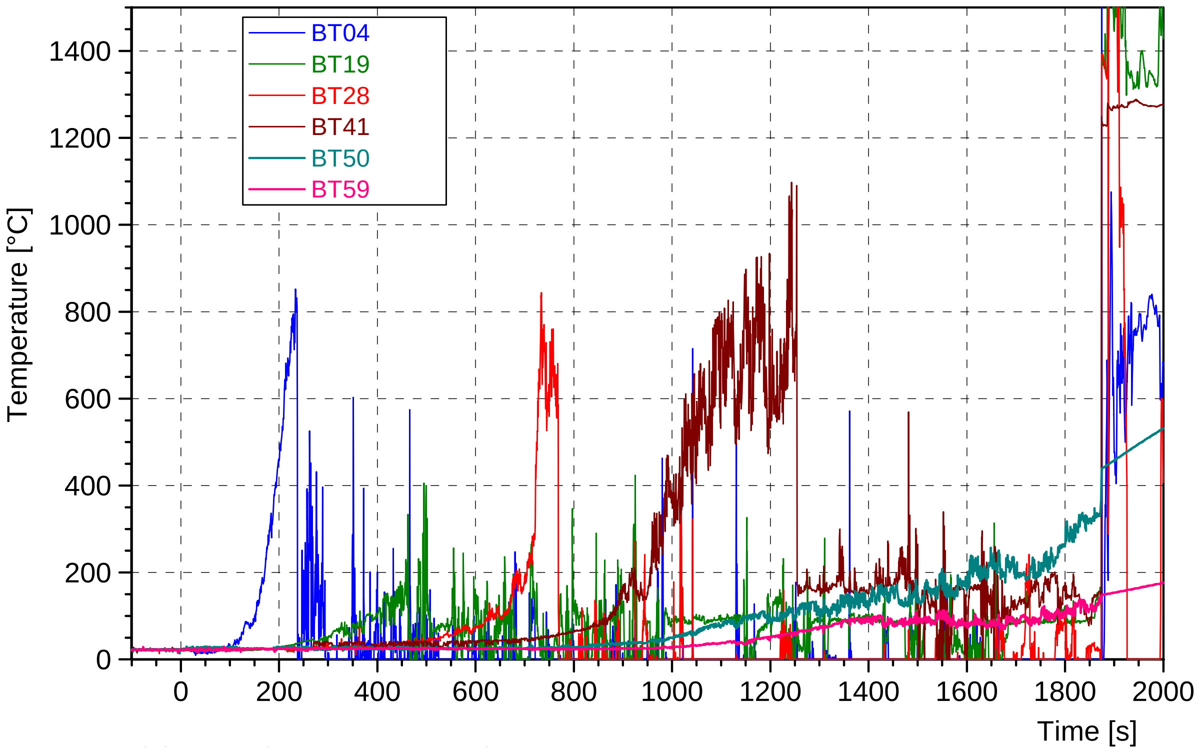

Figure C- 5: T2 | SW - thermocouples in the bottom of the concrete crucible

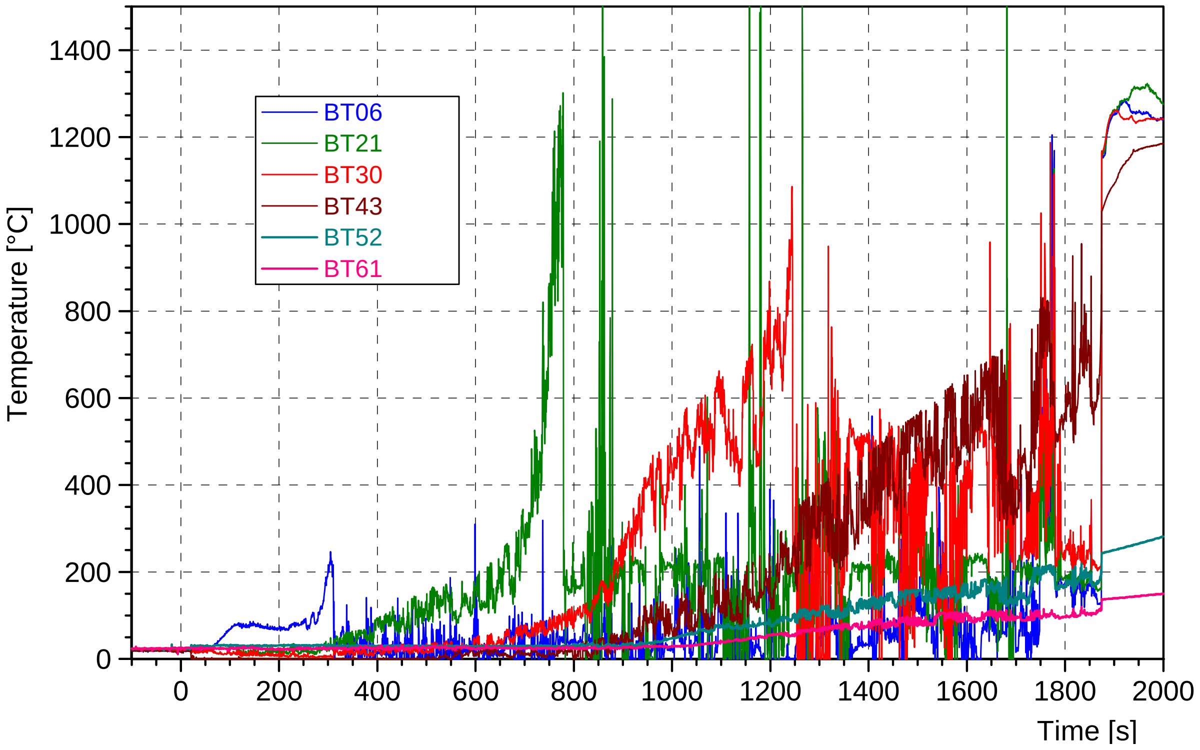

Figure C- 6: T3 | NE - thermocouples in the bottom of the concrete crucible

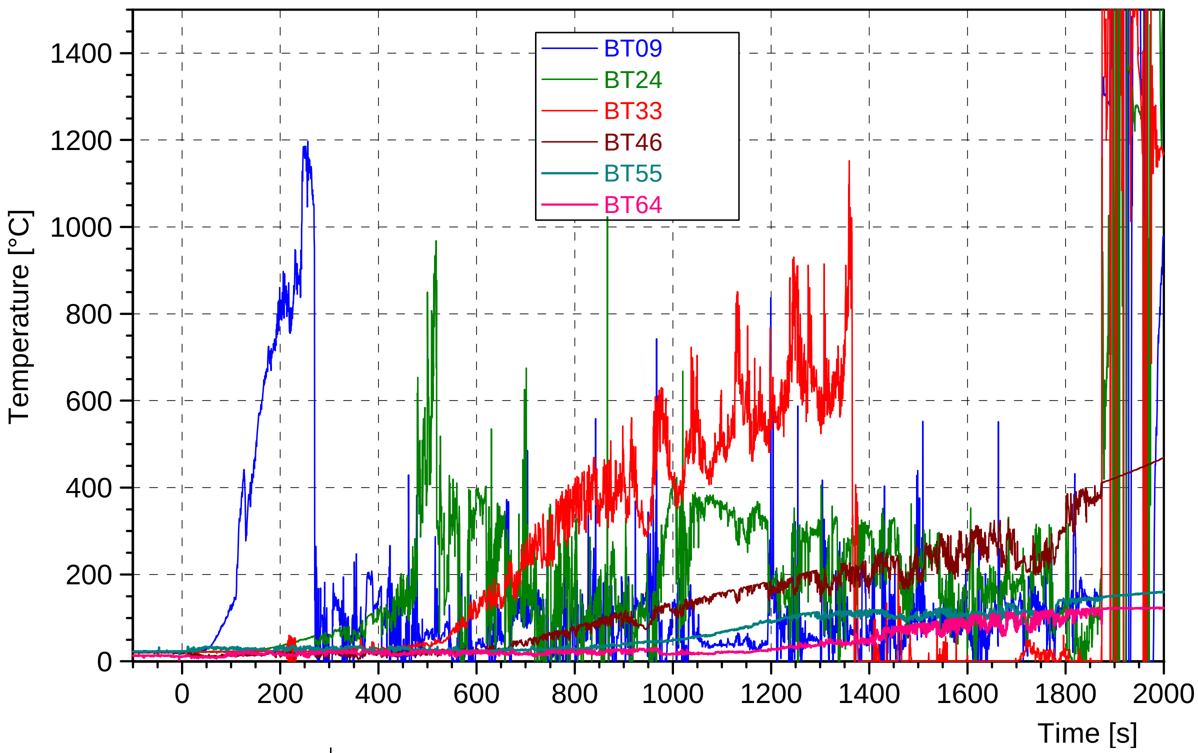

Figure C- 7: T3│SE - thermocouples in the bottom of the concrete crucible

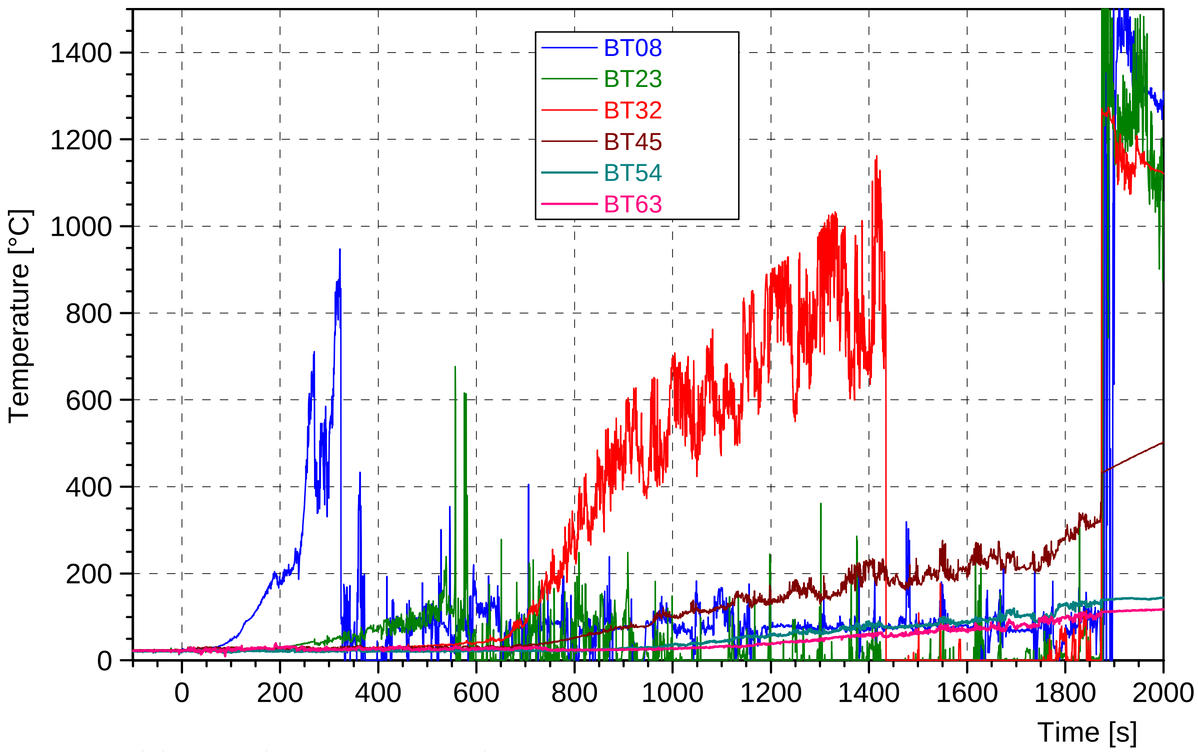

Figure C- 8: T3│SW - thermocouples in the bottom of the concrete crucible

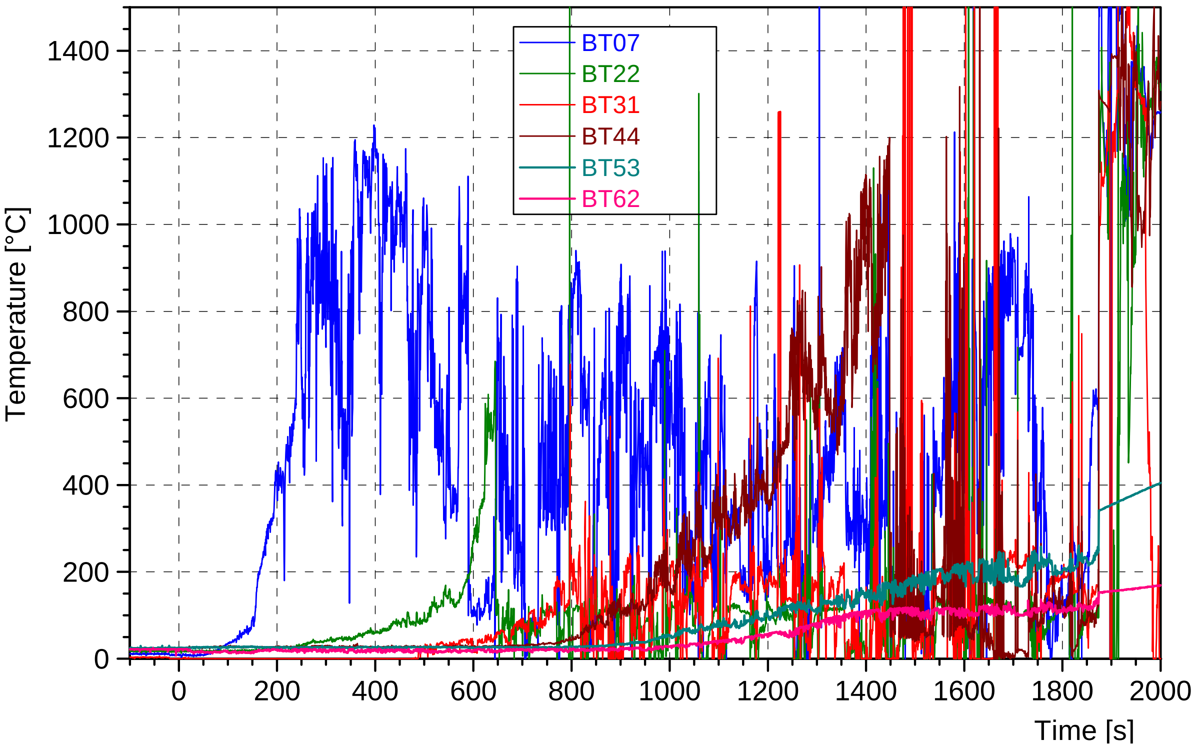

short-term registration

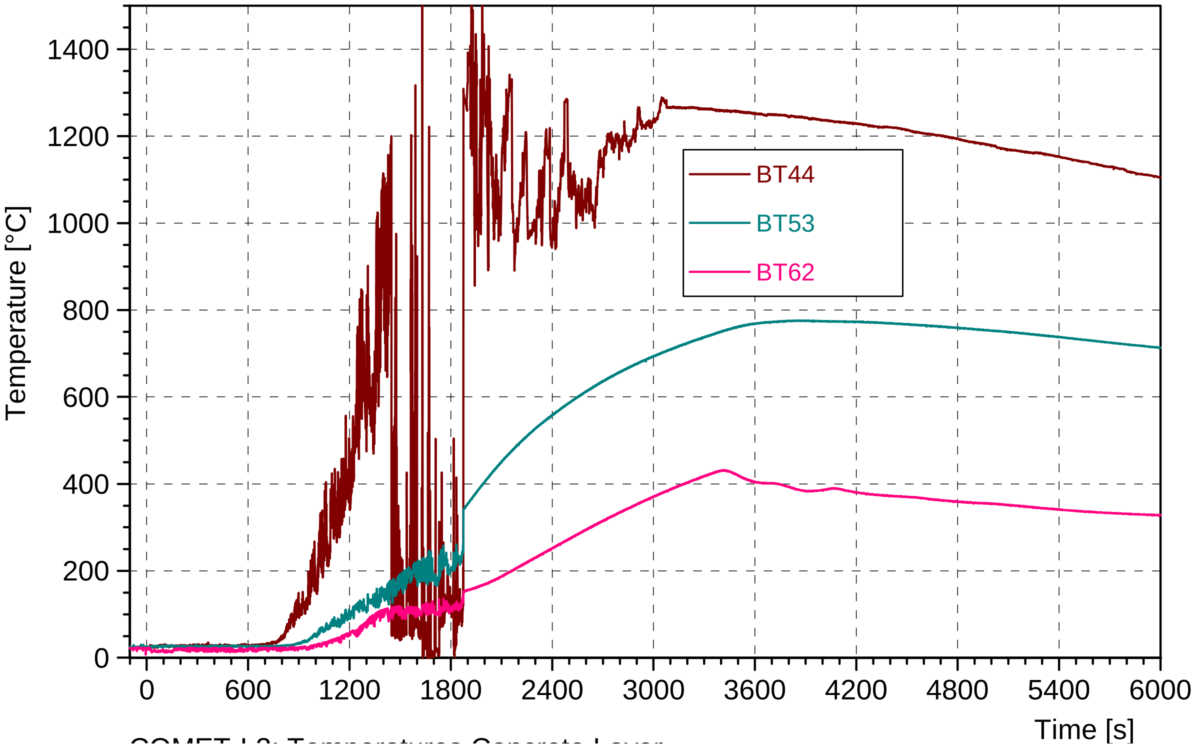

long-term registration

Figure C- 9: T3│NW - thermocouples in the bottom of the concrete crucible

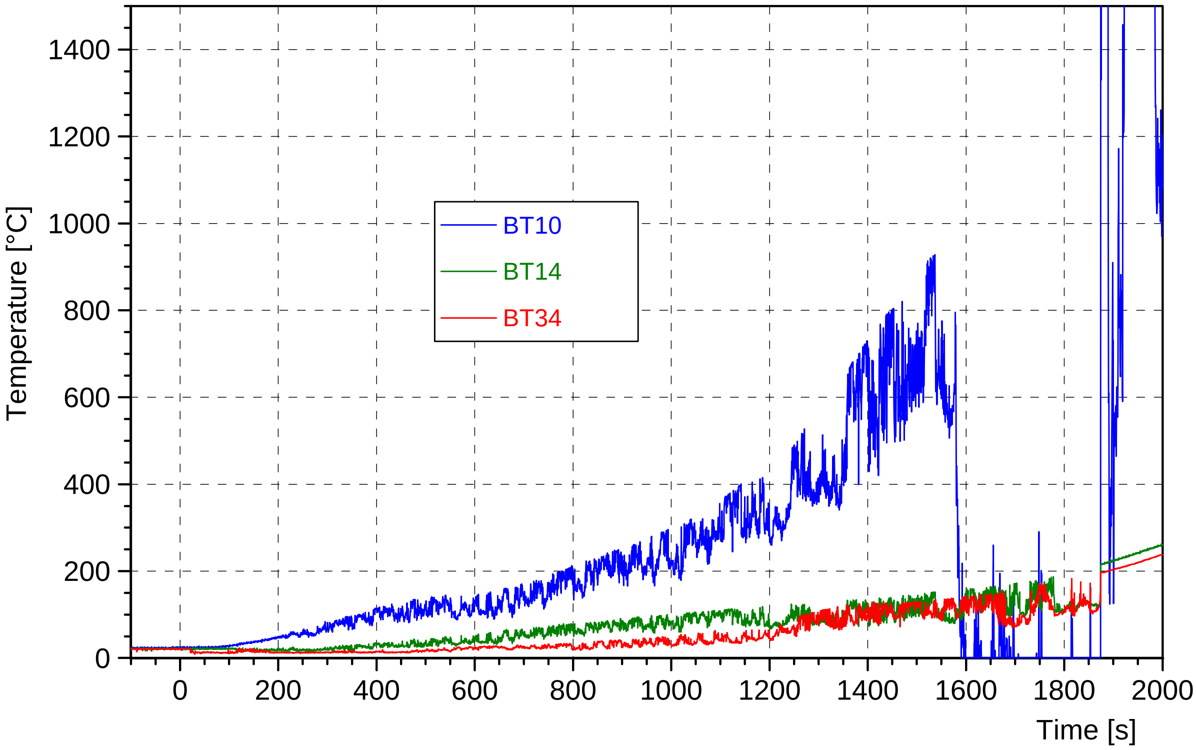

Figure C- 10: Thermocouples BT10, BT14, and BT34 in the outer position of the lower crucible, section NE

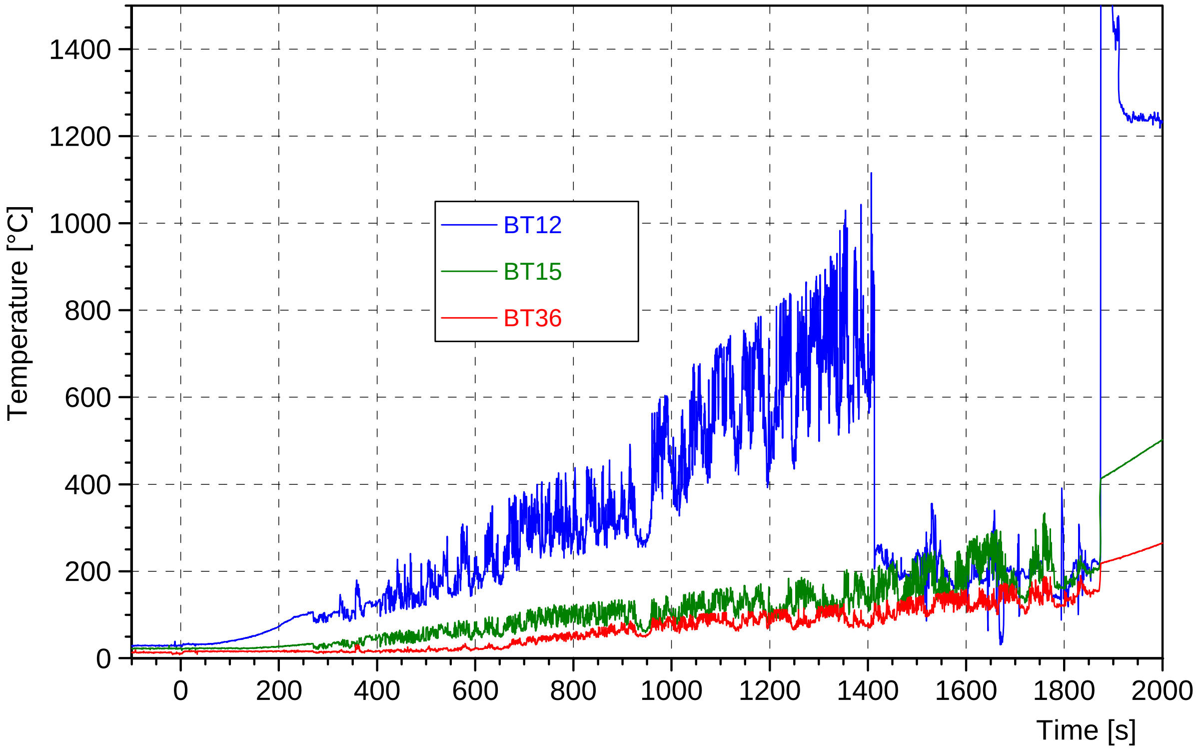

Figure C- 11: Thermocouples BT12, BT15, and BT36 in the outer position of the lower crucible, section SW

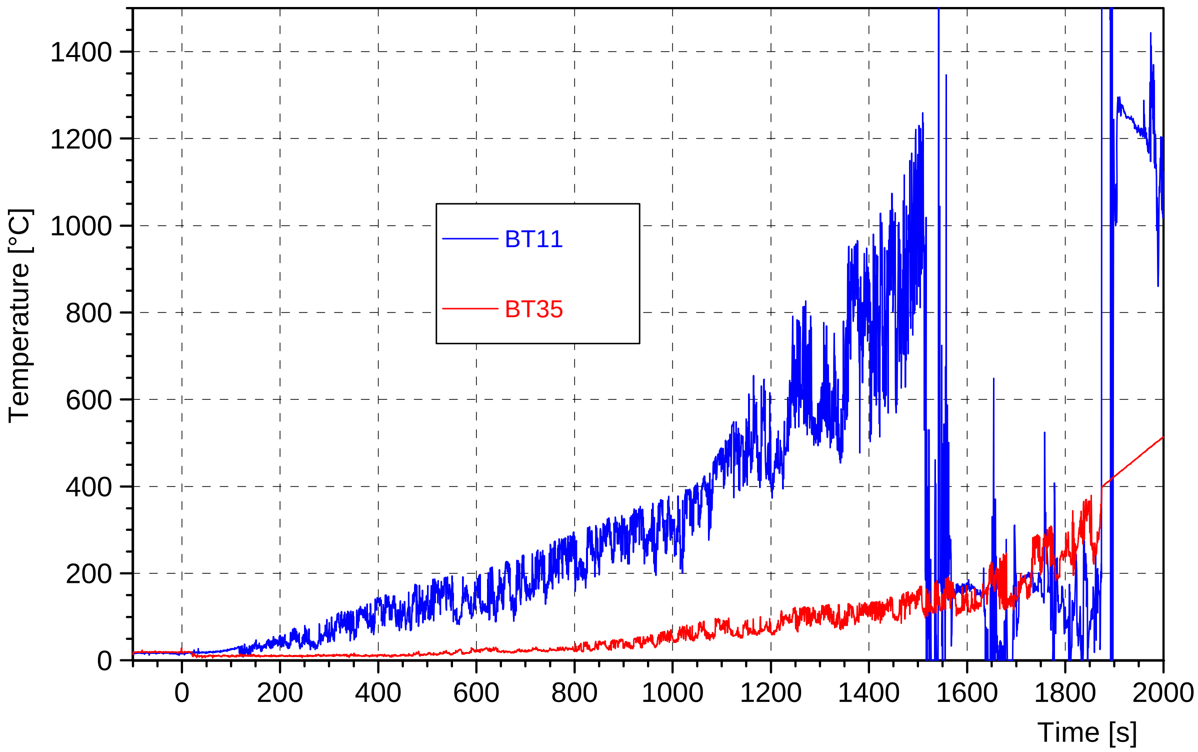

short-term registration

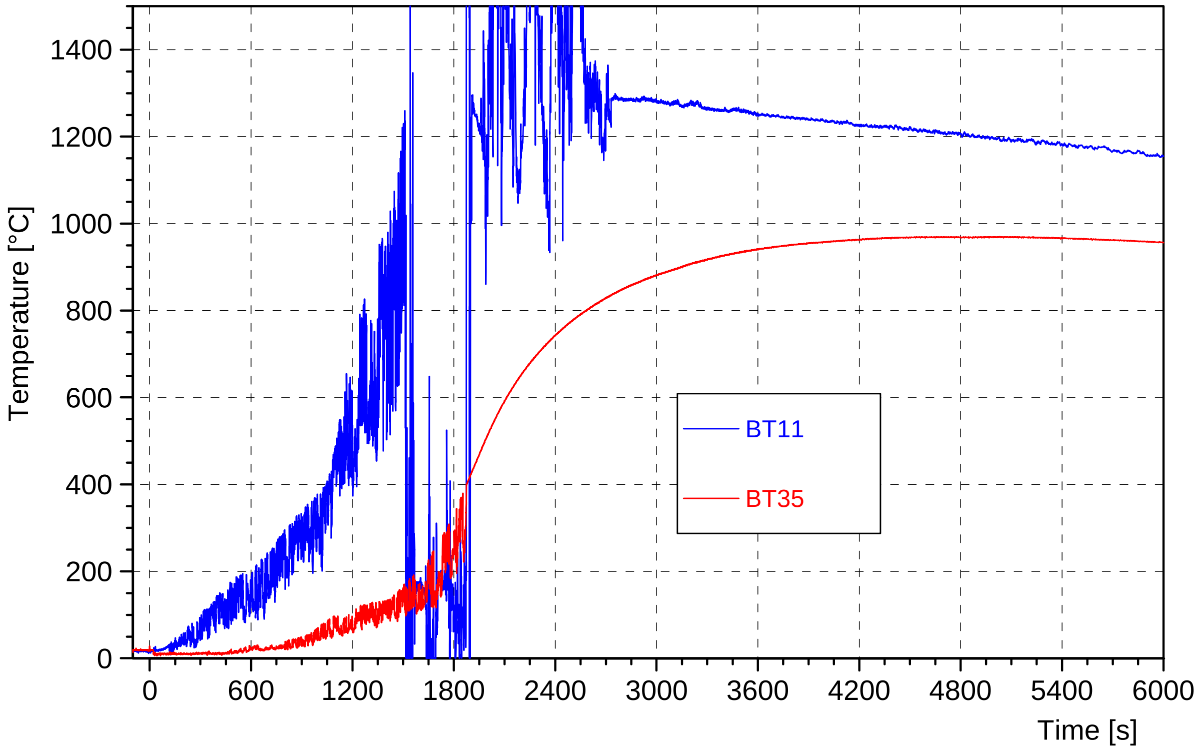

long-term registration

Figure C- 12: T4 | NW- thermocouples in the bottom of the concrete crucible

Thermocouples BT11 and BT35 in the outer position of the lower crucible, section NW

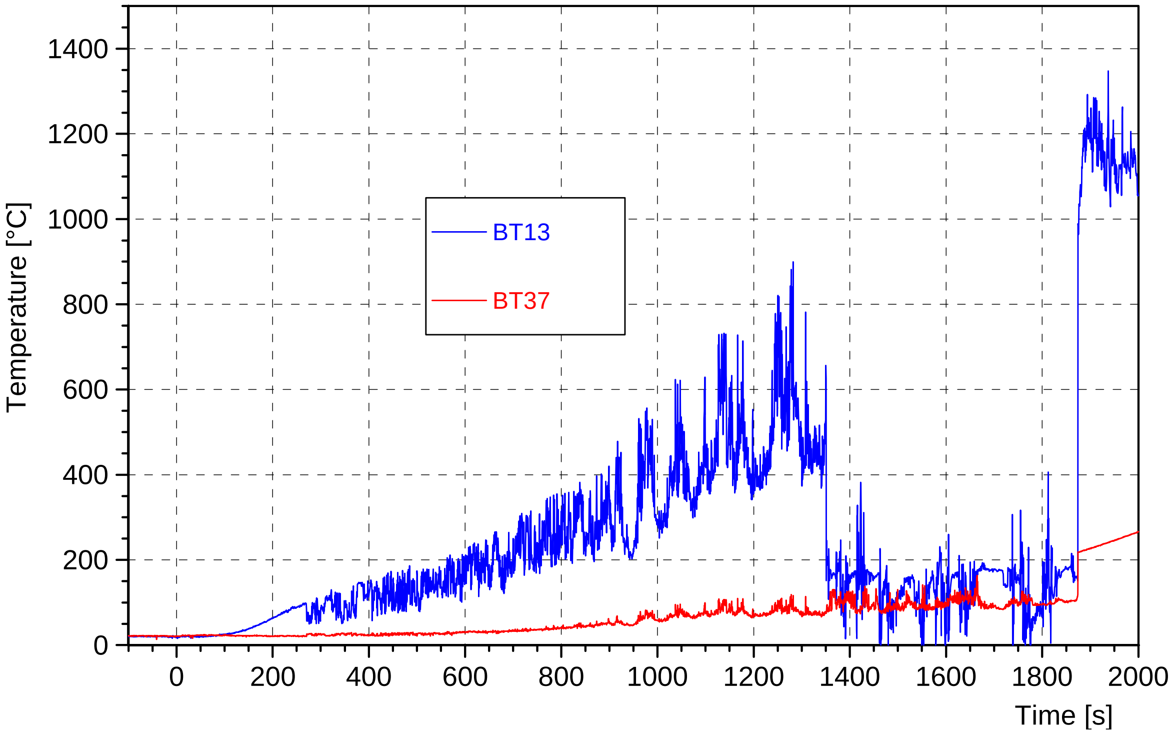

Figure C- 13: T4│SE- thermocouples in the bottom of the concrete crucible

Thermocouples BT13 and BT37 in the outer position of the lower crucible, section SE

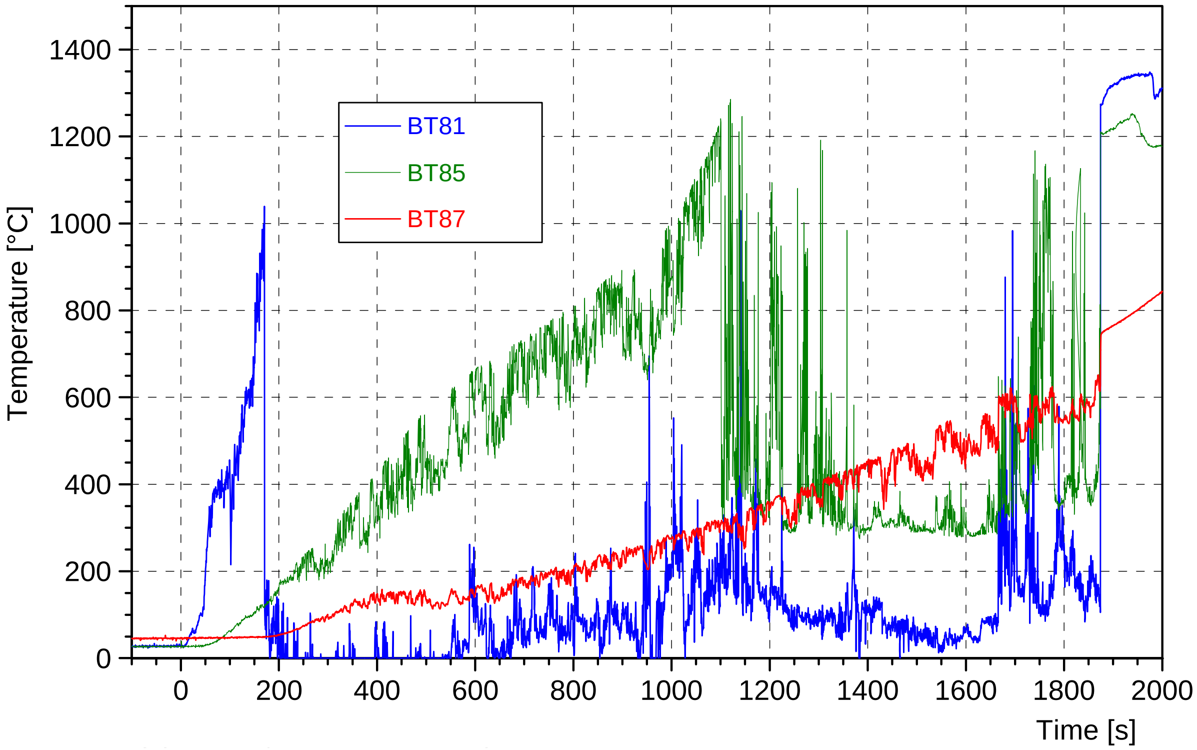

short-term registration

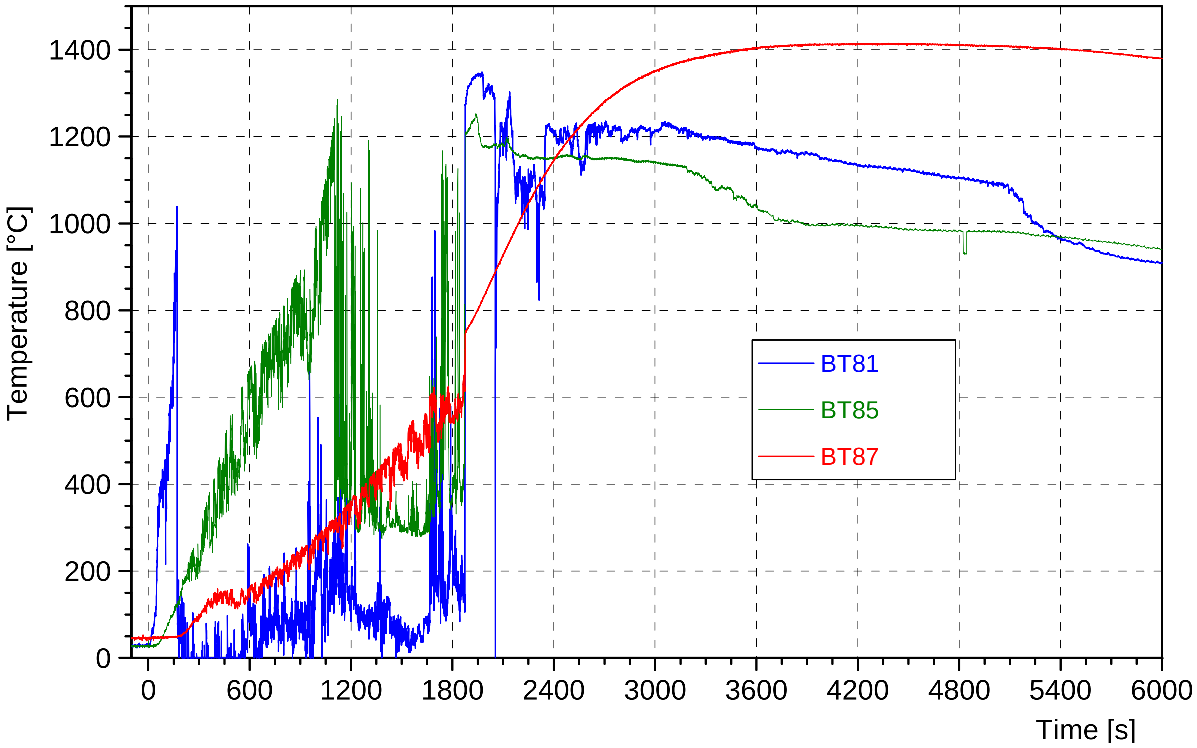

long-term registration

Figure C- 14: T5 | NE- thermocouples in the side wall of the concrete crucible

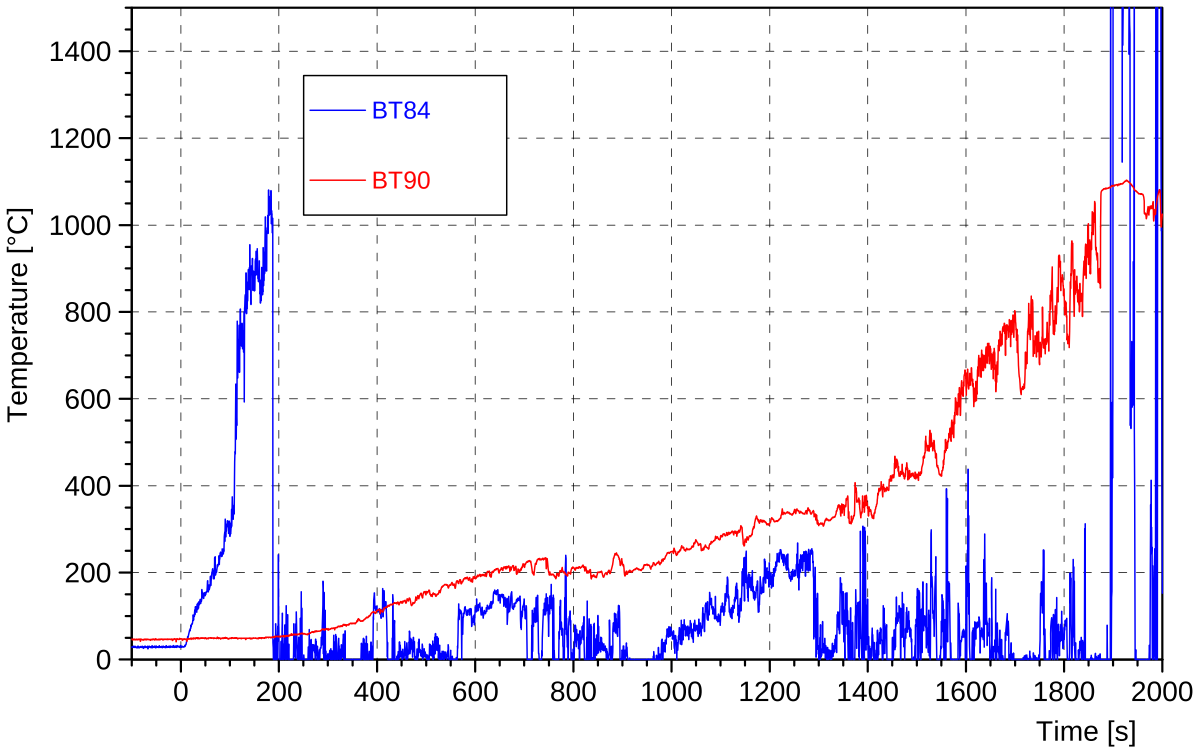

short-term registration

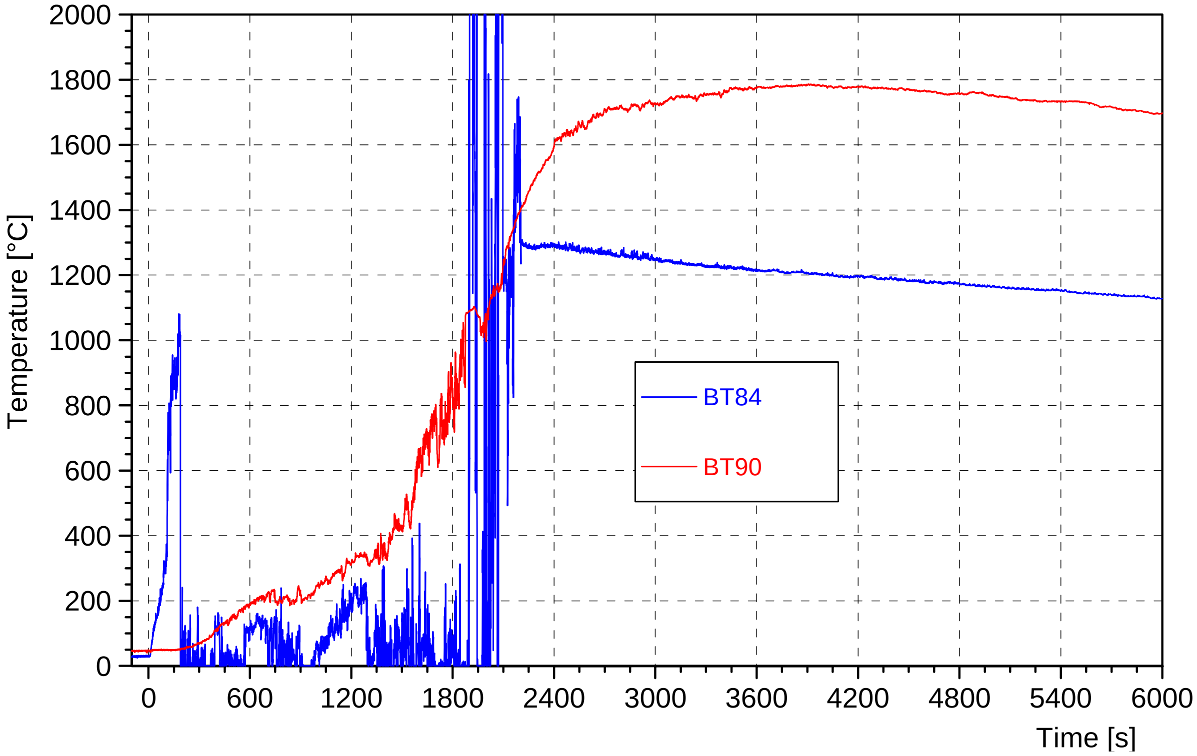

long-term registration

Figure C- 15: T5│SE- thermocouples in the side wall of the concrete crucible

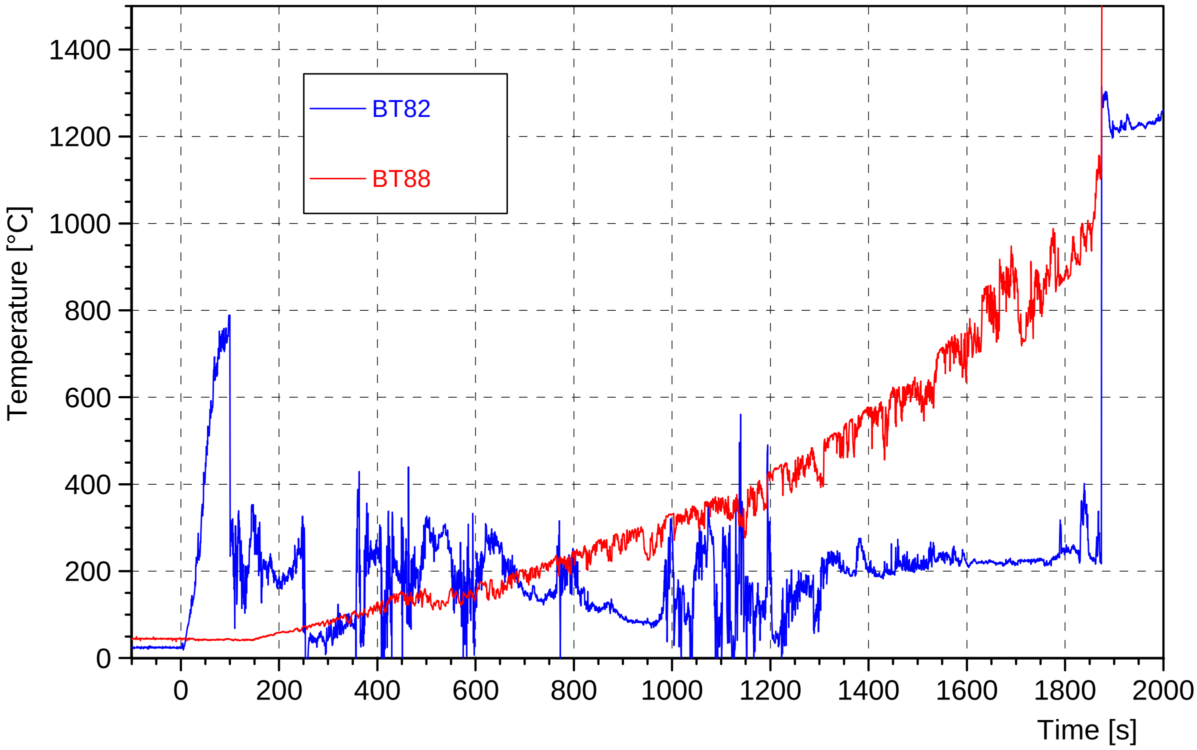

short-term registration

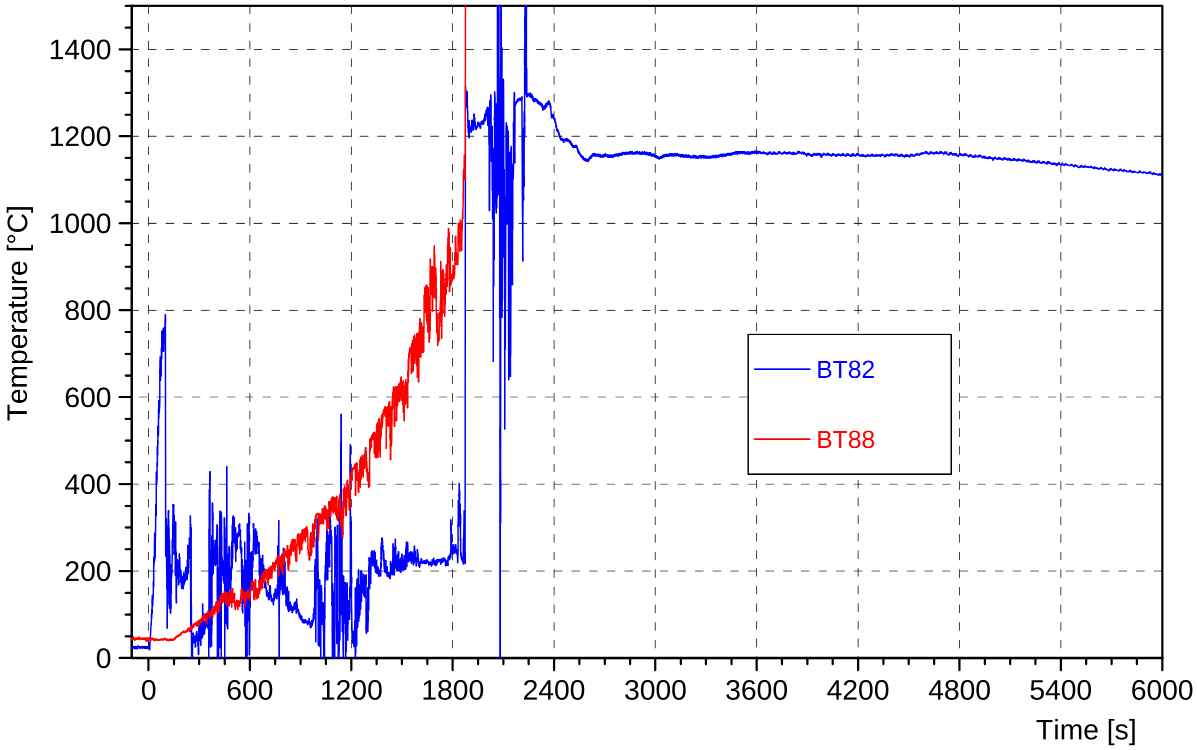

long-term registration

Figure C- 16: T5│NW- thermocouples in the side wall of the concrete crucible

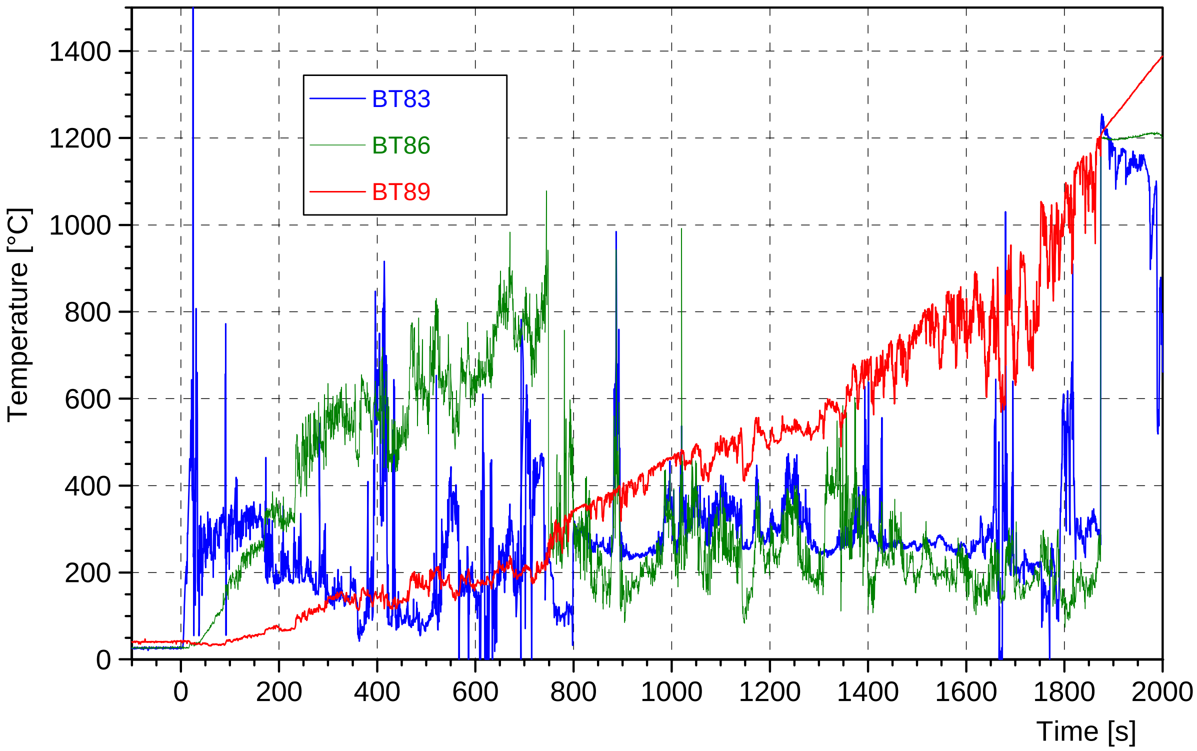

short-term registration

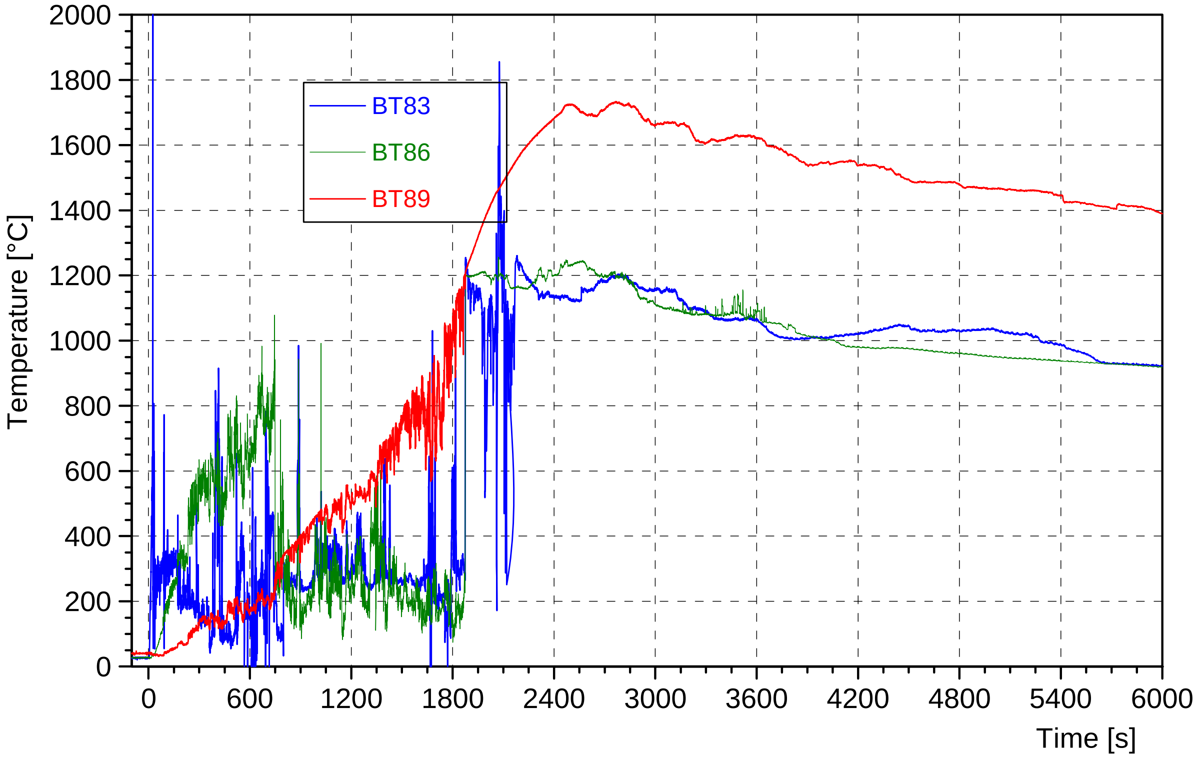

long-term registration

Figure C- 17: T5 | SW- thermocouples in the side wall of the concrete crucible

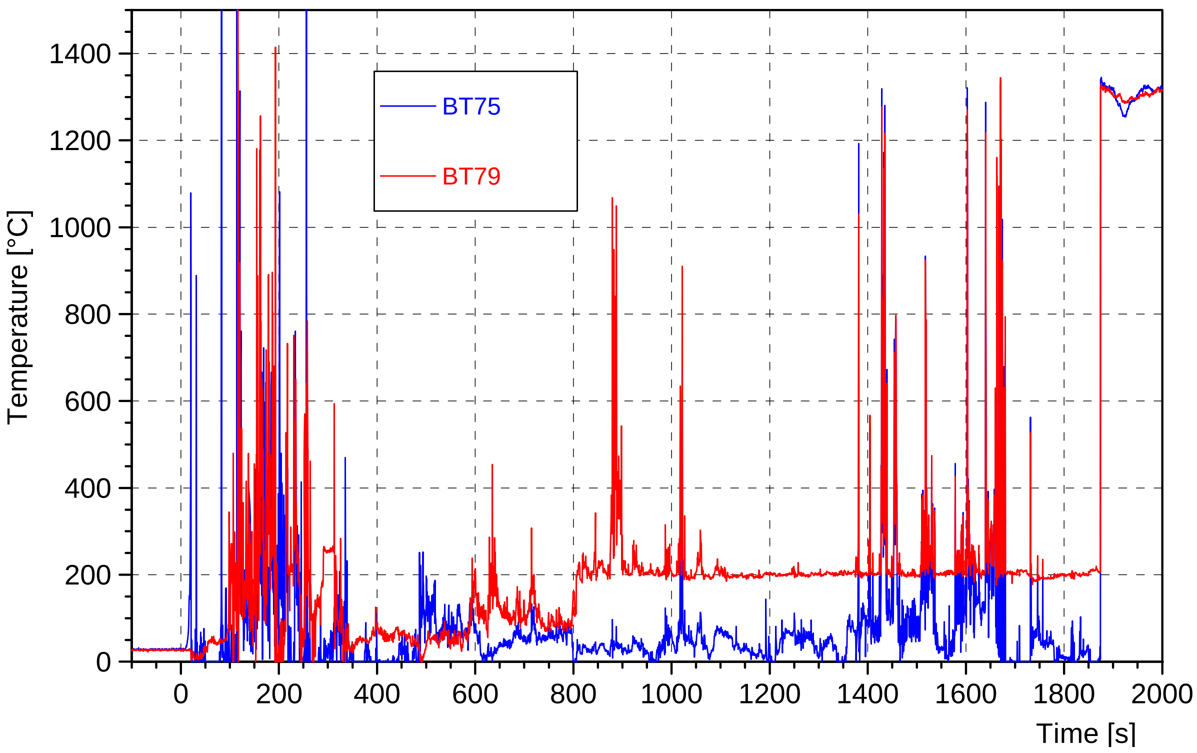

Figure C- 18: T6 | NE- thermocouples in the side wall of the concrete crucible

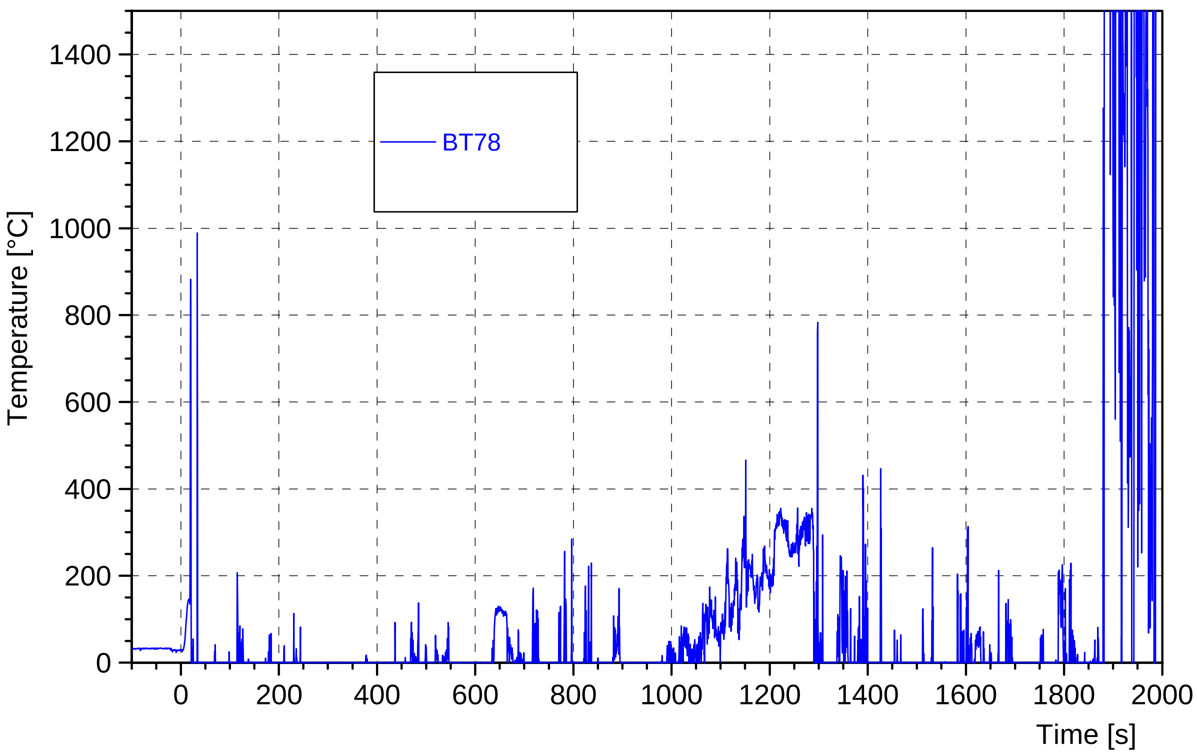

Figure C- 19: T6 | SE- thermocouple in the side wall of the concrete crucible

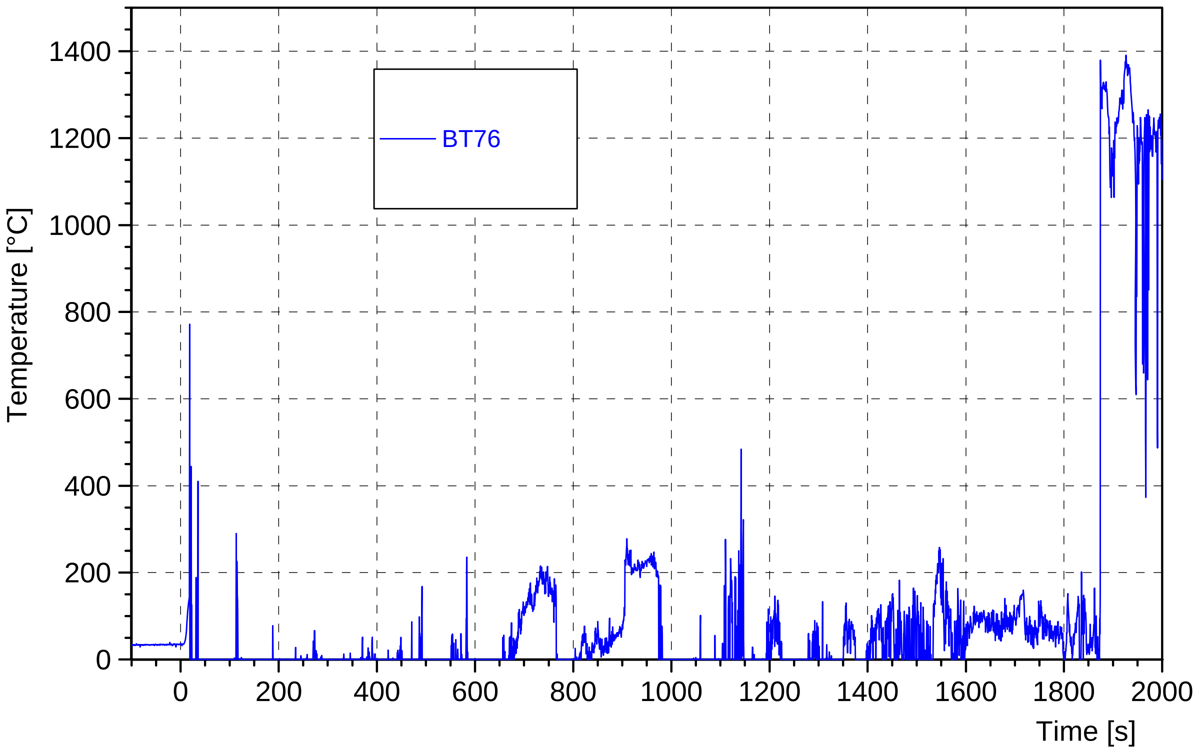

Figure C- 20: T6│NW- thermocouple in the side wall of the concrete crucible

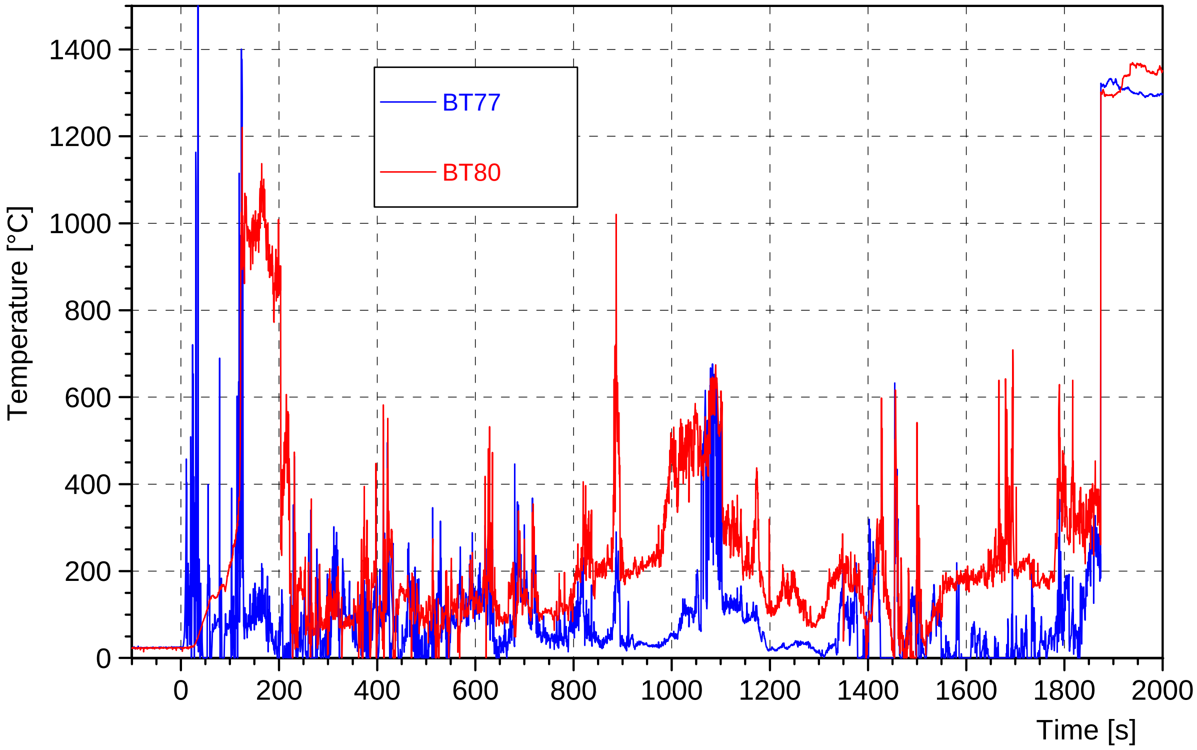

Figure C- 21: T6│SW- thermocouples in the side wall of the concrete crucible

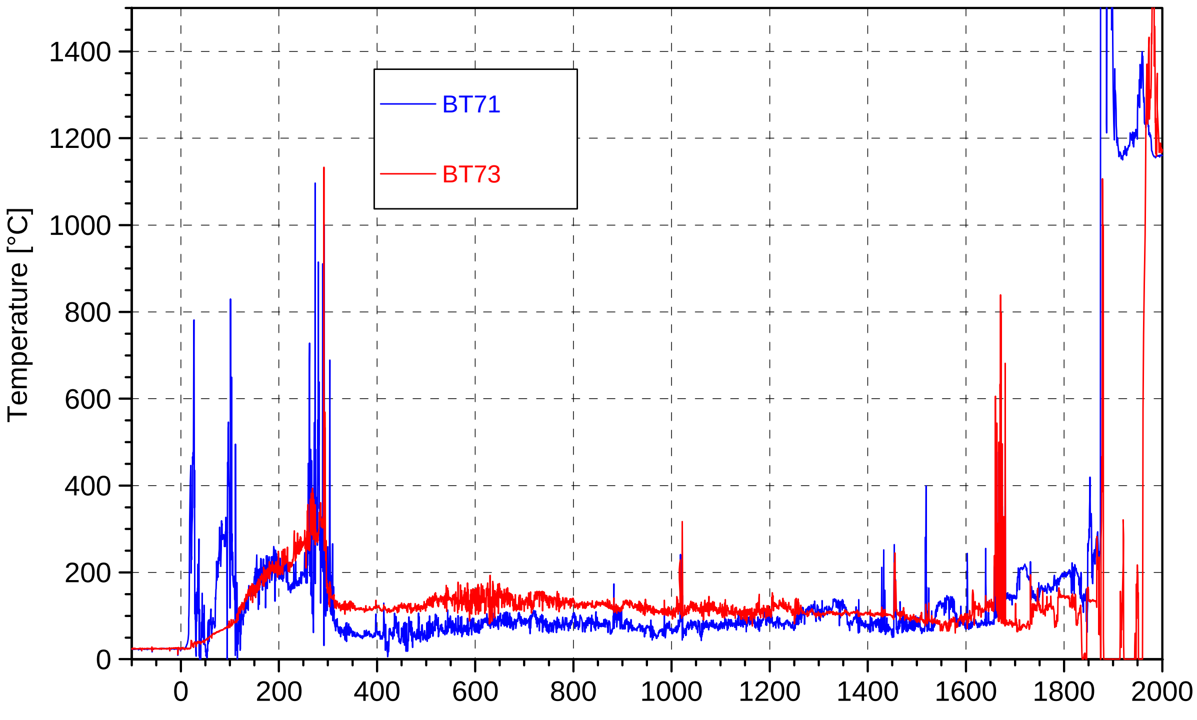

short-term registration

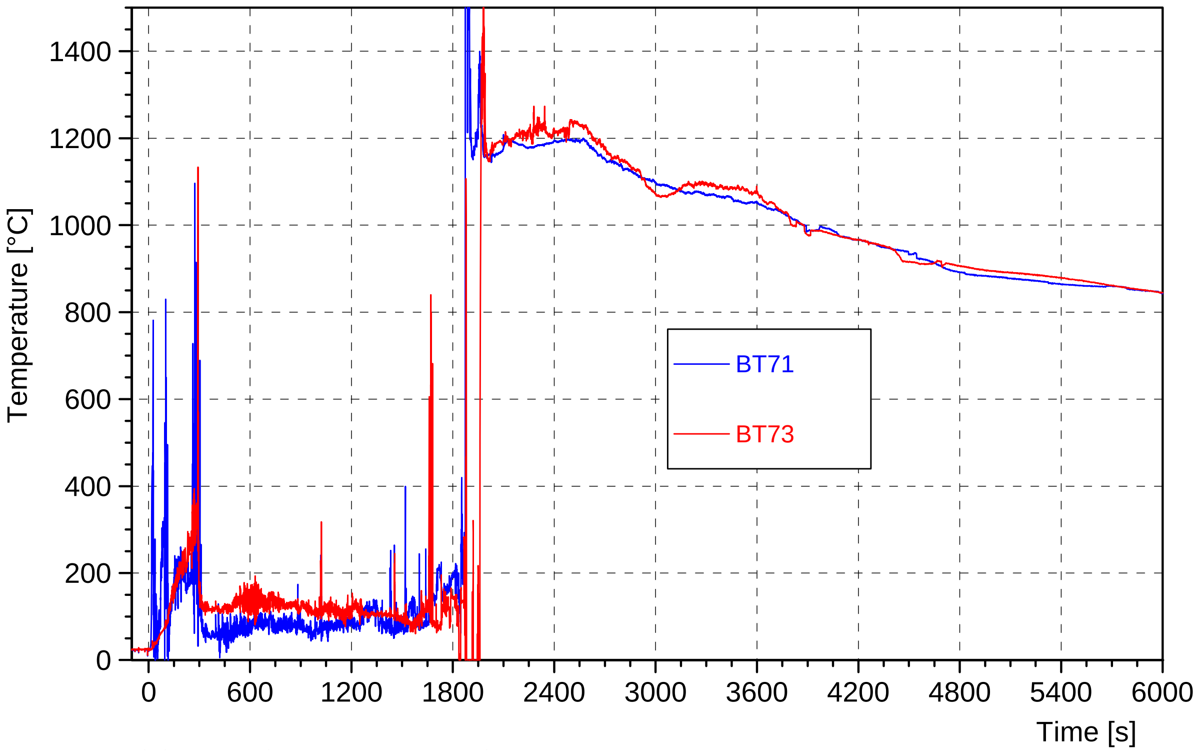

long-term registration

Figure C- 22: T7 | NE- thermocouples in the side wall of the concrete crucible

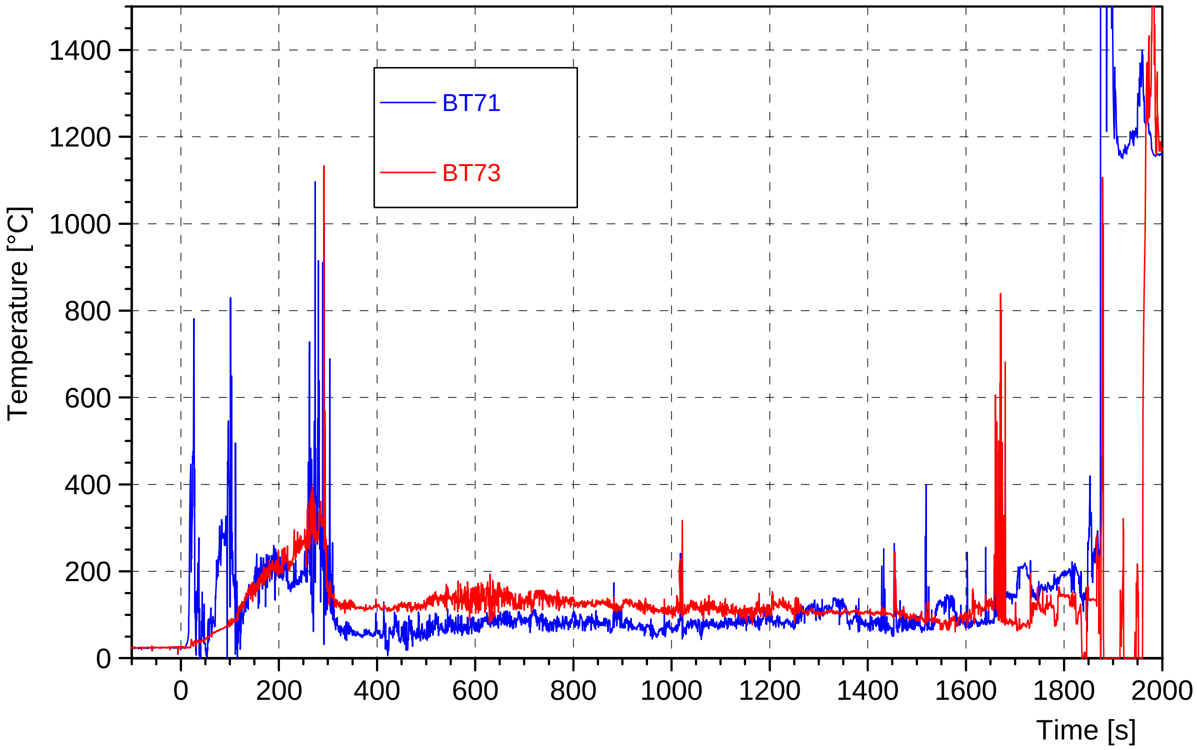

short-term registration

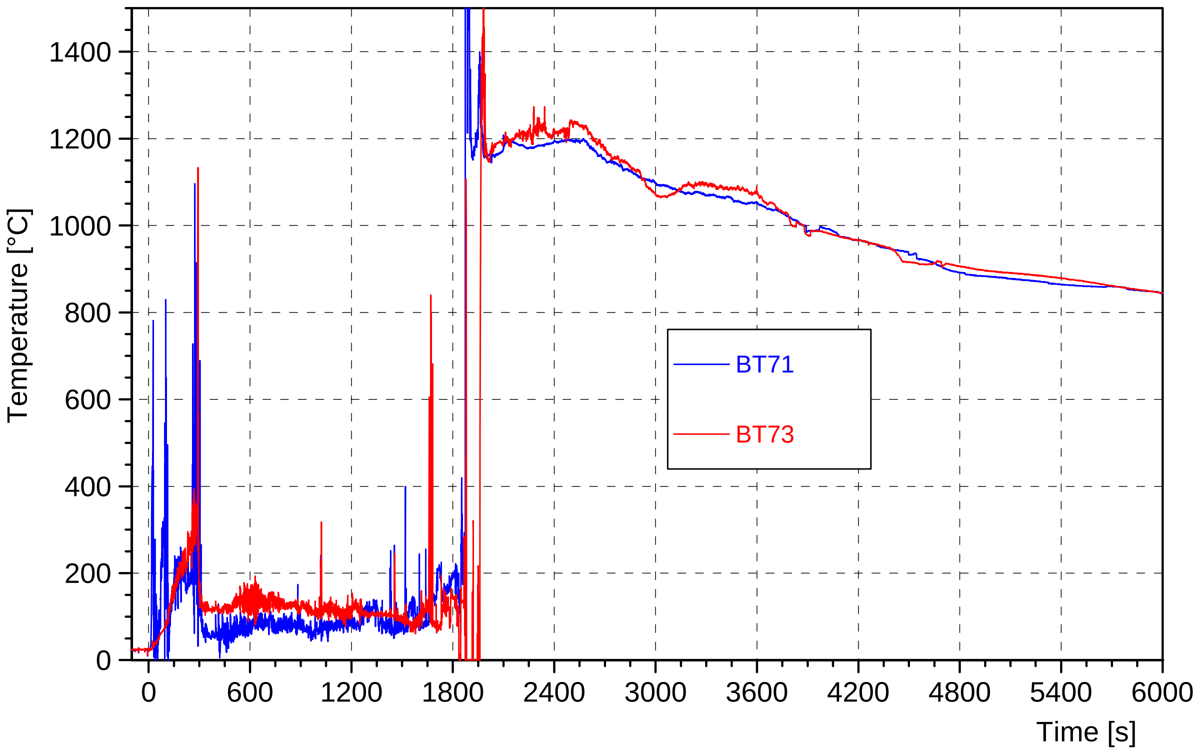

long-term registration

Figure C- 23: T7 | SW- thermocouples in the side wall of the concrete crucible

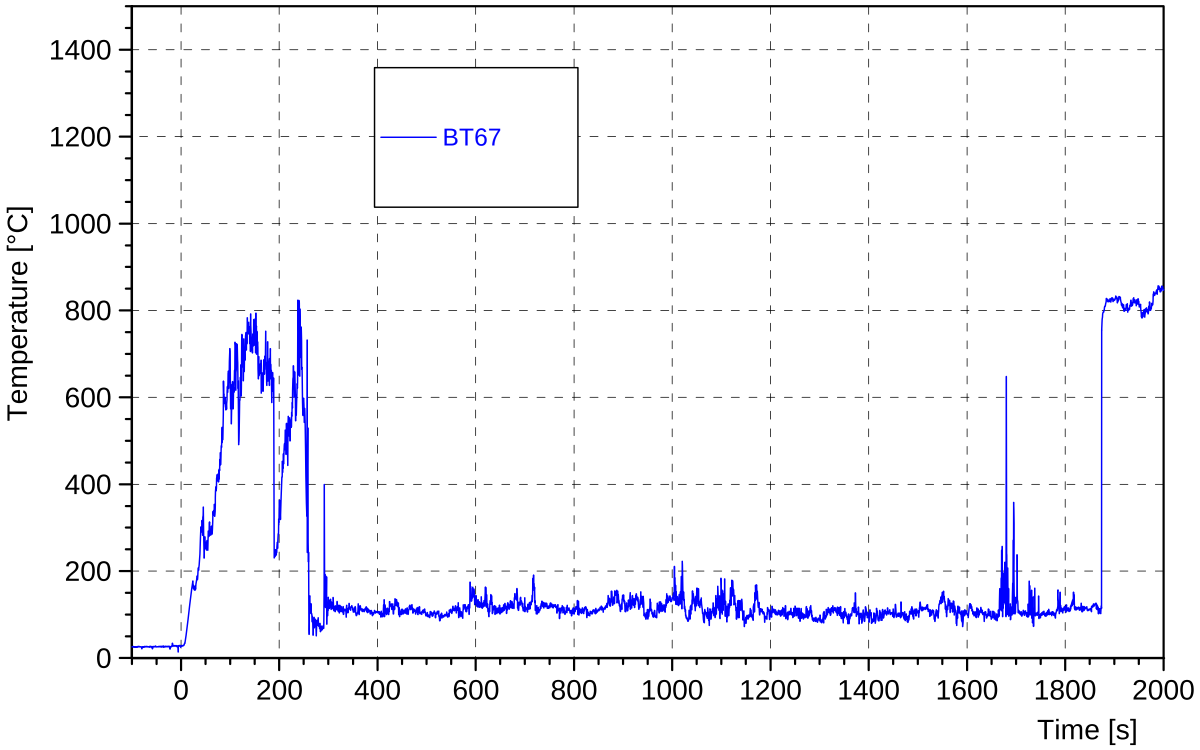

Figure C- 24: T8│NE- thermocouple in the side wall of the concrete crucible

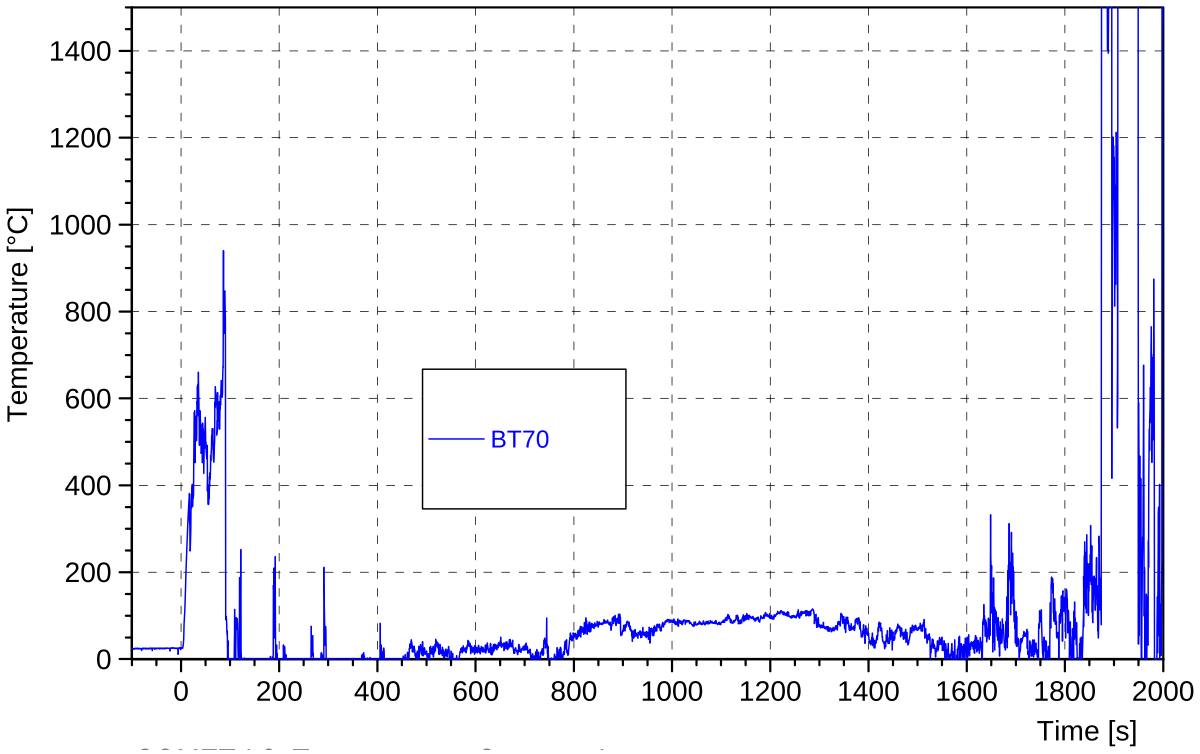

Figure C- 25: T8│SE- thermocouple in the side wall of the concrete crucible

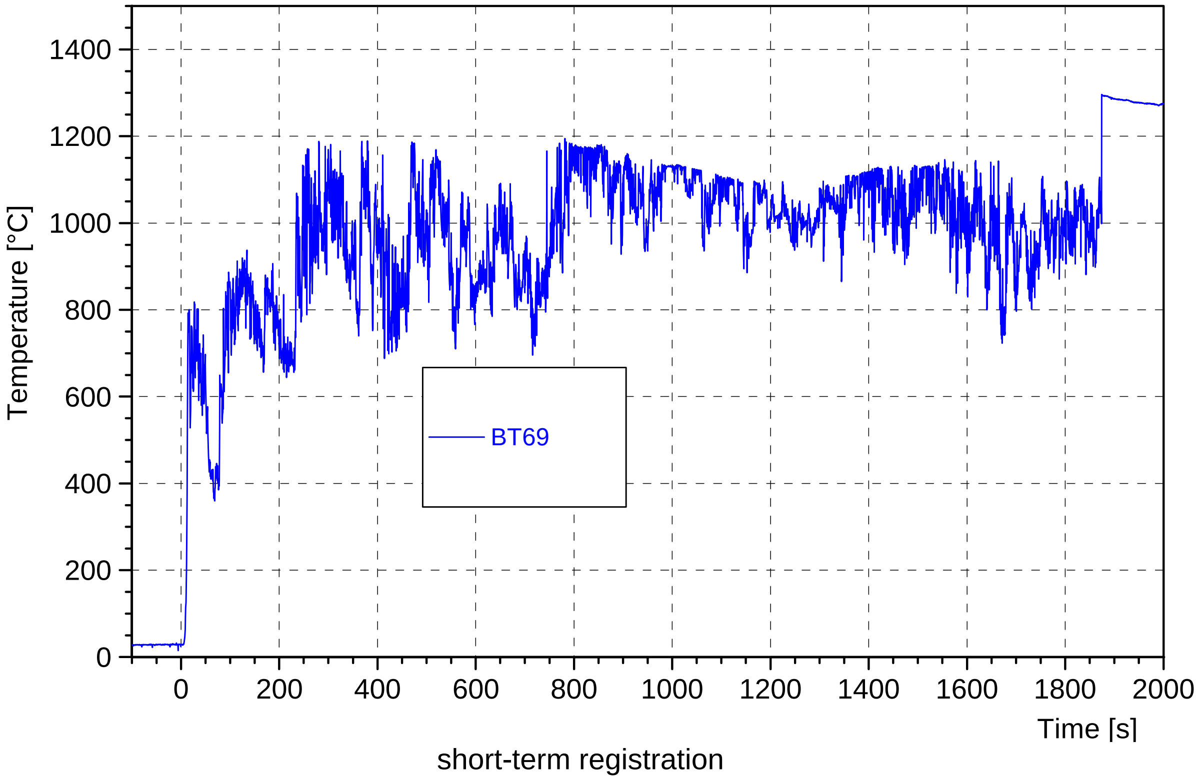

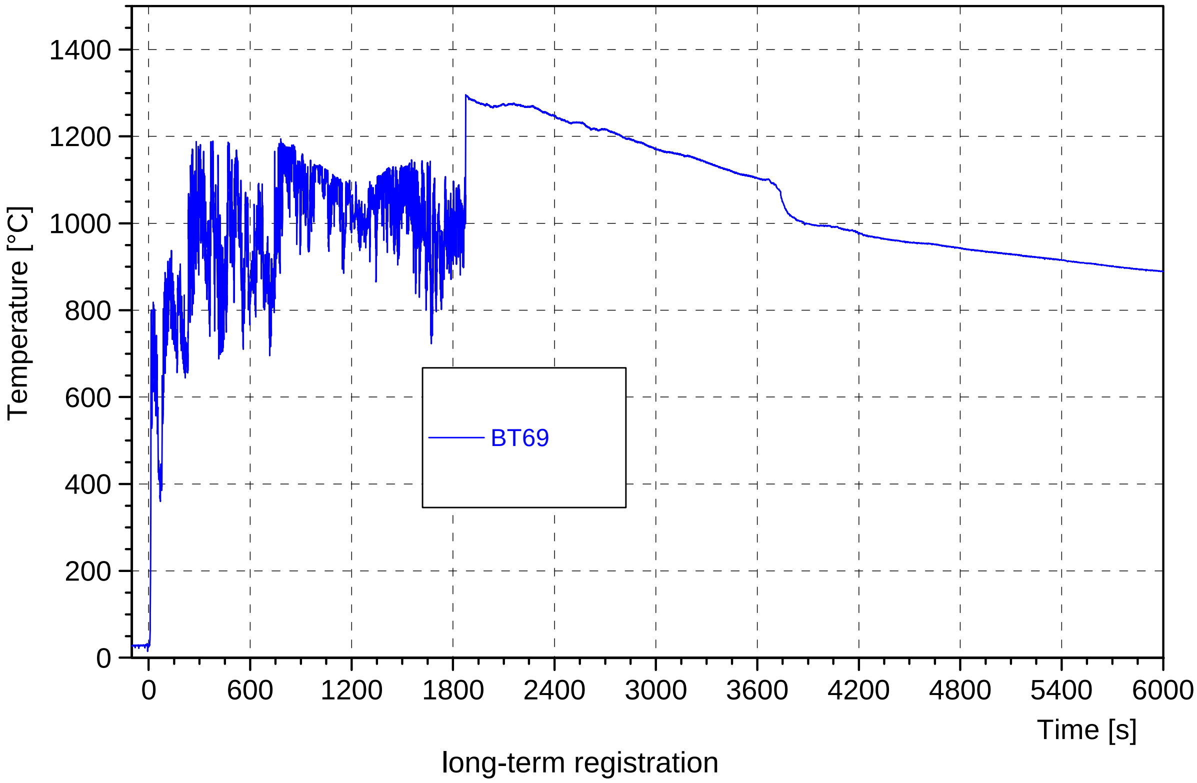

Figure C- 26: T8│SW- thermocouple in the side wall of the concrete crucible

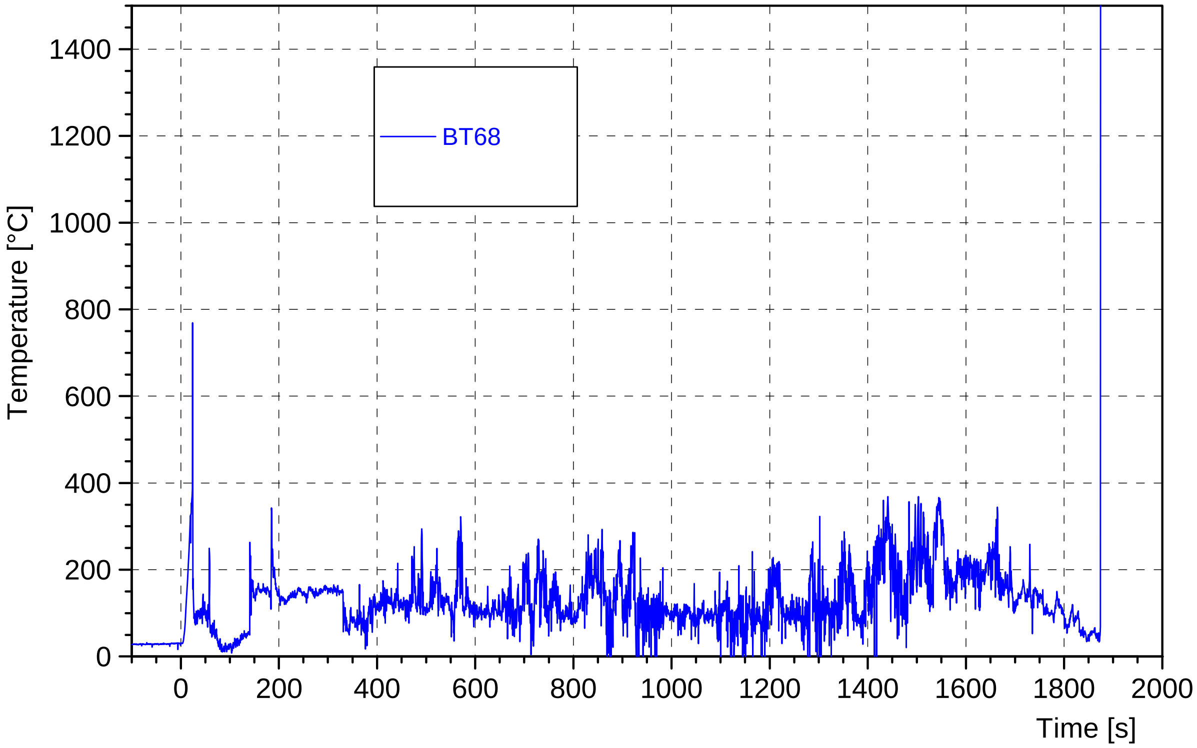

Figure C- 27: T8│NW- thermocouple in the side wall of the concrete crucible

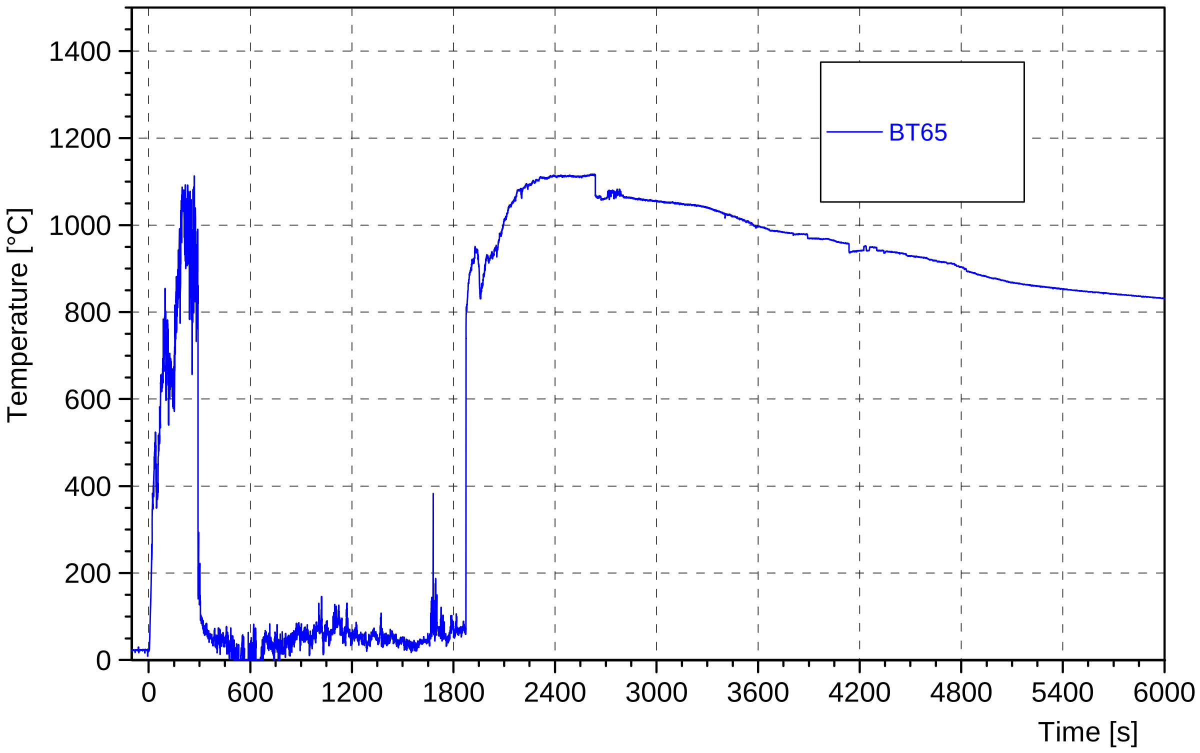

Figure C- 28: T9 | NE- thermocouple in the side wall of the concrete crucible

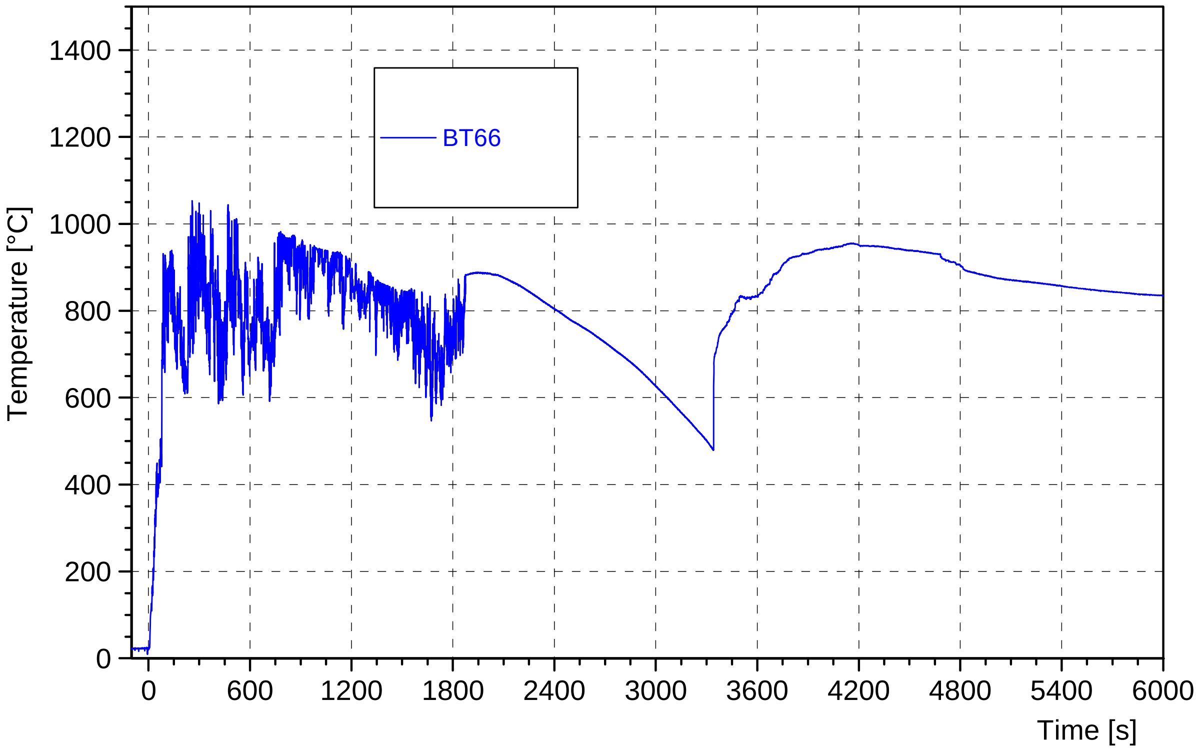

Figure C- 29: T9 | SW- thermocouple in the side wall of the concrete crucible

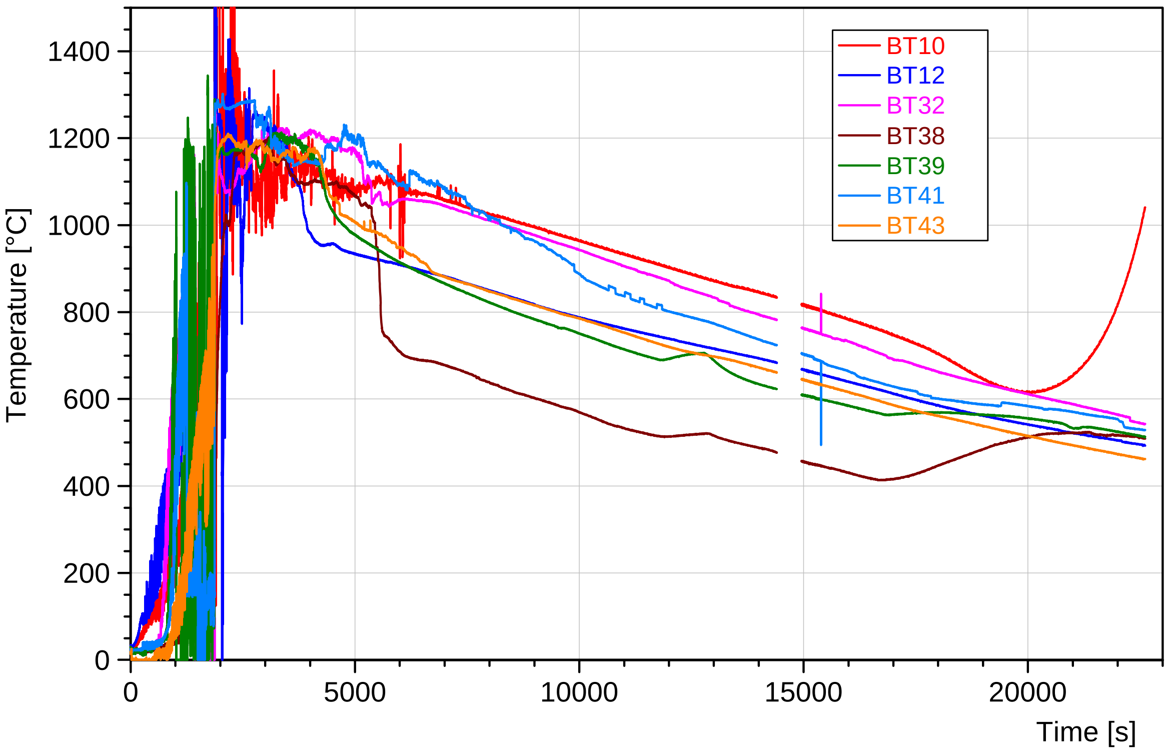

Figure C- 30: Long term temperatures at the erosion front in the lower cavity

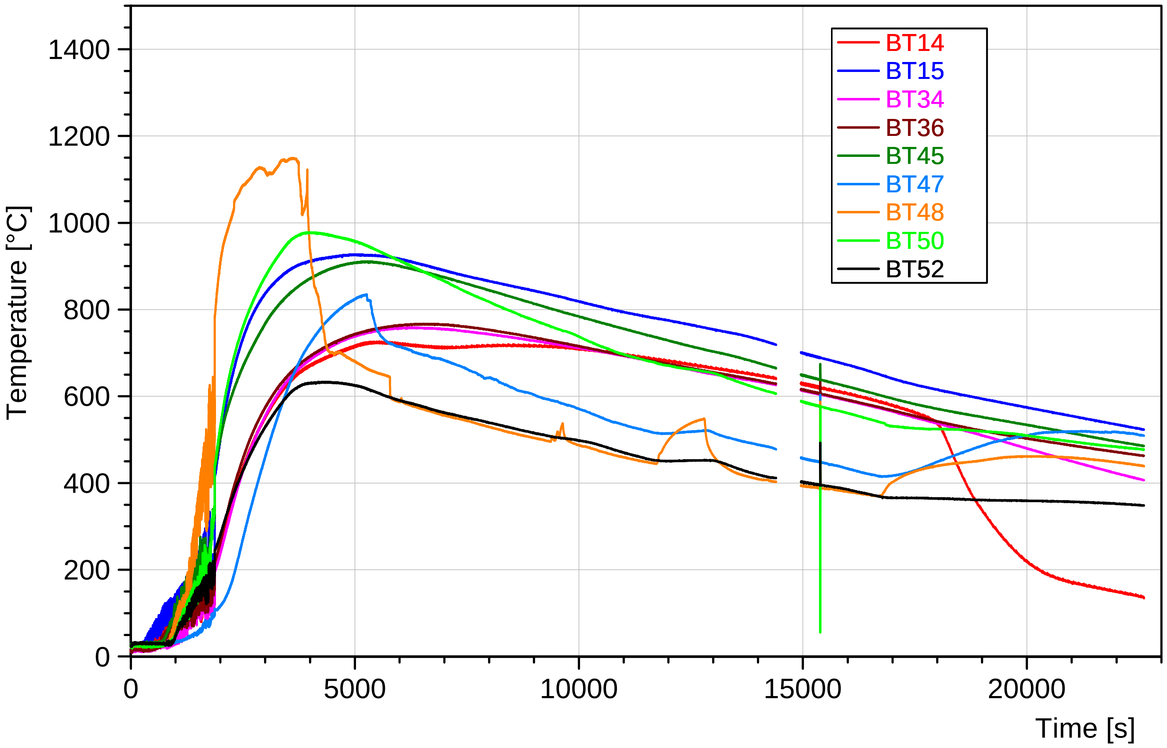

Figure C- 31: Long-term temperatures in the concrete layer close to the erosion front in the lower cavity

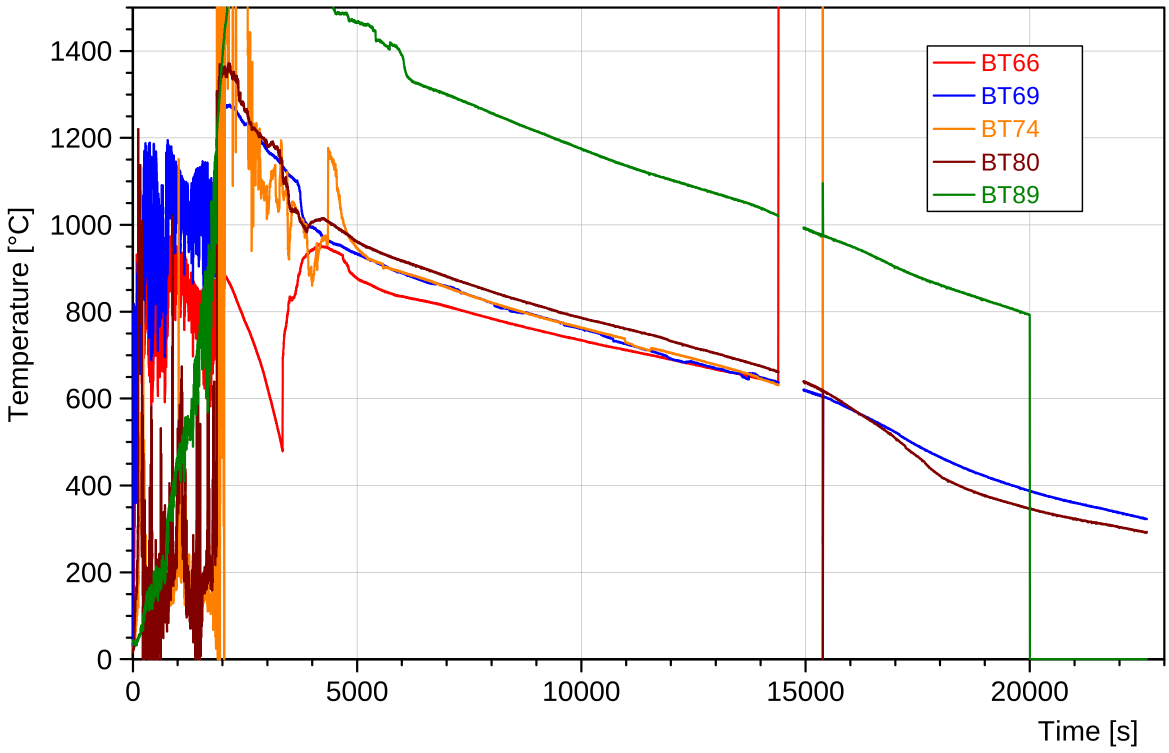

Figure C- 32: Long-term temperatures at the erosion front of the upper cavity, section SW. Thermocouple BT89 has significant offset after formation of a “new junction”.

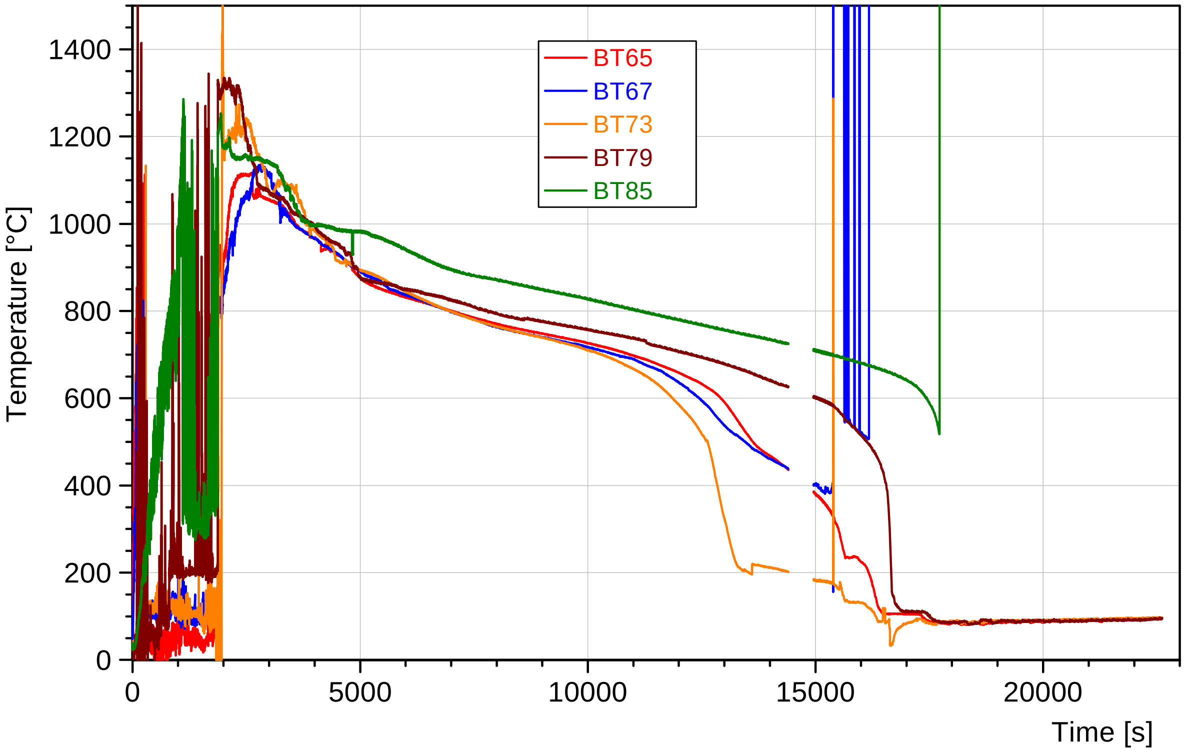

Figure C- 33: Long-term temperatures at the erosion front of the upper cavity, section NE. The thermocouples show quenching by the water between 13,000 and 18,000 s.

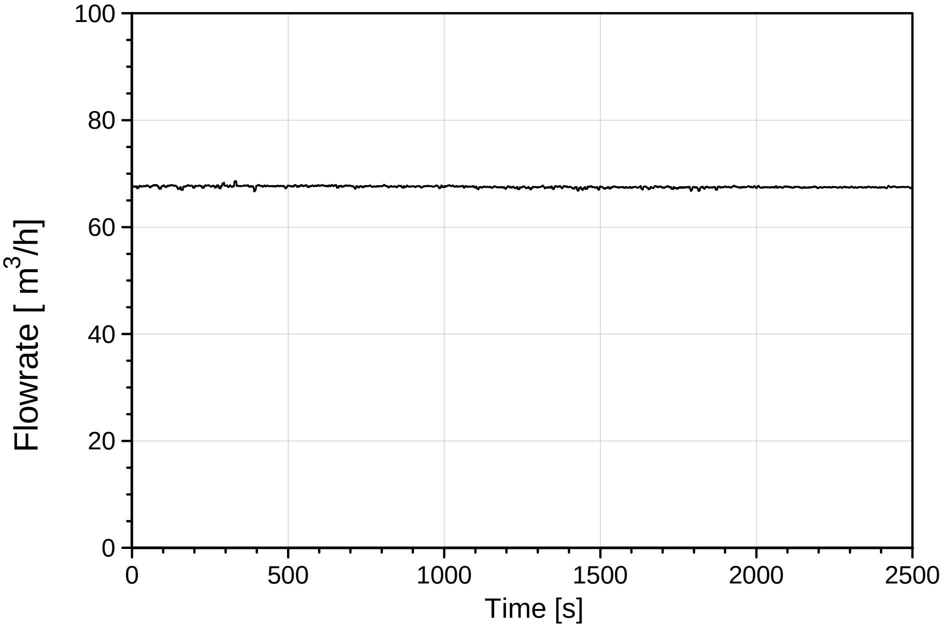

Figure C- 34: Argon cover gas flow into the crucible hood